UNIVERSIDADE FEDERAL DE SÃO CARLOS
CENTRO DE CIÊNCIAS EXATAS E DE TECNOLOGIA
DEPARTAMENTO DE QUÍMICA
PROGRAMA DE PÓS-GRADUAÇÃO EM QUÍMICA

Structural, Morphological and Optical Properties of $Ca_{10}V_6O_{25}$

Mayara Mondego Teixeira*

Thesis presented as part of the requirements to obtain the degree of DOCTOR IN SCIENCES, concentration area: CHEMISTRY.

Supervisor: Prof. Elson Longo

***scholarship: CAPES**

São Carlos – SP
2020

UNIVERSIDADE FEDERAL DE SÃO CARLOS

Centro de Ciências Exatas e de Tecnologia
Programa de Pós-Graduação em Química

Folha de Aprovação

Defesa de Tese de Doutorado da candidata Mayara Mondego Teixeira, realizada em 05/05/2020.

Comissão Julgadora:

Prof. Dr. Elson Longo da Silva (UFSCar)

Prof. Dr. Fenelon Martinho Lima Pontes (UNESP)

Profa. Dra. Caterina Gruenwaldt Cunha Marques Netto (UFSCar)

Prof. Dr. Manoel Gustavo Petrucelli Homem (UFSCar)

Prof. Dr. Miguel Ángel San-Miguel Barrera (UNICAMP)

O presente trabalho foi realizado com apoio da Coordenação de Aperfeiçoamento de Pessoal de Nível Superior - Brasil (CAPES) - Código de Financiamento 001.
O Relatório de Defesa assinado pelos membros da Comissão Julgadora encontra-se arquivado junto ao Programa de Pós-Graduação em Química.

Agradecimentos

Primeiramente agradeço a Deus pela vida.

Ao meu orientador Prof. Dr. Elson Longo que me proporcionou a oportunidade por todo ensinamento e aprendizado, no qual o considero como o meu pai científico.

Ao Prof. Dr. Juan Andrés por me aceitar na Universitat Jaume I (Castellon/Espanha) para a realização do doutorado sanduíche, e assim proporcionando a oportunidade de aperfeiçoamento e busca do conhecimento. Agradeço também, pela parceria com seu "Grupo de Química Teórica y Computacional" que realizou os cálculos teóricos dos trabalhos realizados nesta tese. À Profa. Dra. Rosa Llusar e à pesquisadora Dra. Eva Guillamón pelo auxílio na orientação e pela oportunidade de trabalharmos juntas.

Aos professores Dr. Maximo Siu Li, Dr. Luís Fernando da Silva, Dr. Adenilson Chiquito, Dra. Ieda Lucia Viana Rosa e Dra. Yara Galvão Gobato pelas contribuições e ensinamentos durante meu doutorado.

Ao Programa de Pós-Graduação em Química da Universidade Federal de São Carlos pela oportunidade. Em que este presente trabalho foi realizado com apoio da Coordenação de Aperfeiçoamento de Pessoal de Nível Superior – Brasil (CAPES) – Código de Financiamento 001.

Agradeço ao Conselho Nacional de Desenvolvimento Científico e Tecnológico (CNPq) pela oportunidade de realizar estágio no exterior (Doutorado Sanduíche no Exterior – SWE).

A todos que fazem parte do grupo CDMF e por toda estrutura fornecida para execução dessa pesquisa de doutorado. Aos técnicos Rori Camargo, Sandra e as secretárias Dani e Luma por todo auxílio durante esses anos. A todos os amigos que compartilharam comigo momentos especiais durante esse doutorado. Aos amigos Aline, Francisco, Pablo, Regiane, Thaisa e Camila por toda ajuda e parceria durante esses anos, que compartilharam comigo momentos especiais. Gostaria de agradecer também, a todos que fazem parte do grupo LIEC

que de forma direta ou indireta ajudaram no desenvolvimento e na realização deste trabalho.

Ao grupo dos maranhenses que compartilharam dos mesmos objetivos, Mitchell, Maya, Celis, Luciano, Beatriz, Sinara, Valéria e Thiessa, obrigada por todo apoio. Aos amigos Tayane, Clayane, Sérgio, Manoel e Lucas por todos os momentos vividos que jamais esquecerei.

Aos meus pais, Ilma Mondego e Jose Luiz, que sempre me apoiaram em tudo e ao meu irmão Rômulo que sempre me deu forças para correr em busca da realização dos meus objetivos. A todos os meus familiares, em especial a minha avó Malvina que me deu força em todos os sentidos e por meio de suas orações.

Table List

Figures List

Resumo

PROPRIEDADES ESTRUTURAIS, MORFOLÓGICAS E ÓPTICAS DO $Ca_{10}V_6O_{25}$. Modelar a estrutura e a morfologia dos cristais é de grande interesse no campo da ciência e da indústria, pois esses fatores estão fortemente ligados na determinação das propriedades dos materiais. Diante disso, foram sintetizados compostos de $Ca_{10}V_6O_{25}$ pelo método de coprecipitação e hidrotérmico assistido por micro-ondas em diferentes condições de tempo e temperatura no intuito de otimizar sua propriedade fotoluminescente. Estes métodos foram eficientes para a obtenção de diferentes morfologias, além disso, o efeito das condições de síntese teve forte influência na microestrutura e nas propriedades óticas dos compostos de vanádio. Diante disso, propôs-se um mecanismo de crescimento para as diferentes partículas formadas, como também observou-se que o método de síntese tem forte influência no grau de ordem/desordem estrutural. Por meio do controle da morfologia e dos tipos de defeitos na rede do cristal pode-se observar diferentes cores de emissão para os compostos $Ca_{10}V_6O_{25}$. Sendo que, a amostra que apresentou um equilíbrio no grau de ordem/desordem estrutural a curto-, médio- e longo-alcance, exibiu uma emissão na região do branco pelas coordenadas do diagrama de cromaticidade CIE. Então, propôs-se o mecanismo de fotoluminescência para os compostos sintetizados, assim como foi desvendado a sua estrutura e propriedades eletrônicos por meio da relação entre cálculo teórico e os dados experimentais. A propriedade fotoluminescente foi investigada em detalhes o qual foi observado que além das transições eletrônicas típicas do cluster de $[VO_4]$ tem-se a contribuição de níveis de energia que estão localizados no interior do *band gap*. Estes níveis de energia foram formados por diferentes tipos de desordem a curto, médio e longo alcance na estrutura.

Abstract

STRUCTURAL, MORPHOLOGICAL AND OPTICAL PROPERTIES OF $Ca_{10}V_6O_{25}$. Modeling the structure and morphology of crystals is of great interest in the field of science and industry, as these factors are strongly linked in determining the properties of materials. That said, $Ca_{10}V_6O_{25}$ compounds were synthesized by the coprecipitation and the microwave-assisted hydrothermal methods in a different time and temperature conditions in order to optimize their photoluminescent property. These methods were efficient to obtain different morphologies, in addition, the effect of the synthesis conditions had a strong influence on the microstructure and optical properties of vanadium compounds. Then a growth mechanism was proposed for the different particles formed, and it was observed that the synthesis method has a strong influence on the degree of structural order/disorder. By controlling the morphology and types of defects in the crystal lattice, different emission colors can be observed for the $Ca_{10}V_6O_{25}$ compounds. Since, the sample that presented a balance in the degree of order/disorder structural in the short-, medium-, long-range, exhibited an emission in the white region by the coordinates of the CIE chromaticity diagram. Then, the luminescence mechanism for the synthesized compounds was proposed, as well as its structure and electronic properties were revealed through the relationship between theoretical calculation and experimental data. The photoluminescent property was investigated in detail which was observed that in addition to the electronic transition typical of the $[VO_4]$ clusters, there is the contribution of energy levels that are located within the band gap. These energy levels were formed by different types of disorder at short-, medium-, and long-range in the structure.

Summary

1. Introduction

1. INTRODUCTION

Semiconductors have attracted a great deal of attention in both basic research and applications. In particular, semiconductors that act as photoluminescent materials have been regarded as a promising field of research in lighting technology [1, 2]. Since the emergence of the semiconductor laser in 1962 (also called diode lasers), rapid progress has been made, leading to developments such as optical fiber communications, laser disc recorders, optical storage, and laser printers [3]. Currently, there is an increasing demand to develop lasers with enhanced performance, the possibility of broadband tuning, and lower power consumption [3]. In this context, multicolor or multi-wavelength lasers covering broadband spectra are particularly useful for white-light-emitting diodes (w-LEDs) to be applied to color laser displays, optical sensing, biomedical imaging, photon computers, and on-chip optical communication [3-5].

The optical properties of a given material are a consequence of its interaction with light [6]. From a quantum perspective, the energy is produced when the incident wave is capable of inducing a pathway from the ground or fundamental electronic state to the excited states with higher energies. They will then relax to the fundamental state or states with lower energies accompanied by electromagnetic radiation in the ultraviolet (UV), visible, or infrared (IR) regions of the spectrum [6], with concomitant generation of photoluminescence (PL) emissions. The PL behavior of a given material can be controlled by varying the emission region, from the visible to the near-infrared region [7].

Research on the crystal surface engineering of semiconductors has demonstrated that the surface structures play an important role in their activities, because photoelectron conversion takes place when photoinduced electrons and holes are available on the surface [8]. Both the development of optical technology and the photoelectric properties of semiconductors can be further enhanced or optimized by tailoring the morphology and the exposed surfaces of the crystals [9].

Vanadate compounds formed by combining the VO_4^{3-} group and divalent cations, M^{2+}, belonging to the family of the alkaline earth metals, M^{2+} = Mg^{2+}, Ca^{2+}, Sr^{2+}, and Ba^{2+}, in the crystalline structure show an intrinsic broadband emission with good thermal, optical, and chemical stability, better chromaticity, and high luminous efficiency [10, 11]. Novel oxide-based materials including calcium vanadates are promising candidates with enhanced PL emissions. In particular, the Ca^{2+} cation can form complex structures such as CaV_2O_6, $Ca_2V_2O_7$, $Ca_3V_2O_8$ $Ca_4V_4O_{14}$, $Ca_{10}(VO_4)_6(OH)_2$, and $Ca_{10}V_6O_{25}$ [12-14]. Their characteristic PL emissions are associated to the VO_4^{3-} group [10, 15-17]. However, despite the unquestionable relevance of $Ca_{10}V_6O_{25}$ as a material, a comprehensive and reliable picture of its structure, surface, and electronic properties as well the mechanism underlying PL emissions is far from being achieved [13, 16]. For this system, current research activities focused on enhancing its optical performance via morphological control, crystal facet engineering, and reducing the band gap are the main objective of this PhD dissertation.

On the basis of the above considerations, in this study we present a unified experimental and theoretical study aimed at enabling us to garner a comprehensive understanding of solid-state chemistry in terms of the synthesis and properties of $Ca_{10}V_6O_{25}$. To do so, the energetic, structural, electronic, and morphological properties of $Ca_{10}V_6O_{25}$ were analyzed by experimental techniques, with the major aspects being substantiated and further elucidated by state-of-the-art density functional theory (DFT) calculations. Our main insights are associated with the critical role of the single chemical environments found in the bulk as well as on the surfaces of the $Ca_{10}V_6O_{25}$ material. These results are of great importance for our understanding of the relationship between morphology and activities, and can enable us to synthesize high-efficiency $Ca_{10}V_6O_{25}$-based materials with desirable properties. The proposed synthesis routes and spatial reconstruction performed had the potential to simulate processing conditions to produce various microcrystals and explore material surface structures,

morphology, crystal defects, and reconstruction of microstructures. As a general lesson on the synthesis of $Ca_{10}V_6O_{25}$, we have learned that the choice of the synthesis method and temperature are crucial to allow a more rational approach to morphology control.

1.1. Structure and Morphology

The idea that structure and morphology determine functionality is one of the leitmotifs driving research and applications in fields such as catalysis, plasmonics or optical devices. From the structural point of view, the characteristic that is commonly recognized for the vanadate compounds is the presence of $[VO_4]$ clusters in the crystalline structure [18], which act as building blocks in the lattice and provide a structural diversity that is responsible for the appearance of different properties with promising technological applications [14]. The structure of $Ca_{10}V_6O_{25}$ has aroused interest among researchers as morphological changes can be carried out by controlling the synthesis conditions [16], which in turn has a strong influence on the properties of the as-synthesized materials [9, 19, 20].

Under equilibrium conditions, the morphology of a crystal is determined by intrinsic factors [21]. The crystal morphology with different exposed surfaces is important for improving the properties and applications of materials [9, 20, 22]. These surfaces correspond to the most energy-stable atomic planes in the lattice with the minimum stacking energy [21]. However, in practice, most crystals grow in non-equilibrium conditions and the morphology is strongly influenced by factors such as changes in supersaturation and ionic strength [21]. In general, different facets of crystals have specific physical and chemical properties [19]. Thus, a small variation in the synthesis conditions can drastically affect the electrical, electrochemical, optical, magnetic, adsorption, and catalytic properties of semiconductors [23-26]. The modulation of functional materials in order to provide

high efficiency in their application has therefore been a subject of considerable interest for different chemical industries [9, 27, 28].

Control over the morphology of a given material, from the nanoscopic to the macroscopic scales, contributes to their improvement and induces the emergence of new properties [21, 29]. An understanding of crystal morphology evolution is significant for the design, synthesis, and applications of crystals with surface-enhanced properties such as catalysis, optical devices, and other applications [30-34]. The morphology does not only control the material's physicochemical properties, but also determines its relevance and merit with regard to technological applications [35-38]. However, there are still many questions to be answered about how the surface of a particle behaves under reactive environments, and it is a challenging task in the development of functional materials, since controlling the conditions throughout the synthesis process allows the bonding characteristics to be modified in order to render a given structure with a specific morphology and exposed crystallographic surfaces (FIGURE 1.1) [9, 20, 39]. Thus, each surface corresponds to an exposed plane of the crystals and a wide range of morphologies can be obtained, including spheres, wires, rods, and plates. Hence, a correlation among the structure, morphology, and electronic and optical properties of a given semiconductor becomes apparent [27].

FIGURE 1.1 - Different morphologies obtained by changes in the experimental conditions.

1.1.2 Synthesis methods

Many synthesis strategies have been developed in the past two decades to selectively form materials with distinct surface structures in order to control the morphology of the as-synthesized materials. It is well known that the physicochemical performance of micro/nanoscale materials is strongly affected by the crystal size, shape, and defect structure [40-42]. Solution-based synthesis has been one of the most common routes. Studies have been carried out to achieve control over particle size, shape, and phase by changing various synthesis parameters (i.e., chemical precursors, concentration, temperature, pH, additives, and stirring rate). Among them, the microwave-assisted hydrothermal method is capable of inducing morphological changes by controlling the growth kinetics of different particle sizes and morphology [43-45]. Furthermore, it favors good homogeneity in the size and shape of the particles, as well as in the purity of the phases of the crystals [28]. The microwave-assisted hydrothermal route has been considered a clean, versatile, fast, and highly efficient method to obtain both organic and inorganic compounds [46-49].

The coprecipitation method is also an adequate synthetic procedure as it shows a good dispersion of particles with uniform size and high purity [50], in addition to being considered a simple, fast, and inexpensive method due to the low temperatures involved [51]. The experimental conditions change the bulk and the surface of the crystal, and can also influence the surface defects, the free concentration of the charge carriers (electron/hole), the morphology, and the grain size [52]. Thus, the structural order/disorder of the bulk and surface are factors that can also strongly influence the properties of the crystals [52]. The order/disorder effect in the microstructure determines the surface charge, and the concentration of oxygen vacancies, which will influence the value of the band gap in the surface or the bulk and this changes the property of the material [52].

The way to extend the functionality of semiconductors in electronic devices is through structural and morphological modifications [19], as different crystal morphologies have different energies and provide different excited states corresponding to each exposed face, which has a great influence on the applications [21]. Each type of facet contains a specific arrangement of surface atoms, which means that the surface atoms in different facets have different activities [53, 54]. Morphology-controlled materials serve as a model to bridge the gap between optical performance and material science because variation in the morphology always results in different crystal surfaces whose definite atomic arrangement is crucial to study the relationship between structure and properties [55-57].

1.2. Photoluminescence Emissions

The development of new compounds with highly efficient and tunable optical properties has become increasingly challenging for industry. In particular, scientists and engineers have focused especially on investigating and optimizing inorganic solids that consist of luminescent centers. Various optical devices, such as fluorescent lamps, light-emitting diodes, luminescent pigments, and sensors, which are based on these systems, have been obtained [58, 59].

Vanadate compounds have complex and chemically stable structures that are promising candidates for phosphor application [12, 18]. They contain the VO_4 cluster as structural moiety in the crystal lattice and display self-activated PL emissions. In the VO_4 cluster, the central V^{5+} metal is coordinated by four oxygen anions in a tetrahedral arrangement in which the symmetrical configuration corresponds to the T_d point group. This moiety is known to be an efficient luminescent center [60] due to the real coordination polyhedron could be thought of as having certain deformations from a perfect model. In this sense, microstructural

modifications in the VO_4 tetrahedra of the crystalline lattice change the morphology of the as-synthesized materials and modify the PL emissions [61].

The intrinsic optical emission of vanadium compounds, predominantly in the visible region, results from the charge transfer from the 3*d* orbital of the vanadium to the 2*p* orbital of the oxygen in the tetrahedron [VO_4] cluster [61]. These transitions are favored due to structural distortions, as the transition in the symmetrically ordered [VO_4] cluster is spin-forbidden. However, distortions in both the V–O bond and O–V–O bond angles in the [VO_4] clusters cause the transition to be partially allowed [62]. In this way, PL emissions can be modulated by means of structural distortions in the [VO_4] clusters, by the method of synthesis [18].

FIGURE 1.2 shows a schematic representation of the PL mechanism in the [VO_4] clusters, in which first the electrons are excited from the ground state $^1A_1$ to the excited levels of highest energy $^1T_1$ and $^1T_2$. The electrons then undergo decay to the metastable states $^3T_1$ and $^3T_2$ and subsequently return to the ground state through a radiative process with the emission of photons [63]. The excitation transition is spin-allowed, while emission is spin-forbidden. However, it becomes partially allowed due to the loss of symmetry of the VO_4 tetrahedra, and with this there is a relatively long decay time in the order of milliseconds for the vanadate phosphors [18, 64].

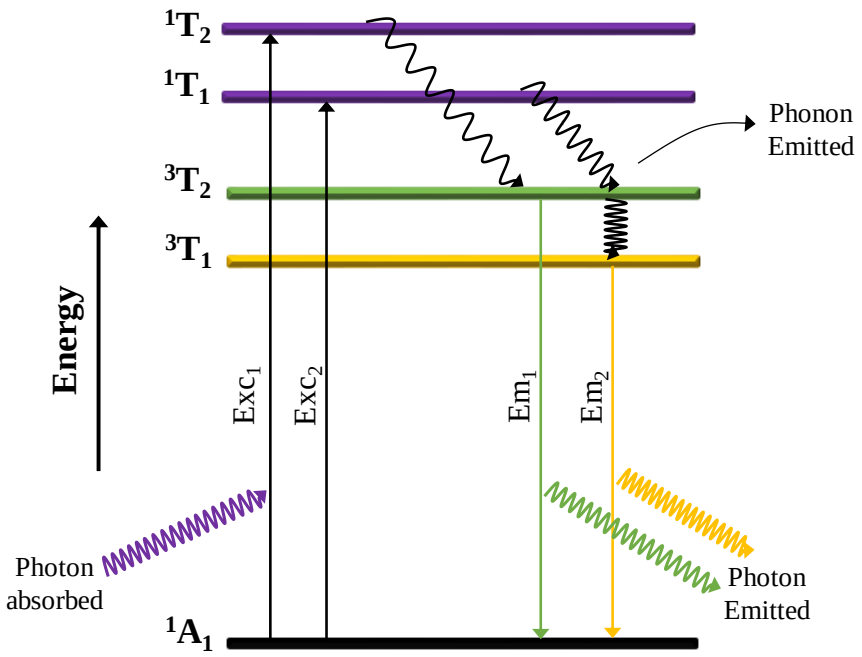

FIGURE 1.2 - Photoluminescence mechanism in the [VO_4] cluster.

It is well known that the electronic transition in the tetrahedral [VO_4] cluster is strongly dependent on the structural characteristics and the network modifying cation [18, 61, 65]. Therefore, different colors in the visible region are observed for vanadium compounds, which can be found in the blue region for YVO_4 [66], green for $Ba_2V_2O_7$ [10], yellow for $Mg_3(VO_4)_2$ [18], red for $KVOF_4$ [67], and in the white region for $CsVO_3$ [4]. However, even today, the origin of the different emission colors of vanadate compounds remains uncertain. Therefore, many studies have been carried out in order to unravel the PL mechanism and color variation, since the vanadate compounds with the VO_4 luminescent centers have shown themselves to be promising candidates for phosphor applications [18].

1.3. Broadband PL mechanism

The broadband model (FIGURE 1.3) shows that PL emission stems from the contribution of different levels of energy present within the band gap of the material [52]. These energy levels are formed due to structural order/disorder in

the short, medium, and long range [68-70]. This is because the real lattice is not perfect and contains a distribution of defects such as lattice vacancies that create a heterogeneous distribution of excited states [71]. These defects can have an enormous effect on the PL behavior, since they participate in the emission mechanism.

The structural order/disorder generates localized states that are acceptors/donors of electrons and holes [72, 73]. Thus, at room temperature electrons can be found in both the fundamental and the excited states, occupying these energy levels formed by structural defects [70, 74]. Moreover, the localized levels are distributed energetically within the band gap, and thus allow the excitation of electrons with various energies, so that the radioactive decay leads to a broadband emission [72, 74]. Localized states are characterized as shallow defects when they are near the valence band (VB) and the conduction band (CB), or as deep defects when they are located in a more internal region of the band gap (FIGURE 1.3(1)) [69, 74].

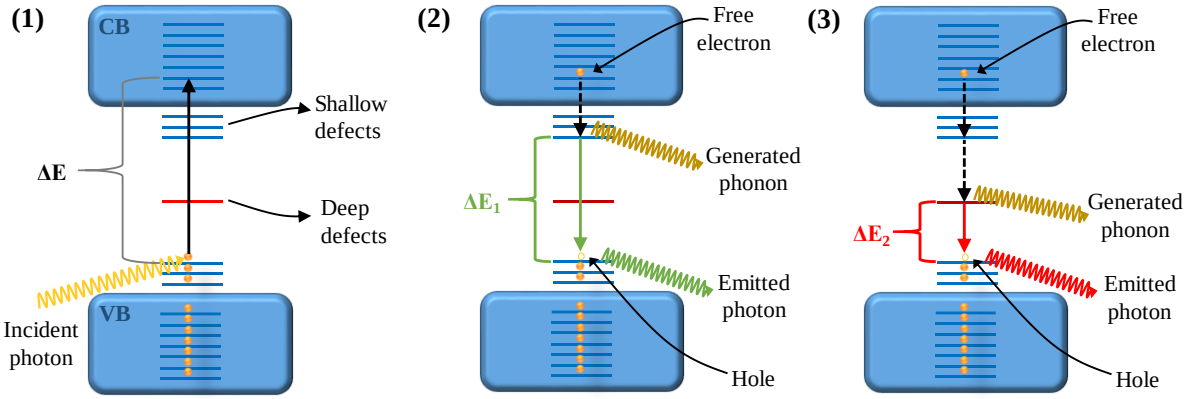

FIGURE 1.3 - Broadband photoluminescence mechanism.

Throughout the PL emission process, first the absorption of the incident photon occurs, which causes the transition of an electron from the lowest to a higher energy level, see FIGURE 1.3(1). In that moment, a hole is formed at the point where the electron was located, and this electron is situated in the CB [75]. The subsequent process occurs in such a way that the excited electron undergoes

a relaxation to lower energy levels [74] (see dashed arrow in FIGURE 1.3(2)) through a non-radioactive transition in which the energy is released by the phonons that generate vibrations and heat in the crystal lattice [75]. Then there is the radioactive transition, in which the electron returns to the lowest energy level through the emission of photons, where each emitted photon corresponds to a wavelength and specific energy in the visible region [74] (see green and red arrows in FIGURE 1.3(2) and (3)). The contribution of these different photons favors broadband emission, which is also called the multi-photon process [69].

2. Goals

2. GOALS

To obtain $Ca_{10}V_6O_{25}$ compound and evaluate photoluminescent behavior.

2.1. Specific goals

- ✓ To obtain $Ca_{10}V_6O_{25}$ compounds by the coprecipitation (CP) and microwave-assisted hydrothermal (MAH) methods;
- ✓ To evaluate the structural order/disorder effect of short-, medium-, and long-range on optical properties;
- ✓ To investigate the morphology influence on the PL property;
- ✓ To study the photoluminescence mechanism of $Ca_{10}V_6O_{25}$.

3. Towards a white-emitting phosphor $Ca_{10}V_6O_{25}$ based material

3. TOWARDS A WHITE-EMITTING PHOSPHOR $Ca_{10}V_6O_{25}$ BASER MATERIAL

Mayara Mondego Teixeira[1], Yara Galvão Gobato[2,3], Lourdes Gracia[4$], Luís Fernando da Silva[2], Waldir Avansi Jr[2], Marcelo Assis[1], Regiane Cristina de Oliveira[5], Gabriela Augusta Prando[2], Juan Andrés[4] and Elson Longo[1*]

[1]CDMF-UFSCar, Universidade Federal de São Carlos, P.O. Box 676, 13565-905 São Carlos, SP, Brazil.

[2]Departamento de Física, Universidade Federal de São Carlos, Rod. Washington Luiz, km 235, CP 676, CEP 13565-905, São Carlos, SP, Brazil.

[3]High Fields Magnetic Laboratory, Radboud University, Toernooiveld 7, 6525 ED, Nijmegen, Netherlands.

[4]Departamento de Química Física i Analítica, Universitat Jaume I, 12071, Castelló de la Plana, Spain.

[5]Grupo de Modelagem e Simulações Moleculares, Faculdade de Ciências, Universidade Estadual de São Paulo, Bauru, SP, Brazil.

[$]Permanent address: Departamento de Química Física, Universitat de València, 46100, Burjassot, Spain

3.1. Abstract

To achieve a stable material capable of white-light emission, we fabricated $Ca_{10}V_6O_{25}$ by both co-precipitation (CP) and microwave-assisted hydrothermal (MAH) methods at different temperatures. The effects of structural disorder at a short-range (Raman spectra), medium-range (UV-vis spectra), and long-range (X-ray diffraction) on the material structure and its effect on optical properties were investigated. Both CP and the MAH methods were efficient for obtaining pure $Ca_{10}V_6O_{25}$ material with different morphologies. Significant changes in morphology and degree of structural order and disorder were found to affect the photoluminescence (PL) properties. All samples exhibited a broadband PL spectrum, characteristic associated to charge transfer processes of the $[VO_4]^{3-}$ group, as well as transitions that occurred in the energy levels located within the band gap. The samples obtained by the MAH method at temperatures of 100 °C and 120 °C exhibited a lower structural disorder (at long- and short-ranges), the CIE chromaticity coordinates were located in the white region, MAH100 (x = 0.311 and y = 0.348) and MAH120 (x = 0.350 and y = 0.368). Furthermore, we conducted a detailed study of temperature dependence of PL spectra. All samples displayed decreased luminescence intensity as temperatures increased and low values of activation energy (approximately 2 meV). Finally, the as-synthetized $Ca_{10}V_6O_{25}$ material has interesting properties for possible applications as a white-emitting phosphor under ultraviolet excitation.

3.2. Introduction

The intrinsic characteristics of vanadium-based oxides increase their potential utility for applications such as lighting, gas sensing, electrochemical, and photocatalysis [15, 76, 77], as well as for phosphorus applications, because they exhibit at long-wavelength excitation and chemical stability [61, 78]. Thus, many

vanadates have been studied for their broadband emission properties, making them a promising material for white-light-emitting diodes (WLEDs) [65, 79, 80]; furthermore, they display superior properties, such as high bright-light emission and long service lifetimes. In particular, vanadate groups ($[VO_4]^{3-}$) present in the lattices of vanadium-based oxides display a wide emission range in the visible spectral region, because of owing to their self-activated emitting properties [81] that correspond to two typical charge transitions. The luminescence is usually generated by the charge transfer transition from the 2*p* orbital of oxygen to the 3*d* orbital of vanadium. Additionally, the emission wavelength depends on the presence of metallic cations between $[VO_4]^{3-}$ groups [65, 82]. The high photoluminescence (PL) emission efficiency has been examined and justified in terms of structural distortions in the V–O bond and the O–V–O bending motions of the $[VO_4]$ tetrahedron, as building blocks forming the structure of the material; these distortions yield a symmetry-breaking process within the $[VO_4]$ tetrahedron clusters. Consequently, the distortions increase the likelihood of spin-forbidden transitions compared that in isolated and ordered $[VO_4]$ clusters [61, 65]. These structural distortions of the $[VO_4]$ tetrahedra may cause energy level shifts in both ground and excited states, leading to the material emitting different luminescent colors [65]. Huang *et al.* observed that larger distortions of the $[VO_4]^{-3}$ groups increases the probability of charge transfer processes occurring [61]. This structural change causes the parity-forbidden d-d transition of vanadium to become partially parity-allowed; additionally, the spin-forbidden $^3T_2$ ($^3T_1$) – $^1A_1$ state transition become partially allowed due to the mixing of $^3T_2$ ($^3T_1$) states with high-energy excited singlet states.

Different synthetic methods were used to obtain the $Ca_{10}V_6O_{25}$ superstructure examined herein. Previous research detailed a hydrothermal method for synthesizing calcium vanadate under temperature conditions of 120–180 °C for 24 hours at pH = 12.5 [13, 16, 83]. By using this method, researchers noted modifications in the crystalline structure due to the increase of the

temperature and hydrothermal reaction time. These modifications led to more intense diffraction peaks and consequently to greater crystallinity. Li *et al.* used a precipitation method to obtain $Ca_{10}V_6O_{25}$; they determined a series of ideal conditions for the reaction, including a reaction temperature of 90 °C for a 2 h period, which resulted in an interesting column-like crystal morphology [84]. Although there are several procedures for obtaining $Ca_{10}V_6O_{25}$, the microwave-assisted hydrothermal (MAH) method is considered to be promising owing to the more manageable synthetic conditions and excellent particle size control [85]. Absorption of microwave energy causes heating of particles, which accelerates both diffusion and collision [85]. For example, in reference [86] $Ca_{10}V_6O_{25}$ was synthesized at a temperature of 120 °C at different times (4, 8, 16, and 32 min), observing different morphologies for the resulting material. Thus, this methodology is desirable for the preparation of $Ca_{10}V_6O_{25}$ under low-temperature conditions that provides morphology control.

Recently, we obtained $Ca_{10}V_6O_{25}$ structures through a combination of the co-precipitation (CP) and microwave-assisted hydrothermal (MAH) methods [86]. As a continuation of previous works, we investigated the luminescence properties of vanadium materials by manipulating the synthesis temperature, thus influencing the morphological, structural order/disorder at long-, medium-, and short-range on the optical properties of $Ca_{10}V_6O_{25}$. Specifically, we investigated the PL and thermal quenching properties. The materials were characterized through X-ray diffraction (XRD), Raman spectroscopy, diffuse reflectance spectroscopy in the ultraviolet/visible region (UV-vis), field emission scanning electron microscopy (FE-SEM), energy dispersive X-ray spectroscopy (EDX), and X-ray absorption near edge structure (XANES).

In this paper, we have discussed the long-range structural order/disorder effects associated with XRD and Rietveld refinement with first principle calculations. These effects are related to the spatial periodicity of the atomic arrangement for large distances in the crystal lattice. The degree of local

order/disorder in the medium-range are studied by UV-vis diffuse reflectance and PL spectroscopy; these effects extend between the calcium and vanadium clusters present in the material structure. Finally, we study the structural short-range order/disorder effects by Raman and XANES spectroscopies; these short-range effects extend only to the nearest neighbors, being characterized as punctual defects in the crystal lattice.

3.3. Experimental methods

3.3.1 Synthesis

The $Ca_{10}V_6O_{25}$ compounds were synthesized via the CP and MAH methods according to a procedure we previously reported [86]. First, 2 mmol of NH_4VO_3 (≥ 99.9%, Sigma-Aldrich) was dissolved in 30 mL of distilled water and heated to 50 °C under constant magnetic stirring until complete dissolution. Separately, 1.6 mmol of $CaCl_2.2H_2O$ (99.0%, Synth) was dissolved in 30 mL of distilled water. For the CP method, the calcium and vanadium solutions were mixed, and the pH was adjusted to 12.5 via the addition of the aqueous 6 mol/L KOH solution, and the final volume was adjusted to 70 mL then heated to 100 °C. The solution remained in equilibrium at 96 °C for 1 h (sample named CP96). For the MAH method, after adjusting the pH and obtaining a final volume of 70 mL, the precipitate formed was processed for 1 h at various temperatures of 100, 120, and 160 °C, the samples were denoted as MAH100, MAH120, and MAH160, respectively. All powders were collected at room temperature, centrifuged, and washed with distilled water resulting in a pH of around 7, then subsequently dried at 60 °C for 12 hours.

3.3.2. Characterizations

$Ca_{10}V_6O_{25}$ samples were characterized by XRD using a Rigaku-DMax/2500PC (Japan) diffractometer, with Cu Kα radiation (λ = 1.5406 Å) in the 2θ range of 5° to 75° with a scanning rate of 0.02°/min with 40 kV and 150 mA. The Rietveld refinements were performed in the General Structure Analysis System (GSAS) program, the scan speed of 6º/min for a 2θ range of 10º to 110º with 40 kV and 60 mA. The Raman spectra measurements were carried out using a Horiba Jobin-Yvon T64000 spectrometer (Japan) coupled to a CCD Synapse detector and an argon-ion laser emitting at 514 nm with a laser power of 7 mW. The spectra were measured in the 40 - 1200 cm^{-1} range. The XANES spectra were collected at the V K-edge using the D08B-XAFS2 beamline at the Brazilian Synchrotron Light Laboratory (LNLS). XANES spectra were collected in transmission mode at room temperature using a flat Si (111) double crystal monochromator, measured from 45 eV below and 75 eV above the edge, with an energy step of 0.3 eV near the edge region. To provide a good reproducibility during the collection of XANES data, the energy calibration of the monochromator was checked while the data were being collected, using a V metal foil. In addition, the data were normalized to the edge and aligned in energy, using the MAX software [87]. The FE-SEM measurements were taken using a Supra 35-VP Carl Zeiss (Germany) operated at 15 kV. The EDX mapping was recorded in the field emission scanning electron microscopy (FE-SEM) of the FEI Company, model Inspect F50. UV-vis spectra were obtained using a Varian spectrophotometer model Cary 5G (USA) in diffuse reflection mode. PL measurements at room temperature were carried out using a Monospec 27 monochromator Thermal Jarrel Ash (USA) coupled with a R955 photomultiplier Hamamatsu Photonics (Japan). A krypton ion laser Coherent Innova 200 K (line 350 nm) with laser power about 14 mW on the samples. PL measurements as a function of the temperature (30 K to 300 K) were performed using a 500M Spex

spectrometer coupled with a GaAs PMT. A Kimmon He-Cd laser (line 325 nm) with laser power up to 40 mW was used as the excitation source for PL measurements.

3.3.3. Computational Method

First principle calculations including the temperature are performed using a standard statistical-thermodynamics approach, within the limit of the quasi-harmonic approximation implemented in the CRYSTAL17 package [88], where zero point and thermal pressures are evaluated and added to the static pressure at each cell volume, to obtain the total pressure as a function of both temperature and volume. The calculated equilibrium lattice parameters optimized at the B3LYP level [89, 90] were previously published [86].

3.4. Results and discussion

3.4.1. Long-range structural order: XRD and Rietveld Refinement

The XRD patterns showed the degree of long-range structural order/disorder for the $Ca_{10}V_6O_{25}$ obtained by the CP method at 96 °C and by the MAH method at 100, 120, and 160 °C, see FIGURE 3.1. The $Ca_{10}V_6O_{25}$ phase corresponds to a hexagonal structure conforming to the $P6_3/m$ space group, indexed according to the JCPDS file No. 52-649 (FIGURE 3.1a). To observe the degree of order/disorder at the long-range scale, a full width at half maximum (FWHM) measurement was performed for the (211) and (300) planes (FIGURE 3.1b), since the diffraction peaks result from the lattice parameters—namely, atom arrangement and periodicity over long distances. For a perfectly ordered crystal structure at long-range, the observed peaks are sharp and intense [91, 92]. The sample obtained using the CP method (CP96) exhibited less-defined peaks in the 29–34°

range, with a FWHM value of 0.41° (211) and 0.69° (300). Thus, this material presented with structural distortions along the Ca–O and V–O bonds lengths, as well as the O–Ca–O and O–V–O bond angles, generating distorted $[CaO_6]_d$ and $[VO_4]_d$ clusters. For the MAH100 and MAH120 samples, FWHM values of 0.24° (211), 0.22° (300) and 0.24° (211), 0.24° (300) were observed, respectively; the MAH160 sample obtained at 160 °C exhibited an increase in the FWHM values at 0.36° (211) and 0.52° (300). The materials that were subjected to microwave radiation favored the crystallization and displayed long-range structural ordering. Thus, the samples obtained by the MAH method exhibited more defined peaks than those obtained by the CP method. In this way, the higher FWHM value observed for the CP96 sample is indicative of higher structural disorder at long-range; thus, it was likely to result in higher energy (eV) of the PL emission properties. However, in the MAH system, a temperature increase to 160 °C resulted in dissolution and recrystallization of the sample, creating long-range disorder in the structure that resulted in an increased FWHM value for the MAH160 sample. Such long-range disorder causes disturbances in the crystal lattice that alter the value of the band gap energy and, consequently, alter the PL spectra.

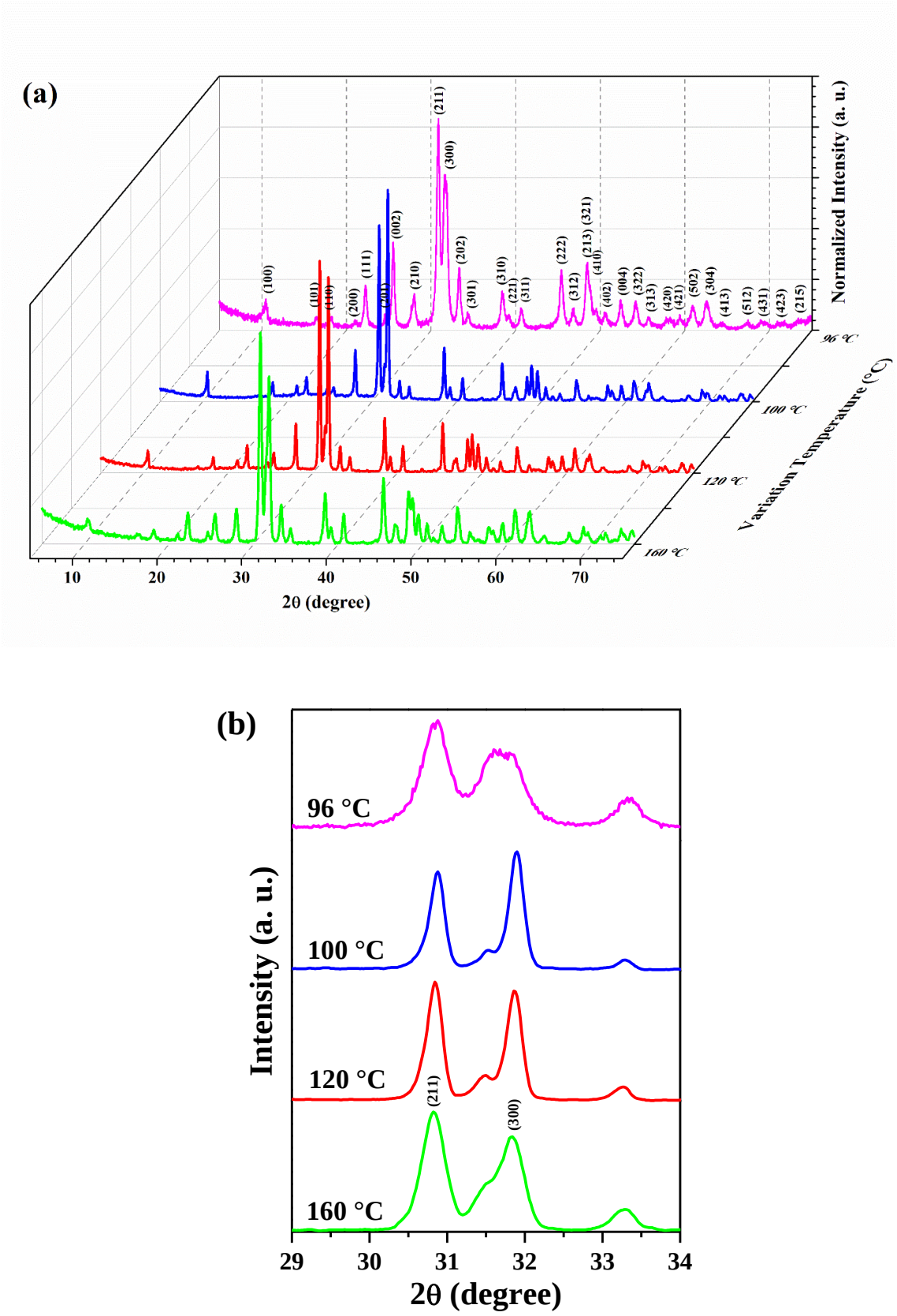

FIGURE 3.1 - (a) XRD patterns of the $Ca_{10}V_6O_{25}$ samples and (b) Magnification of the (211) and (300) planes for samples obtained by the CP method at 96 °C and the MAH method at temperatures of 100, 120, and 160 °C.

It was observed that temperature variations provoked changes of the planes, manifested in the XRD patterns, that can be associated with differences in the crystallographic orientation. FIGURE 3.1a shows an inversion in intensity in some planes for the CP96 sample, as observed for the 25.5° peak corresponding to the (002) plane. Thus, temperature has a strong influence on surface modification that will be preferentially exposed in the material.

The Rietveld refinement calculation method was performed using the GSAS program [93, 94]. FIGURE A1 and TABLE A1 (see in Appendix A, Supplementary Information) show the modifications to the experimental lattice parameters and unit cell volumes of the $Ca_{10}V_6O_{25}$ samples, with respect to influences of the respective synthetic method and reaction temperatures. The $Ca_{10}V_6O_{25}$ structure does not have a Crystallographic Information File (CIF), so a card presenting the same structure (hexagonal) and space group ($P6_3/m$) was used. The Inorganic Crystal Structure Database (ICSD) card No. 24100 [95] of the mineral chromate–apatite with chemical formula structural $Ca_5(CrO_4)_3OH$ was used, as it has a similar crystallographic structure. The difference between the observed (Y_{Obs}) and calculated (Y_{Calc}) XRD patterns revealed a small difference near zero, as observed in the line $Y_{Obs} - Y_{Calc}$ (see FIGURE A1). The fitting parameters, R_{Bragg} e χ^2, indicate that the refinement results were reliable to describe $Ca_{10}V_6O_{25}$ structures. The structural refinement confirmed that the $Ca_{10}V_6O_{25}$ material has a hexagonal structure. TABLE A1 shows the lattice parameters and unit cell volumes for the $Ca_{10}V_6O_{25}$ samples, which agree with previously reported values [86].The values for the unit cell volume and lattice parameters of the sample prepared by the MAH method at 160 °C were increased compared to those of samples obtained at lower temperatures (96, 100, and 120 °C). Thus, as temperatures increased to 160 °C, changes in the structural organization of the $[CaO_6]$ and $[VO_4]$ clusters rendered reduced network symmetry and long-range ordering. Additionally, the resulting structural distortions led to defects, such as

oxygen vacancies, stresses, and strains on the crystalline lattice, that affected the PL property.

Theoretical calculations were performed to identify the influence of synthesis temperature on the resultant material structure. TABLE 3.1 shows the theoretical values for the lattice parameters and the cell volume for the $Ca_{10}V_6O_{25}$ hexagonal structure at different temperatures: 80, 100, 120, 140, 160, and 180 °C [86]. The gradual increase in the synthesis temperature was shown to provoke an expansion in unit cell volume. This increased volume is in agreement with the experimental values presented in TABLE A1. The phonons are responsible for the appearance of structural distortions in $[CaO_6]$ and $[VO_4]$ clusters of the lattice, accounting for the unit cell expansion.

TABLE 3.1 - Results obtained from theoretical calculations.

T (°C)	a = b (Å)	c (Å)	V (Å^3)
static calc.	9.672	6.979	565.42
80	9.705	6.974	568.86
100	9.706	6.974	568.95
120	9.707	6.973	569.06
140	9.708	6.973	569.19
160	9.710	6.973	569.33
180	9.711	6.973	569.48

FIGURE A2 displays a schematic representation of the $[VO_4]$ clusters of the $Ca_{10}V_6O_{25}$ material, the values of the corresponding bond angles are highlighted. The atomic positions and lattice parameters of the Rietveld refinement were used in the Visualization for Electronic and Structural Analysis program [96, 97] to obtain the symmetry and geometry of the $[CaO_6]$ and $[VO_4]$ clusters. Different distortions can be seen for the O–V–O bond angles in the $[VO_4]$ cluster for the samples prepared at various temperatures. An ordered and

symmetrical material presents [VO_4] clusters of tetrahedral symmetry entirely comprised of 109.5° angles. Thus, all samples exhibited distorted bond angles of the [VO_4] clusters, which reduced symmetry and affected the PL spectrum. Ca^{2+} cations are coordinated by six oxygen anions, forming three different types of polyhedral: [CaO_6] clusters presenting a trigonal prism, pentagonal pyramid, and octahedral symmetry [86]. The bond angles and other geometric details of the octahedral clusters are reported in FIGURE A3.

3.4.2. Short-range structural order: Raman and XANES spectroscopies

The Raman spectra revealed short-range structural order/disorder for the $Ca_{10}V_6O_{25}$ material prepared at different temperatures by both the CP and MAH methods (FIGURE 3.2). In the 351–1062 cm^{-1} range, vibrations associated with the [VO_4] tetrahedron appeared [86]. The bands at 861 and 822 cm^{-1} were assigned to the symmetric stretching vibration of the V–O bond. The band at 796 cm^{-1} is attributable to the antisymmetric stretching vibration mode of the VO_4 [86]. Bands at 406, 389, and 351 cm^{-1} correspond to the bending vibration of the O–V–O bond [98, 99]. Lower-frequency bands between 48 and 273 cm^{-1} are assigned to the Ca^{2+} cation displacements and lattice mode vibrations [99, 100].

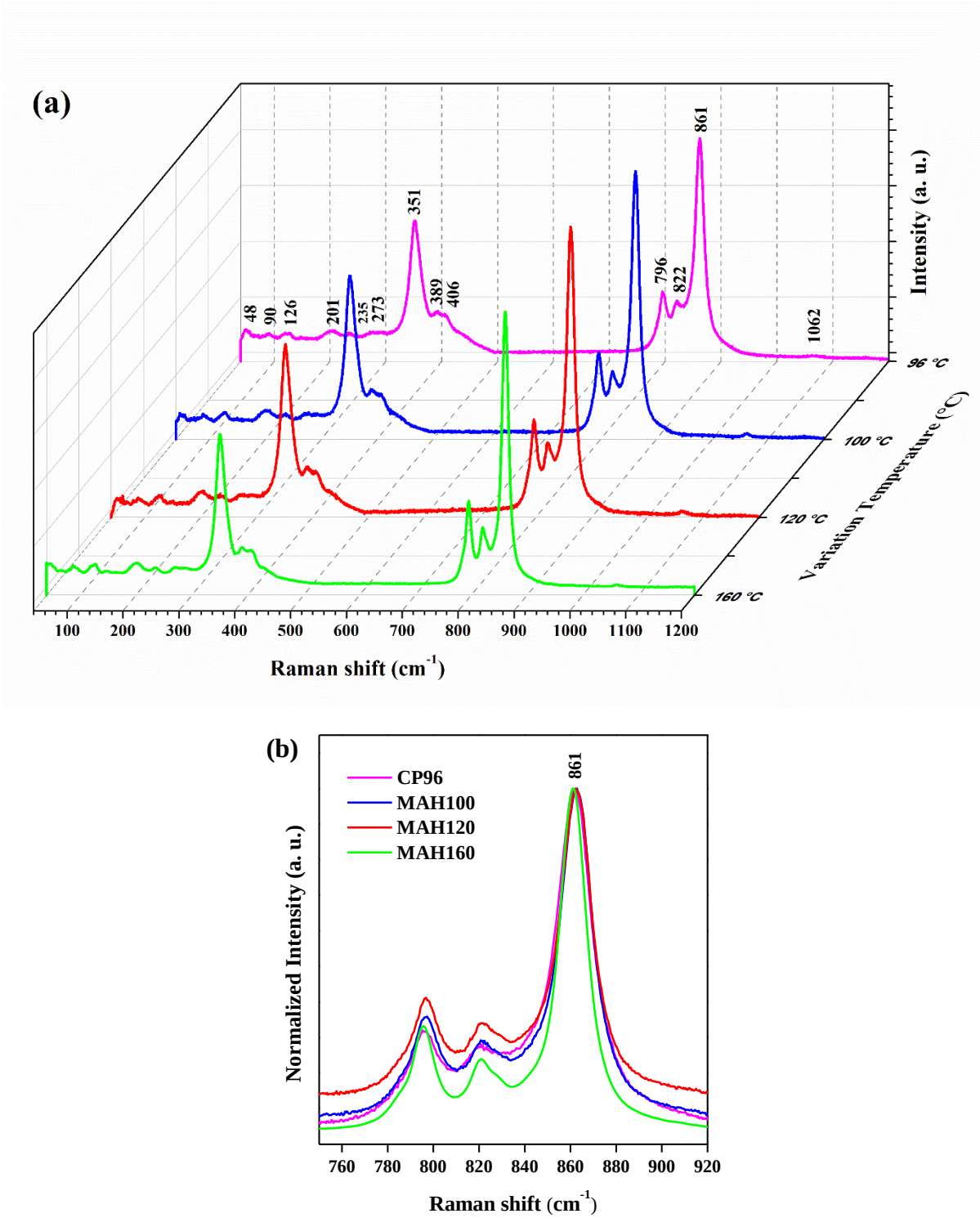

FIGURE 3.2 - (a) Raman spectra of $Ca_{10}V_6O_{25}$ samples obtained via different methods and temperature conditions. (b) Magnification of the region between 750–920 cm^{-1}.

Raman spectroscopy is a useful technique to understand the degree of short-range structural order/disorder owing to its relationship to the local

structural order in the bonding of Ca and V clusters. In this situation, the order/disorder do not extend far beyond the nearest neighbor distances, because of this are characterized by punctual defects. In a perfect crystal, the first-order Raman phonon spectrum exhibits narrow lines that correspond to the Raman allowed zone center (Γ-point) modes, which obey definite polarization selection rules [91]. Considering this, FWHM measurements of the intense band at 861 cm^{-1} were conducted to observe the structural modifications at a short-range for the V–O bond within the [VO_4] cluster (FIGURE 3.2b). For the MAH100, MAH120, and MAH160 samples, the FWHM values were 18.07, 17.59, and 15.14, respectively; whereas for the CP96 sample, the FWHM value was 20.03. Thus, the sample obtained by the CP method displayed a higher FWHM value, indicative of greater distortion in the [VO_4] clusters of the crystal lattice. The high FWHM value is related to a large distortion of the V–O bond, decreasing the symmetry within the [VO_4] cluster. Therefore, samples obtained using the MAH method featured lower FWHM values, indicating that short-range organization increased in the microwaved system as the reaction temperature increased. Short-range motions include the vibrational and rotational movements of the material, which also induces order/disorder in the V–O bond, changing the band gap values of the material; this factor as the long-range is usually responsible for the broadband nature of the PL emissions.

In the past decade, XANES spectroscopy has been used to probe the local order of several compounds and investigate their structural and electronic properties [101-109]. FIGURE 3.3 shows the normalized V-K XANES spectra of three representative vanadium-based reference compounds (V_2O_4, V_2O_5, and Na_3VO_4) and the as-prepared $Ca_{10}V_6O_{25}$ samples examined herein. Chaurand *et al*. revealed that the pre-edge peak could be considered the most useful feature of the XANES spectra, permitting one to determine both the oxidation state and the symmetry of a vanadium species [110]. Indeed, several studies have reported different methods of analysis for discerning the oxidation state and symmetry of vanadium compounds

[108, 110-113]. In several reports, the pre-edge peak is attributed to correspond to the transition from the V 1*s* to the V 3*d* states forbidden by dipole selection rules of centrosymmetric systems, yet allowed in non-centrosymmetric systems via hybridization between V 3*d* and O 2*p* states [108, 111-113].

FIGURE 3.3a shows the difference between XANES spectra for the synthesized samples and reference compounds. Thus, the comparison of pre-edge XANES spectrum for the MAH160 sample with the reference compounds revealed similarities to the Na_3VO_4 spectrum. This demonstrates that V^{5+} atoms are present within the [VO_4] tetrahedral configuration of the MAH160 sample. To verify the influence of temperature on the local structure around V^{5+} cations, the XANES spectra of $Ca_{10}V_6O_{25}$ samples are shown in FIGURE 3.3b. The spectra of the as-prepared samples did not exhibit any significant difference, suggesting a similar local order of the V^{5+} cations for samples obtained at different temperatures.

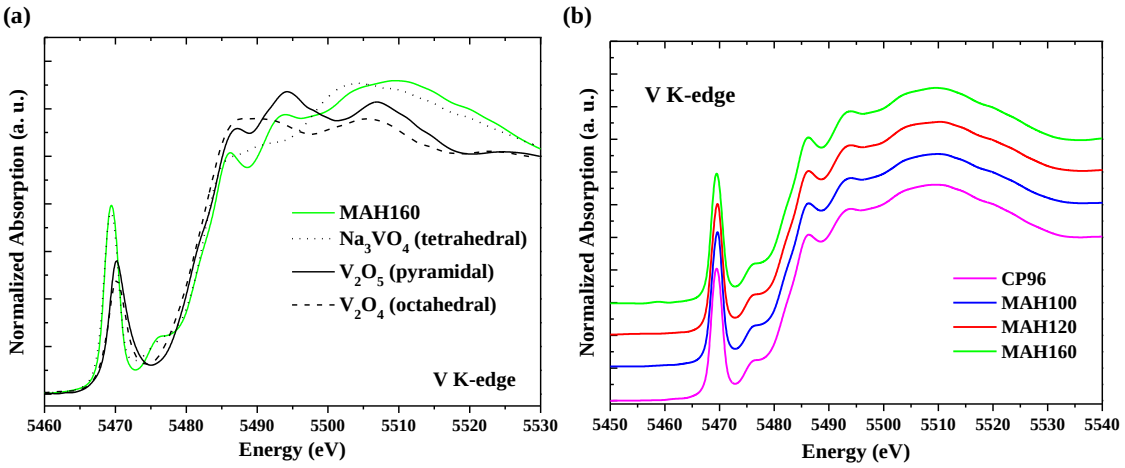

FIGURE 3.3 - Normalized V-K edge XANES spectra of $Ca_{10}V_6O_{25}$ samples. (a) XANES spectra of reference compounds and $Ca_{10}V_6O_{25}$ treated at 160 °C. (b) Samples treated at various temperatures.

3.4.3. Morphology of $Ca_{10}V_6O_{25}$

FIGURE 3.4 illustrates the morphology of $Ca_{10}V_6O_{25}$ samples obtained via various methods and synthesis temperatures. The morphological changes of the $Ca_{10}V_6O_{25}$ crystals were a result of various synthetic temperatures. Samples prepared by the CP method at 96 °C for 1 h exhibit micrographs similar to a straw bundle that is connected to the center of the particle. The particles are microstems with a mean width of 0.08 ± 0.019 μm. When the material was subjected to MAH processing at 100 °C for 1 h, the microwave radiation favored a definition of the stems with a mean width of 0.083 ± 0.023 μm. With an increase in temperature to 120 °C, the stems disaggregated from the straw bundles and become larger, displaying a mean width of 0.802 ± 0.202 μm. At a reaction temperature of 160 °C using the MAH method, the microwave radiation favored a greater disaggregation of stems as the dissolution and recrystallization of the particle. The stems had a mean width of 0.231 ± 0.091 μm.

In the CP method, there is a high degree of disorder of the particles because the effective shocks between hydrated ionic clusters are random in nature. The crystal grows randomly and with a high defect density. When these crystals are treated in the MAH method, there is a continual dissolution and recrystallization. Microwaves associated with the phonon effect (temperature) directly influence the order and disorder of the crystal surfaces, generating a new agglomeration order in the polycrystalline system. Our observations indicate that the crystals decrease in interaction and growth. Therefore, the increase in reaction temperature and the microwave radiation for the MAH-derived samples caused a decrease in the interaction of the stems, and the straw bundle morphology was undone.

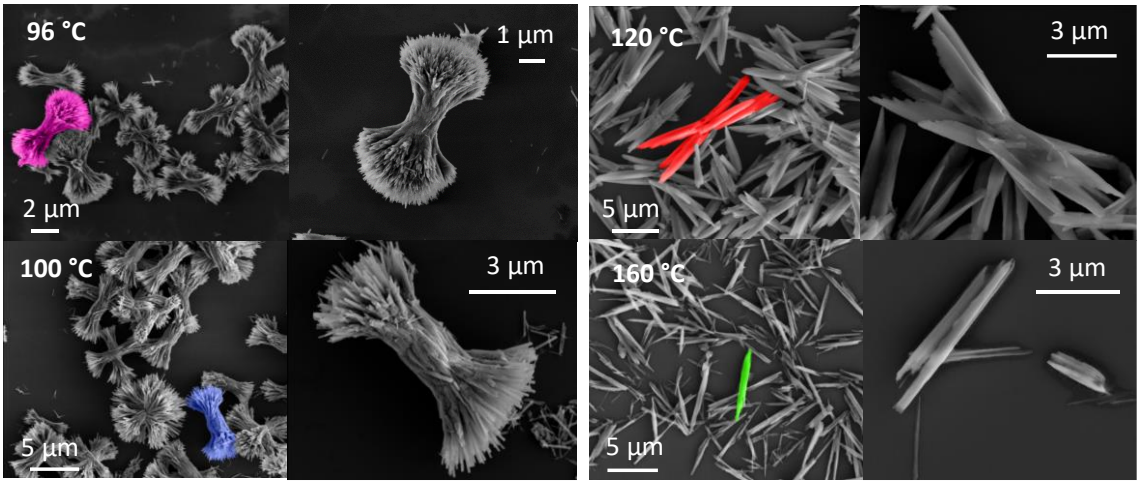

FIGURE 3.4 - FE-SEM images for $Ca_{10}V_6O_{25}$ material obtained by the CP method at 96 °C and MAH method at temperatures of 100, 120, and 160 °C.

All samples exhibited the formation of stems, involving the presence of growth processes to render different 1D morphologies. Specifically, the microwave radiation used during the MAH method greatly influences the morphology of the resulting particles. Effective shocks and particle growth are altered in an open system (i.e., CP method) and a closed system (i.e., MAH method), thus altering the order/disorder at both the short- and long-range of $[CaO_6]$ and $[VO_4]$ clusters, effectively breaking the symmetry of clusters and changing the exposed face in morphology; as a consequence, the morphology of the $Ca_{10}V_6O_{25}$ can be modified by changing the temperature and the synthesis method.

FIGURE A4 shows the chemical composition map obtained by EDX mapping for the $Ca_{10}V_6O_{25}$ samples. The images were constructed by analyzing the energy released from the emission of elemental Si, O, Ca, and V; this method indicates their distribution within the samples. In the images, green, red, yellow, and blue were used to highlight the silicon, oxygen, vanadium, and calcium, respectively. Thus, it can be observed that all the samples had a homogeneous composition of calcium, vanadium, and oxygen.

3.4.4. Medium-range structural order: UV-vis diffuse reflectance and PL

The optical band gap energies (E_{gap}) of the $Ca_{10}V_6O_{25}$ samples are shown in FIGURE 3.5. The E_{gap} values of the samples were obtained by Equation (3), which relates the Kubelka–Munk (1) and Wood–Tauc (2) functions [114, 115].

$$F(R) = \frac{(1-R)^2}{2R} = \frac{k}{s} \quad (1)$$

$$\alpha h\nu = C_1(h\nu - E_{gap})^n \quad (2)$$

$$[F(R)h\nu]^2 = C_1(h\nu - E_{gap}) \quad (3)$$

where *F(R)* is the Kubelka–Munk function of the sample, *R* is the reflectance of a thick enough layer, *k* is the molar absorption coefficient, and *s* is the scattering coefficient. In the Wood–Tauc function, α is the linear absorption coefficient of the sample, $h\nu$ is the photon energy, C_1 is a proportionality, E_{gap} is the optical band gap constant, and *n* is a constant associated with different types of electronic transitions. For the $Ca_{10}V_6O_{25}$ superstructure, a direct transition was considered; therefore, n = ½. The plot of $[F(R)h\nu]^2$ versus $h\nu$ provided the E_{gap} values by linear extrapolation of the UV-vis curve.

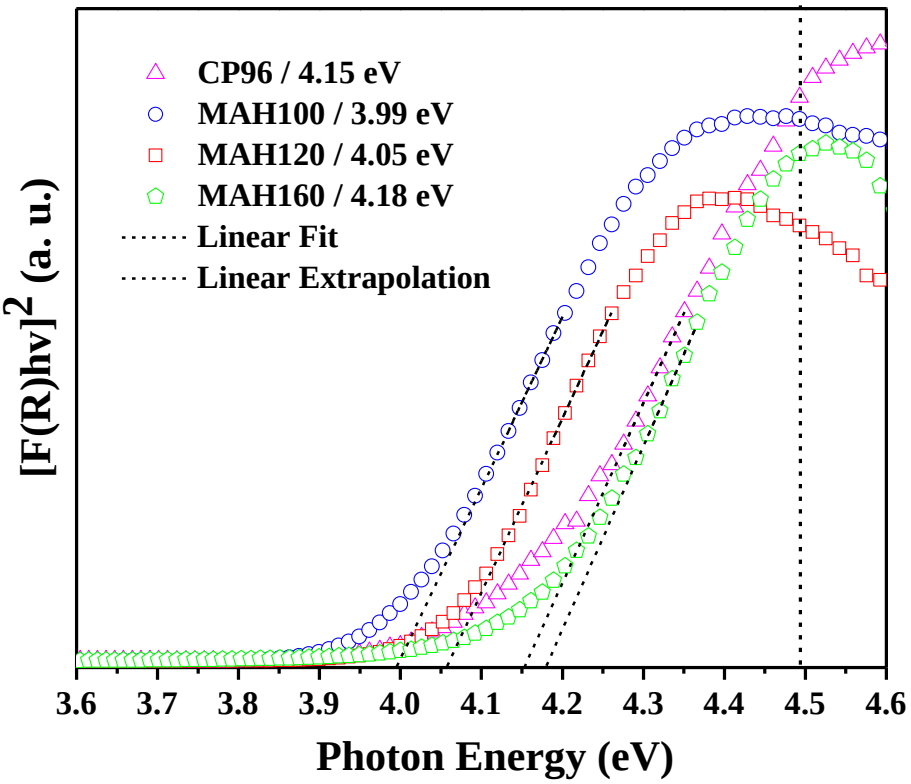

FIGURE 3.5 - UV−vis spectra for $Ca_{10}V_6O_{25}$ material obtained by the CP method at 96 °C and the MAH method at temperatures of 100, 120, and 160 °C.

All $Ca_{10}V_6O_{25}$ samples exhibited near absorbance approximately 300 nm with E_{gap} values between 3.99 and 4.18 eV. All samples absorbed a high fraction of photons in the ultraviolet region. According to the Wood–Tauc theory, an ordered and crystalline material presents a sharp vertical curve (dashed curve); for the $Ca_{10}V_6O_{25}$ structure, a E_{gap} of approximately 4.5 eV would be expected. All samples had a sloped UV-vis curve, with a decrease in E_{gap} values associated with the presence of structural defects in the medium-range. An ideal semiconductor absorption should present a vertical line for an electronic transition; in contrast to that predictions, all samples had a high defect density owing to the remarkable inclination of the Urbach tail [116]. This tail appeared in disordered materials as a result of the formation of localized states (defects) extended in the band gap. It is hypothesized that these defects, resulting from short- and medium-range distortions on the $[CaO_6]$ and $[VO_4]$ clusters, perturb the energy level distribution in both the conduction band (CB) and valence band (VB); thus, the band gap

values were changed. The short-range distortions propagate at medium-range by the interaction between neighboring clusters, favoring the formation of intermediary energy levels inside the band gap of materials; this commonly favors the development of broadband emission.

FIGURE 3.6 shows the PL spectra at room temperature with a laser excitation of 350 nm, and the CIE chromaticity diagram for $Ca_{10}V_6O_{25}$ samples prepared at temperatures of 96, 100, 120, and 160 °C. The PL spectra from the $[VO_4]$ tetrahedral clusters are well established in the literature, with a broadband emission centered near 520 nm [61, 65, 79, 80]. The PL property is justified by the charge transitions in the $[VO_4]$ cluster of tetrahedral symmetry, which has the ground state $^1A_1$ and excited states $^1T_1$, $^1T_2$, $^3T_1$, and $^3T_2$. The luminescence of the vanadium-based oxides is caused by charge transitions in the states ($^3T_1$, $^3T_2$) → $^1A_1$, where broadband in the visible region is defined as the 400–720 nm range. The luminescence mechanism of these materials is assigned by a charge transfer within the $[VO_4]^{3-}$ group, between the 2*p* orbital of O anion of the valence band for the 3*d* orbital of the V cation of the conduction band [61, 79]. For all $Ca_{10}V_6O_{25}$ samples synthesized at different temperatures, a broadband PL with different emission centers was observed (see FIGURE 3.6a). This is indicative that the distribution of the $[VO_4]^{3-}$ groups is not uniform in the crystal lattice, and there is a possibility of defect centers [79].

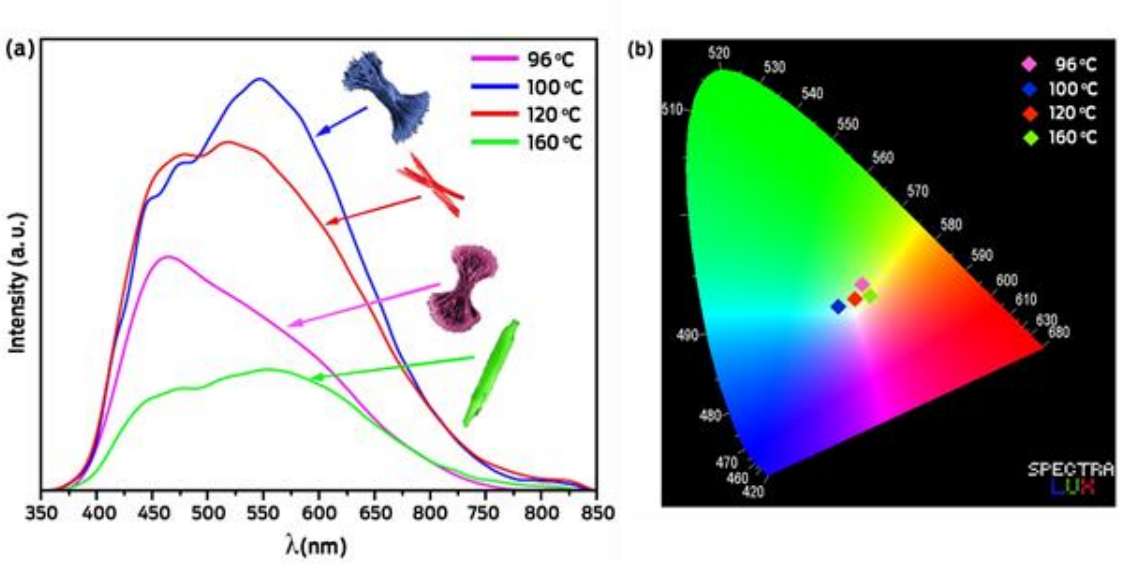

FIGURE 3.6 - (a) PL spectra at room temperature (λ_{ex} = 350 nm) and (b) CIE chromaticity coordinates of the PL spectra for $Ca_{10}V_6O_{25}$ samples obtained by the CP method at 96 °C and the MAH method at temperatures of 100, 120, and 160 °C.

Theoretical calculations have shown that PL emissions also has an important influence on the structural distortions at the [CaO_6] clusters and, especially, in the distorted tetrahedral [VO_4] clusters [86]. The short-, medium-, and long-range structural order/disorder form distorted clusters [VO_4]$_d$, [CaO_6]$_d$ and ordered clusters [VO_4]$_o$, [CaO_6]$_o$; these clusters give a high probability of electron transition ($^3T_1$, $^3T_2$) → $^1A_1$. The short-range disorder forms a density of local defects in the bonds between vanadium and calcium atoms that decreases the symmetry of [CaO_6] and [VO_4] clusters. This intra-cluster interaction occurs by means of the polarization processes induced by the permanent dipole moment of neighboring clusters. This interaction provokes a medium-range disorder related to the rotational motion of the permanent moments in different frameworks formed by the [VO_4]-[CaO_6], [VO_4]-[VO_4], or [CaO_6]-[CaO_6] clusters. From these relationships, the structural disorder extends throughout the crystal lattice (long-range disorder) by dispersion interactions due to correlations between electrons located in the neighborhood of [CaO_6] or [VO_4] clusters [92, 117]. Thus, the

interactions between clusters with distorted symmetry, $[VO_4]_d$ and $[CaO_6]_d$, form new intermediate energy levels within the band gap of the material, favoring broadband emission. Therefore, the structural order/disorder provokes an electronic redistribution of energy levels in both the VB and CB; these redistributions induce a change in the band gap and influence the intrinsic PL. A higher disorder structure at the long-, medium-, and short-range favored a more energetic emission for PL bands in the blue region, as was seen for the CP96 sample. The processing of samples by the MAH method at temperatures of 100 °C and 120 °C increased the crystallinity at both the long- and short-range and benefited the PL intensity for these samples. The increase in the temperature to 160 °C (MAH method) induced dissolution and recrystallization processes that separated stems from the straw bundles. Thereby, an increase in temperature during the MAH method, resulting in different PL properties. The effect of the interaction between stems was practically eliminated, although the separation of the stems caused defects on the surface of the semiconductor. The results of PL indicate a decrease in structural defects (decreased PL in the blue and green regions) with the maintenance of oxygen vacancies. Thus, disorder in both the long- and short-range induced the formation of localized defects (quantum dots disorder) in the material. A quantum dot disorder in the $[CaO_6]$ and $[VO_4]$ clusters favors the formation of different surfaces (oxygen vacancies). Therefore, particles with different morphologies and sizes exhibit different PL properties.

Variations in the reaction temperature and morphological changes in the particles have an influence on the PL properties of the resultant material. To evaluate the performance of the $Ca_{10}V_6O_{25}$ materials to emit colors via luminescence, the CIE chromaticity diagram was investigated (FIGURE 3.6b). The PL spectrum of the CP96 sample, that with higher structural disorder at both the long and short ranges, exhibited a shift to smaller wavelengths—*i.e.*, higher energy. The CIE color coordinates conveyed that the emission was essentially green (x = 0.364 and y = 0.387). Samples prepared by the MAH method favored

displacement to higher wavelengths and lower energy and favored long-, medium-, and short-range order–disorder equilibria within the crystal structure of the MAH100 and MAH120 samples. Thus, MAH samples showed emissions in the white region, as indicated by the CIE color coordinates, MAH100 (x = 0.311 and y = 0.348) and MAH120 (x = 0.350 and y = 0.368). According to the literature, CIE coordinates of the more balanced white-light region of the diagram are in the ranges x = 0.28 – 0.35, y = 0.30 – 0.37 [118, 119]. Thus, the samples produced by reaction temperatures of 100 °C and 120 °C have chromatographic coordinates corresponding to a pure white-light-emitting material. Increased temperatures (160 °C) used during MAH-based synthesis, resulting in the MAH160 sample, increases the long-range disorder of the crystal lattice. Thus, a shift in the chromatographic coordinates was observed to x = 0.374 and y = 0.375; this shift is indicative of the white emission being nearer the yellow region. In this way, the different distortions in long-, medium-, and short-range for both the [VO_4] and [CaO_6] clusters modulate the luminescence properties of $Ca_{10}V_6O_{25}$ samples prepared by various methods and temperatures.

FIGURE 3.7 shows the normalized PL spectra for the $Ca_{10}V_6O_{25}$ samples as a function of the temperature in the range of 30–300 K. $Ca_{10}V_6O_{25}$ samples prepared by different synthesis temperatures have similar emission bands. Thus, these transitions (PL bands) are characteristic of the material structure. To understand in more detail its properties, the temperature dependence of these PL bands was investigated for all samples. A reduction of linewidth was observed at lower temperatures (<150 K), see FIGURE 3.7b, as expected. Enhancement of PL intensity and dominance of the red emission band were also noted at lower temperatures; this red emission is usually attributed to defects of oxygen vacancies in the material or an increase in the V–O bond length to decrease the values of the transition energies ΔE [61, 120, 121]. FIGURE A5 indicates that all $Ca_{10}V_6O_{25}$ samples display an increase in V–O bond length to values between 1.76 and 1.82 Å, favoring the formation of oxygen vacancies and,

consequentially, structural distortions at the [VO_4] clusters. Furthermore, distinct organizations of intermediary energy levels within the band gap contribute to the luminescence in the red and orange coordinate regions, see FIGURE 3.7a. Higher-energy emission bands dominate at higher temperatures, see FIGURE 3.7b. The increase in temperature has likely favored bluish-green and yellow luminescence, characteristic of an electronic transition within the [VO_4] cluster, notably the transition of states ($^3T_1$, $^3T_2$) → $^1A_1$, FIGURE 3.7a [65, 78, 79, 122]. Thermally active phonons may have facilitated the excitation electrons previously trapped in oxygen's 2*p* orbital to the 3*d* orbital of vanadium. At temperatures above 150 K, the transition in PL bands of more energetic levels is favored.

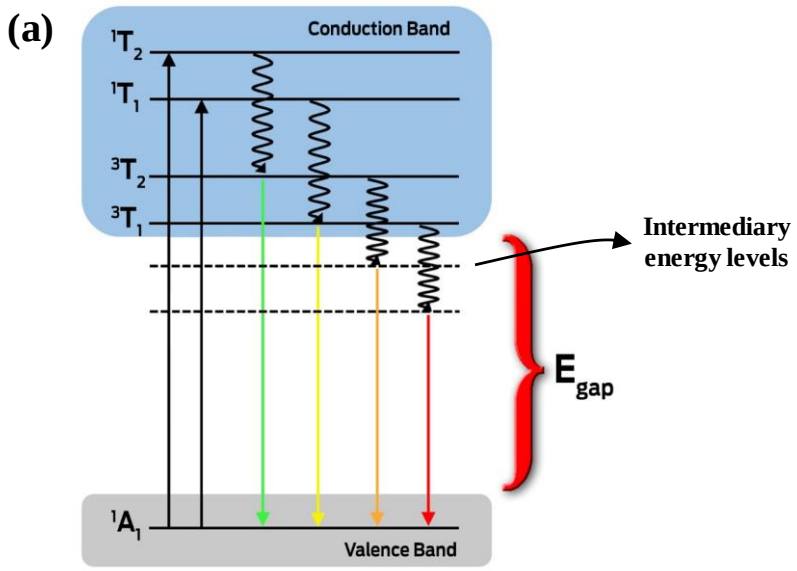

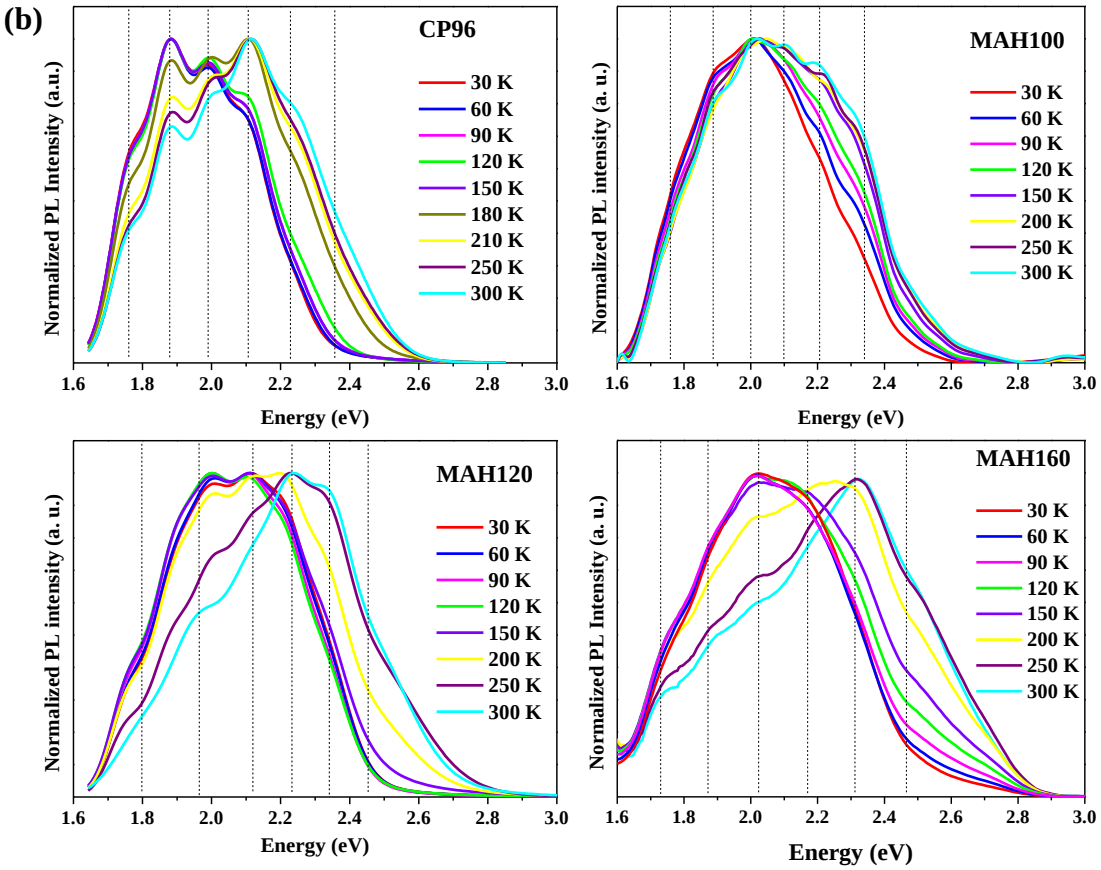

FIGURE 3.7 - (a) PL mechanism and (b) temperature dependence of the normalized PL spectra for the $Ca_{10}V_6O_{25}$ samples obtained by the CP method at 96 °C and the MAH method at 100 °C, 120 °C, and 160 °C under excitation at 325 nm.

All $Ca_{10}V_6O_{25}$ samples exhibited transitions corresponding to the $[VO_4]$ cluster, but with small displacements in the emission centers that are indicative of possible differences in the microstructural organization of the $[VO_4]$ tetrahedron via various distortions, as was noted by the Rietveld refinement. These distortions in the $[VO_4]$ cluster are strongly influenced by order/disorder effects in $[CaO_6]$ clusters (FIGURE A3).

All samples presented a decrease in the emission intensity when the temperature was increased from 30 to 300 K (FIGURE A6) [61, 62, 79]. The observed thermal quenching of the phosphors may be explained by the schematic diagram shown in FIGURE 3.8a [123]. As previously shown in FIGURE 3.7, the excited state

of the $[VO_4]^{-3}$ group is exists as two near-degenerate energy levels (^{1}T and ^{3}T) [61, 78, 80]. The excited electron from the ground state (point 1) to the ^{1}T level of the excited state (point 2) and is generally transferred to the ^{3}T energy level (point 4); after reaching the ^{3}T state, the electron then returns to the ground state (point 5) by a radiative transition, as illustrated in FIGURE 3.8a. However, when the temperature is increased, the electron may return to the ground state (^{1}A) by means of a non-radiative transition. Thus, the electron is thermally activated from Point 4 in the schematic to the crossover of the excited state and the ground state at Point 6. Therefore, the excited electron can easily transfer to the ground state by non-radiative means via energy transfer of phonon; thus, increasing temperatures quench emission transition from Point 4 to Point 5. As a consequence, the luminescence intensity of the phosphor decreases via a processes referred to as "thermal quenching" [123-125]. The energy required to thermally activate the excited electron from Point 4 to Point 6 via activation energy, ΔE_a, can be obtained by:

$$I(T) = \frac{I_0}{1 + \gamma e^{-\frac{E_{at}}{k_B T}}}$$

where k_B is the Boltzmann constant (8.617×10^{-5} eV K^{-1}), I_0 is the photoluminescence intensity of the $Ca_{10}V_6O_{25}$ samples at 0 K, I(T) is intensity at a given temperature, γ is the ratio between radioactive and nonradioactive lifetimes, and E_{at} is the activation energy of the thermal-quenching process. Generally, a lower value of ΔE_a leads to a higher probability of non-radiative transitions.

FIGURE 3.8b,c show the Arrhenius plots for all observed emission bands within the PL spectra for the MAH120 sample. The obtained activation energy is approximately 2 meV for all bands of the $Ca_{10}V_6O_{25}$ sample produced by the MAH method at 120 °C. Similar values were also obtained for all other samples (see Appendix A, Supplementary Information), indicating important non-radiative transitions occurring within $Ca_{10}V_6O_{25}$.

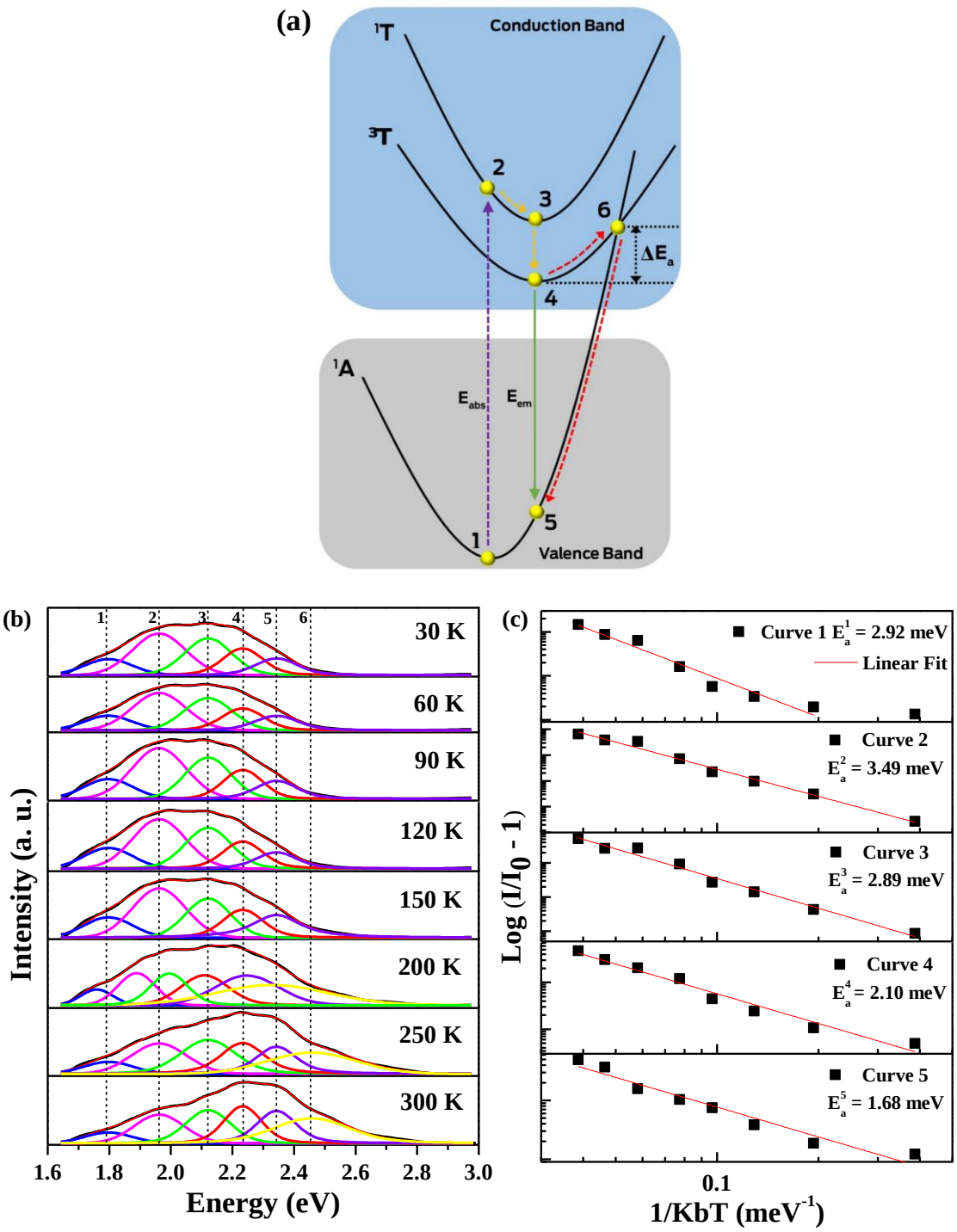

FIGURE 3.8 - (a) Electronic transition diagram of the $[VO_4]^{3-}$ group. (b) Deconvolution of the PL band spectrum using the Voigt Area G/L function. (c) Arrhenius plots of log $((I_0/I) - 1)$ versus $1/k_BT$. The $Ca_{10}V_6O_{25}$ sample obtained by MAH method at 120 °C.

3.5. Conclusion

To explore the use of promising new phosphorescent compounds, we report on the successful synthesis of $Ca_{10}V_6O_{25}$ structures with various morphologies via the CP and MAH methods at different temperatures. XRD patterns, Rietveld refinement, and Raman spectroscopy were all used to confirm the formation of a $Ca_{10}V_6O_{25}$ compound with a hexagonal structure that displays different degree of order/disorder at both short and long ranges. XANES spectroscopy revealed the presence of V^{5+} coordinated by four oxygen atoms in a tetrahedral configuration. FE-SEM images showed that variation in the temperature was favorable to obtain $Ca_{10}V_6O_{25}$ with different morphologies, an increase in temperature to 160 °C caused a decrease in interactions between particles, thereby modifying the morphology. EDX mappings showed that all samples had a homogeneous distribution of elemental Ca, V, and O. UV-vis DRS measurements revealed that all samples displayed a medium-range lattice disorder responsible for broadband emissions. Thus, the samples presented different morphologies and structural order/disorder that favorably produced optical properties beneficial for white-light application. Therefore, distortions in the lattice and changes in the morphology of $Ca_{10}V_6O_{25}$ can tune the electronic transitions within the material through the formation of energy states within the band gap; this state benefits the broadband PL emission, which involves the participation of numerous photons generating a white-light emission that is potentially applicable in UV chip excited WLEDs. However, for this application more research to realize practical UV chip excited WLEDs is necessary.

4. Computational Chemistry Meets Experiments for Explaining the Geometry, Electronic Structure, and Optical Properties of $Ca_{10}V_6O_{25}$

4. COMPUTATIONAL CHEMISTRY MEETS EXPERIMENTS FOR EXPLAINING THE GEOMETRY, ELECTRONIC STRUCTURE, AND OPTICAL PROPERTIES OF $Ca_{10}V_6O_{25}$

Mayara Mondego Teixeira[1*], Regiane Cristina de Oliveira[1], Marisa Carvalho Oliveira[1,2], Renan Augusto Pontes Ribeiro[3], Sergio R. de Lazaro[3], Máximo Siu Li[4], Adenilson J. Chiquito[5], Lourdes Gracia[6], Juan Andrés[2] and Elson Longo[1].

[1]CDMF-UFSCar, Universidade Federal de São Carlos, P.O. Box 676, 13565-905 São Carlos, SP, Brazil.

[2]Departamento de Química Física i Analítica, Universitat Jaume I, 12071, Castelló de la Plana, Spain.

[3]Departamento de Química, Universidade Estadual de Ponta Grossa, Av. General Carlos Cavalcanti, 4748, 84030-900, Ponta Grossa, PR, Brazil.

[4]IFSC-Universidade de São Paulo, P.O. Box 369, 13560-970 São Carlos, São Paulo, Brazil.

[5]Departamento de Física, Universidade Federal de São Carlos, Rod. Washington Luiz, km 235, CP 676, CEP 13565-905, São Carlos, SP, Brazil.

[6]Departamento de Química Física, Universitat de València, 46100, Burjassot, Spain.

4.1. Abstract

In this paper, we present a combined experimental and theoretical study to disclose, for the first time, the structural, electronic, and optical properties of $Ca_{10}V_6O_{25}$ crystals. The microwave-assisted hydrothermal (MAH) method has been employed to synthetize these crystals with different morphologies, within a short reaction time at 120 °C. First-principle quantum mechanical calculations have been performed at the density functional theory level to obtain the geometry and electronic properties of $Ca_{10}V_6O_{25}$ crystal in the fundamental and excited electronic states (singlet and triplet). These results, combined with the measurements of X-ray diffraction (XRD) and Rietveld refinements, confirm that the building blocks lattice of the $Ca_{10}V_6O_{25}$ crystals consist of three types of distorted 6-fold coordination [CaO_6] clusters: octahedral, prism and pentagonal pyramidal, and distorted tetrahedral [VO_4] clusters. Theoretical and experimental results on the structure and vibrational frequencies are in agreement. Thus, it was possible to assign the Raman modes for the $Ca_{10}V_6O_{25}$ superstructure, which will allow us to show the structure of the unit cell of the material, as well as the coordination of the Ca and V atoms. This also allowed us to understand the charge transfer process that happens in the singlet state (s) and the excited states, singlet (s^*) and triplet (t^*), generating the photoluminescence emissions of the $Ca_{10}V_6O_{25}$ crystals.

4.2. Introduction

The members of the calcium vanadate family, such as $Ca_{0.5}V_3O_8$ [126], CaV_4O_9, CaV_3O_7 and CaV_2O_5 [127], CaV_2O_6 [14], $CaVO_3$, CaV_6O_{16} [84], $Ca_2V_2O_7$ [128], $Ca_3V_2O_8$ [129], $Ca_4V_4O_{14}$, $Ca_7V_4O_{17}$ [130], and $Ca_{10}V_6O_{25}$ [16, 83, 84] have attracted increasing interest, because of their structure, compositional diversity, and physical and chemical properties, which facilitate a wide range of technological

applications in the fields of magnetism, electrochemistry, catalysis, and optical devices [13, 16, 82, 83, 126, 127, 131-133].

In particular, $Ca_{10}V_6O_{25}$ has drawn attention, because of its geometric structure, in which both Ca and V cations adopt different local coordinations [16, 84], with a promising potential in electronic, biomedical, and semiconductor applications [16, 134]. Moreover, Pei et al. [83] observed that the $Ca_{10}V_6O_{25}$ nanorod modified glassy carbon electrode, which presents good performance in the electrochemical detection of tartaric acid, is promising for the development of electrochemical sensors for tartaric acid: However, information about its structure and related materials is scarce and incomplete [13, 16, 83, 84, 134, 135]. For related compounds, Adams and Gardner [136] analyze the single-crystal vibrational spectra of apatite ($Ca_5(PO_4)_3F$), vanadinite ($Pb_5(VO_4)_3Cl$), and mimetite ($Pb_5(AsO_4)_3Cl$). Petit et al. [98] synthesized $Ca_{10}(PO_4)_{6-x}(VO_4)_x(OH)_2$ (where $0 \leq x \leq 6$) and studied the vibrational modes in related materials. Frost et al. [137] assigned the vibrational modes to vanadinite [$Pb_5(VO_4)_3Cl$]; meanwhile, Bartholomai and Klee [138] resolved the vibrational modes for the apatites pyromorphite [$Pb_5(PO_4)_3Cl$], vanadinite [$Pb_5(VO_4)_3Cl$], and mimetite [$Pb_5(AsO_4)_3Cl$].

For the synthesis of $Ca_{10}V_6O_{25}$ crystals, different authors reported the use of precipitation and hydrothermal methods to obtain crystals with diverse morphologies [16, 83, 84]. In particular, Hojamberdiev et al. [16] synthesized $Ca_{10}V_6O_{25}$ via hydrothermal processing in a basic medium under the pH range of 12.0–13.5, the temperature range of 120–180 °C, and reaction times of 12, 24, and 48 h. These authors concluded that the above reaction parameters have a strong influence on the morphology of the as-synthetized $Ca_{10}V_6O_{25}$ crystals, and they obtained various morphologies, such as rods and spherical, ricelike, and bundled particles. However, these methods require high temperatures, long processing times (from a few hours to a few days), and expensive equipment. However, the use of microwaves has improved the synthesis procedure since materials were obtained at shorter times and lower temperatures. Moreover, there is increased

interest in developing the microwave-assisted hydrothermal (MAH) method, because it has advantages of being a faster, simpler, and more efficient route to obtain single-phase crystals with good reproducibility [139-142]. In this context, by using the MAH method, our group could synthetize various metal oxides, such as $BaZrO_3$ [143], CuO with catalytic activity [144], $SrTiO_3$ with photocatalytic activity [145], and α-Ag_2WO_4 as acetone gas sensors [146].

The present paper reports the synthesis of monophasic $Ca_{10}V_6O_{25}$ crystals by using the MAH method at a temperature of 120 °C within a short synthesis time. The geometry, electronic structure, optical properties, and morphology of the crystals were examined using X-ray diffraction (XRD) patterns with Rietveld refinement, Raman spectroscopy, ultraviolet–visible (UV–vis) diffuse reflectance spectroscopy (DRS), photoluminescence (PL) measurements, transmission electron microscopy (TEM), energy-dispersive X-ray spectroscopy (EDS), field-emission scanning electron microscopy (FE-SEM), and current-voltage measurements. First-principles calculations at the density functional theory (DFT) level were performed to complement the experimental results, in order to elucidate the geometry, electronic structure, and optical properties of $Ca_{10}V_6O_{25}$ crystals. The localization and characterization of the excited singlet and triplet electronic states allows us to rationalize the PL emissions of this material, which are reported for first time in the present work.

4.3. Experimental methods

4.3.1 Synthesis

The synthesis of the $Ca_{10}V_6O_{25}$ crystals follows the procedure proposed by Hojamberdiev et al. [16]: 2 mmol of NH_4VO_3 (≥99.9%, Sigma-Aldrich) was dissolved in 25 mL of distilled water, and heated thereafter at 50 °C under magnetic stirring until the reagent was dissolved completely. Separately, 1.6

mmol of $CaCl_2.2H_2O$ (99.0%–105.0%, synth) was dissolved in 25 mL of distilled water at room temperature. After complete dissolution of the reactants, the solutions were mixed at room temperature and the pH of the solution was adjusted to 12.5 via the dropwise addition of a 6 mol/L KOH aqueous solution. The final volume was adjusted to 70 mL. Subsequently, the solution was stirred for 10 min and thereafter, it was transferred to the MAH system at the temperature of 120 °C and maintained for different time durations of 4, 8, 16, and 32 min. The precipitates formed were collected at room temperature, washed with distilled water until the pH was neutralized, and dried in a conventional furnace at 60 °C for 12 h. The samples obtained after the different time durations were denoted as CaVO-4, CaVO-8, CaVO-16, and CaVO-32, corresponding to the synthesis times of 4, 8, 16, and 32 min, respectively.

4.3.2. Characterizations

$Ca_{10}V_6O_{25}$ samples were characterized by X-ray diffraction (XRD) using a diffractometer (Model DMax/2500PC, Rigaku, Japan), with Cu Kα radiation (λ = 1.5406 Å) in the 2θ range of 5°–75° with a scanning rate of 0.02°/min. The Rietveld refinements using the general structure analysis (GSAS) program, the scan rate of 0.01º/min for 2θ range of 5º–110º. Raman spectroscopy measurements were performed using a spectrometer (Model T64000, Horiba Jobin-Yvon, Japan) coupled to a CCD Synapse detector and an argon-ion laser, operating at 514 nm with a maximum power of 7 mW. The spectra were measured in the wavenumber range of 25–1200 cm^{-1}. Ultraviolet visible (UV-vis) spectra were obtained using a spectrophotometer (Model Cary 5G, Varian, USA) in diffuse reflection mode. The morphologies of the samples were examined using field-emission scanning electron microscopy (FE-SEM) (Supra 35-VP Carl Zeiss, Germany) operated at 15 kV. PL measurements were performed with a Monospec 27 monochromator (Thermal Jarrel Ash, USA) coupled with a R955

photomultiplier (Hamamatsu Photonics, Japan). A krypton ion laser (Coherent Innova 200 K, USA; λ = 350 nm) was used as the excitation source with an incident power of ~14 mW on the samples. All measurements were performed at room temperature. For the Raman, PL, and UV-vis characterizations: the $Ca_{10}V_6O_{25}$ samples, in the powder form, were placed in the respective port samples of each piece of equipment.

For the current-voltage (*I–V*) characterizations, 6-mm-diameter pressed pellets were made and the measurements were performed at room temperature, using silver electrical contacts 75 nm thickness, which were obtained on an evaporator (Model AUTO 306, Edwards) under a pressure of 10^{-7} mbar. The current was determined by a Keithley 6517B electrometer coupled to a probing positioning system.

4.3.3. Computational Methods

Calculations were performed using the periodic ab initio CRYSTAL14 package [147], based on density functional theory (DFT) using hybrid functional of a nonlocal exchange functional developed from Becke, combined with a correlation functional based on the gradient of electronic density developed from Lee, Yang, and Parr (B3LYP) [89, 90]. This computational technique has been successful for the study of the electronic and structural properties of various materials, including vanadates and several other oxides [57, 148-151]. The Ca, V, and O atoms were described by standard atom-centered all-electron basis sets: 86-511d3G, 86-411d4G, and 6-31d1G, respectively [152-154].

Full optimization of the $Ca_{10}V_6O_{25}$ structure was performed. The initial geometry was obtained from XRD experimental results, considering the removal of one O atom in this system through the ATOMREMO option provided by the CRYSTAL program. The convergence criteria for both monoelectronic and bielectronic integrals was set as 10^{-8} Hartree. Regarding the density matrix

diagonalization, the reciprocal space net was described by a shrinking factor set to 4, corresponding to 12 *k*-points within the irreducible part of the Brillouin zone in accordance with the Monkhorst–Pack method [155]. In order to understand the PL mechanism associated with $Ca_{10}V_6O_{25}$ material, both excited singlet states (s*) and excited triplet states (t*) have been localized and characterized, following the previous strategies developed by our group [105, 150, 156-159]. For the s* model, we consider an off-centering V displacement of 0.1 Å in the *z*-direction. In this case, the t* model state was reproduced fixing the difference between spin-up (α) and spin-down (β) ($n\alpha - n\beta = 2$) along the self-consistent field (SCF) calculations. The electronic structure was investigated from band structure and density of states (DOS).

4.4. Results and discussion

4.4.1. XRD and Rietveld Refinements

FIGURE 4.1 and FIGURE B1 (see Appendix B, Supplementary Information) present the XRD patterns and Rietveld refinement plot of the 3D $Ca_{10}V_6O_{25}$ crystals, respectively. The XRD patterns in FIGURE 4.1 show that all of the samples exhibit well-defined peaks suggesting an ordered long-range arrangement in the crystal lattice, for the samples obtained at 120 °C via MAH. The Miller indices of the peaks are in accordance with Joint Committee on Powder Diffraction Standards (JCPDS) No. 52-649 for the $Ca_{10}V_6O_{25}$ phase with a hexagonal structure and the space group of $P6_3/m$, indicating the absence of additional phases. Thus, the efficient internal heating by direct coupling of microwave energy with the molecules was efficient in obtaining the pure $Ca_{10}V_6O_{25}$ phase at a temperature of 120 °C within short reaction times in the MAH method. The Rietveld refinement method was applied to confirm the three-

dimensional (3D) structure of $Ca_{10}V_6O_{25}$. The refinement was performed using the GSAS program [93, 94].

No Inorganic Crystal Structure Database (ICSD) card related to this structure has been reported in the literature. The ICSD No. 24100, for calcium tris(tetraoxochromate(V)) hydroxide, reported by Wilhelmi, K.A. *et al*., has been used, because it has a similar crystallographic structure [95]. The obtained results are displayed in TABLE B1 in the Supplementary Information. The experimentally observed XRD patterns and the theoretically calculated data exhibit small differences near zero on the intensity scale, as illustrated by the line $Y_{Obs}–Y_{Calc}$; moreover, the fitting parameters (R_{Bragg} and χ^2) indicate consistency between the calculated data and observed XRD patterns for the $Ca_{10}V_6O_{25}$ microcrystals obtained at 120 °C. The smaller values of fitting parameters obtained for the CaVO-4 and CaVO-16 samples indicate greater network symmetry and long-range ordering than those of the powders of CaVO-8 and CaVO-32. TABLE B1 shows that the CaVO-4 and CaVO-16 samples present a smaller cell volume, associated with the volume contraction at the unit cell. The lattice parameters (*a*, *b*, and *c*) and bond angle (β) estimated from the refinement confirm the hexagonal structure.

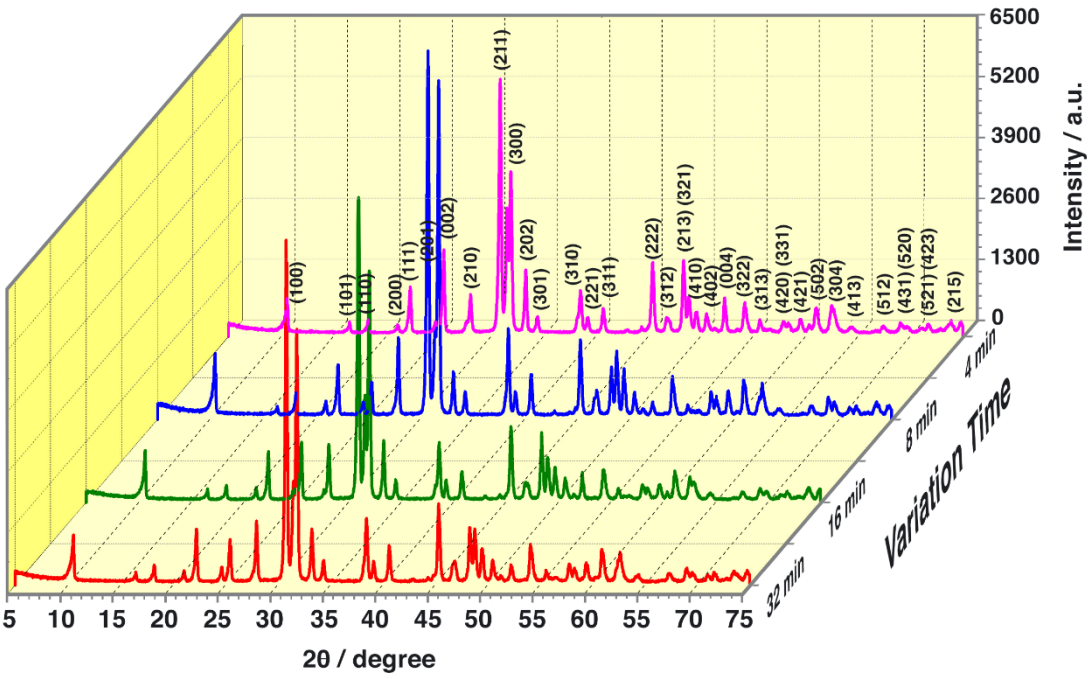

FIGURE 4.1 - XRD patterns and the Miller indices in accordance with JCPDS File No. 52-649 for the $Ca_{10}V_6O_{25}$ processed at 120 °C, as function of synthesis time.

FIGURE 4.2 displays a schematic representation of a hexagonal unit cell of the $Ca_{10}V_6O_{25}$ crystal, modeled from the Rietveld refinement data and optimized with DFT/B3LYP level of theory, in which the symmetry and geometry of the local coordination of Ca and V cations forming the building blocks of this crystal are depicted.

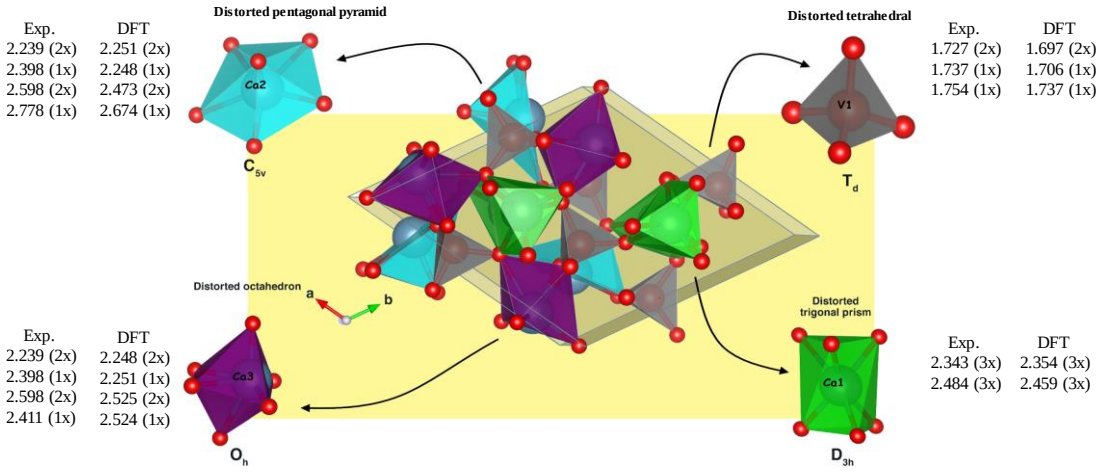

FIGURE 4.2 - Schematic representation of the hexagonal unit cells of $Ca_{10}V_6O_{25}$ showing the local structures for $[CaO_6]$ and $[VO_4]$ clusters (in grey) and the bond lengths (in Å) obtained from Rietveld refinement and DFT calculations. Green, cyan, and purple polyhedrons represent the prismatic, pentagonal-pyramid, and octahedral symmetries associated with $[CaO_6]$ clusters, respectively. The values 1x, 2x and 3x correspond to the bond multiplicity.

The unit cell shown in FIGURE 4.2 was modeled using the visualization system for electronic and structural analysis (VESTA) program (version 3.4.0) for Windows 7-64-bit0 [96, 97]. An analysis of the results indicates that the V cations are coordinated with four oxygen anions to form distorted tetragonal $[VO_4]_d$ clusters, whereas the Ca cations exhibit three types of octahedral $[CaO_6]_d$ clusters with highly distorted geometries. The Ca1, Ca2, Ca3, and Ca4 cations form distorted trigonal prisms, the Ca5, Ca7, and Ca8 cations form distorted octahedra, and the Ca6, Ca9, and Ca10 cations form distorted pentagonal pyramids. Furthermore, it was observed that the theoretical values are consistent with the experimental results. This large variety of V–O and Ca–O bonds and O–V–O and O–Ca–O bond angles is responsible for the order/disorder effects, which are associated with the different degrees of distortion and the wide range of bonding patterns of these clusters. The structural distortions within the

$[CaO_6]_d$ and $[VO_4]_d$ clusters then generate a polarization in the crystal structure, because of the displacement of Ca and V cations.

4.4.2. Raman spectra

The $Ca_{10}V_6O_{25}$ crystal exhibits a hexagonal structure with the space group $P6_3/m$ (C_{6h}^2) and the following vibrational modes:

$$\Gamma = 1A_u + 2E_{1u} + 2B_u + 1E_{2u} + 2A_g + E_{1g} + 2B_g + 3E_{2g}.$$

For a perfect and orderly crystalline structure with this space and point group symmetry, six active Raman modes are expected as follows:

$$\Gamma = 2A_g + E_{1g} + 3E_{2g}.$$

In this study, first-principles calculations predict 123 active Raman and infrared modes for the $Ca_{10}V_6O_{25}$ structure, of which 63 Raman modes match the following decomposition at the Γ point: ($\Gamma = 24A_g' + 24E_g' + 15E_g''$). The experimental vibrational Raman frequencies were obtained in the wavenumber range of 25–1200 cm^{-1}, and all the samples exhibited 13 experimental modes, as shown in FIGURE 4.3. However, some of them are not observed experimentally, because of either overlapping bands or low intensity.

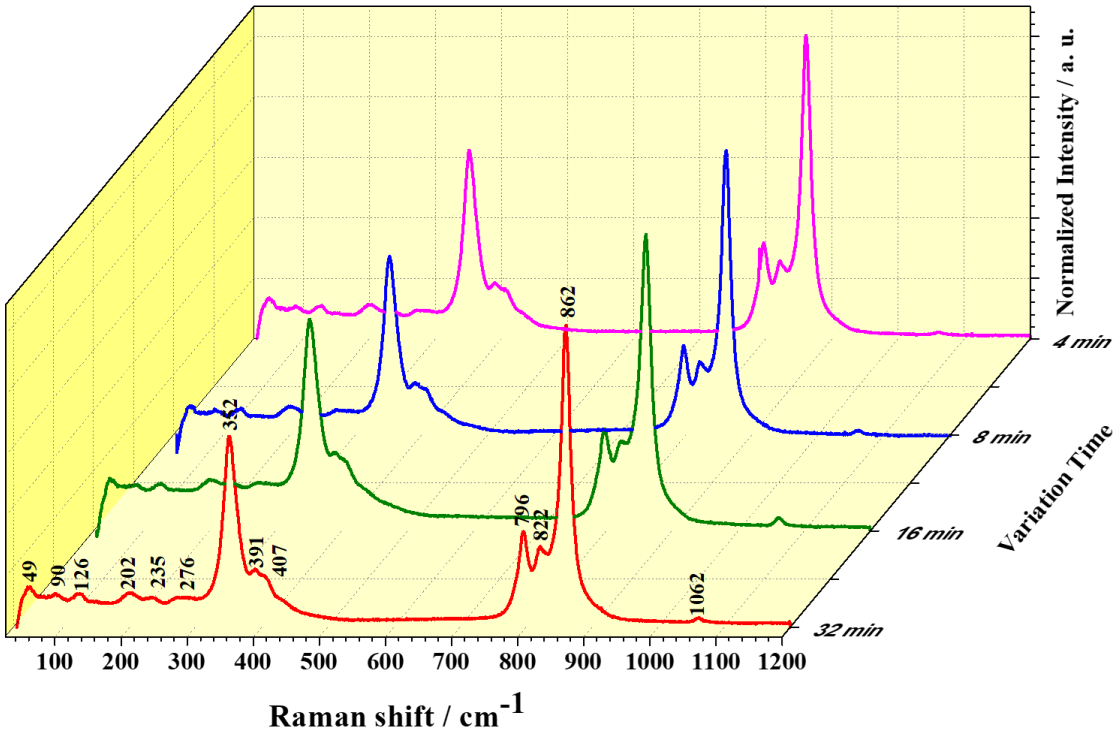

FIGURE 4.3 - Raman spectra in the wavenumber range of 25–1200 cm^{-1} of the $Ca_{10}V_6O_{25}$ crystals processed at 120 °C, as function of synthesis time.

At lower frequencies, the peaks obtained through B3LYP calculations at 89.38 cm^{-1} (exp. 90 cm^{-1}), 124.14 cm^{-1} (exp. 126 cm^{-1}), 204.69 cm^{-1} (exp. 202 cm^{-1}), 237 cm^{-1} (exp. 235 cm^{-1}), and 262.58 cm^{-1} (exp. 276 cm^{-1}) are associated with the lattice modes of $[CaO_6]$ clusters [136]. The intense band at 348.26 cm^{-1} (exp. 352 cm^{-1}) is associated with the A_g mode of bending vibration of the O–V–O bond of ν_3. The peaks at 379.40 cm^{-1} (exp. 391 cm^{-1}) and 400.22 cm^{-1} (exp. 407 cm^{-1}) are assigned to the A_g bending vibration of the O–V–O bond of ν_4. The other band at 796 cm^{-1} is related to the E_{2g} antisymmetric stretching of the VO_4 of ν_3. Moreover, the peaks located at 859.60 cm^{-1} (exp. 822 cm^{-1}) and the most intense band at 867.34 cm^{-1} (exp. 862 cm^{-1}) may be attributed to the A_g symmetrical stretching vibration of the V–O bond of ν_1 [98, 137, 138]. The band located at 1020.96 cm^{-1} (exp. 1062 cm^{-1}) corresponds to the internal modes assigned to the symmetric stretching vibrations of $[VO_4]$ cluster.

As reported in the literature [52, 160], a solid with the local structural order has a sharp, intense, and well-defined vibrational bands. We have compared the full width at half-maximum (fwhm) of the peak of 352 cm^{-1} in the Raman spectra of all the samples (FIGURE B2 in the Supplementary Information). Analysis of these phonon line widths reveals similar structural disorder at the $[VO_4]$ cluster.

TABLE B2 shows the calculated B3LYP frequencies (ω) of the Raman active modes at the Γ point for the $P6_3/m$ structure. The results of the B3LYP calculation present an acoustic mode of zero frequency with E´ symmetry, and an imaginary frequency (–55.02 cm^{-1}), which reveals that the $Ca_{10}V_6O_{25}$ structure optimized in the $P6_3/m$ space group has a structural instability at Γ and corresponds to a saddle point on a very flat potential energy surface after removing an oxygen atom in the initial structure. Various numerical checks (e.g., setting a better energy convergence, strengthening of the optimization criteria, decreasing the symmetry constraints) have been performed to ensure that the negative frequency was not an artifact of the calculations.

4.4.3. Morphology and growth mechanism

Variation in the synthesis time (4, 8, 16, and 32 min) influences the morphology of the $Ca_{10}V_6O_{25}$ crystals (see FIGURE 4.4).

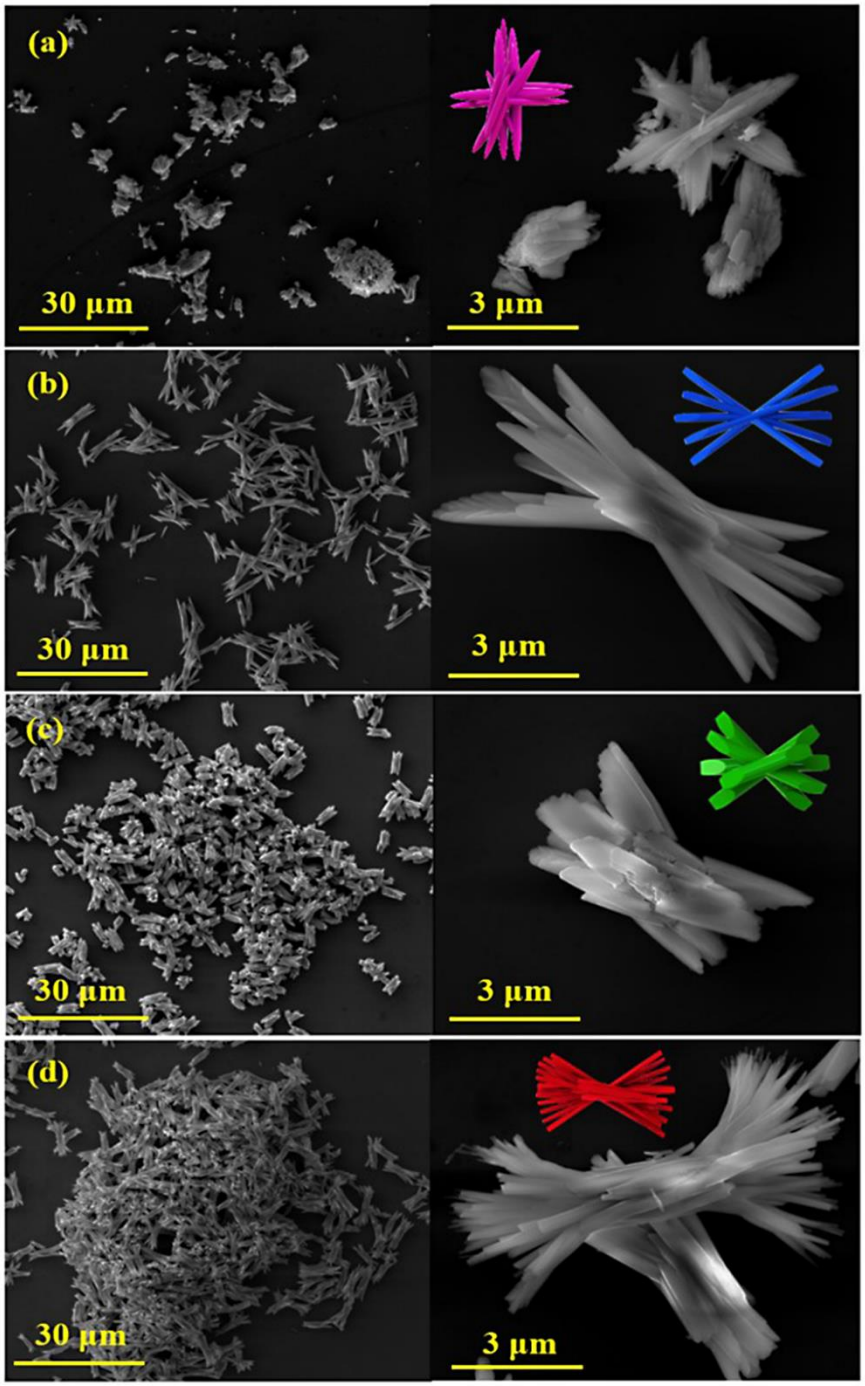

FIGURE 4.4 - Low (30 μm) and high (3 μm) magnification FE-SEM images of the $Ca_{10}V_6O_{25}$ crystals processed at 120 °C as function of synthesis time: (a) 4 min, (b) 8 min, (c) 16 min, and (d) 32 min. Inset illustrates the morphology of the crystals in pink, blue, green, and red.

The growth process can be monitored at different times, maintaining the temperature constant at 120 °C. At 4 min, after the formation of the first

nanoparticles, the oriented growth process of the stems occurred from the agglomerated particles. The small stems grew oriented around a single common center, forming a microparticle in the CaVO-4 sample (FIGURE 4.4(a)). The increase in the synthesis time to 8 min (CaVO-8 sample) favored an elongation of the stems, joined with a length of 6 μm and width of 644 nm, and their stem ends appeared faceted. Thus, the morphology is similar to a straw bundle with two fantails of stems, which are connected to each other in the middle (FIGURE 4.4(b)). During the synthesis, the effect of the microwaves on the particles caused a contraction of the stems (time of 16 min), which were aggregated, generating an increase of 1.1 μm in the width and a decrease of 2.6 μm in the length of the CaVO-16 sample (FIGURE 4.4(c)). It can be observed that, for a synthesis time of 16 min, there was a significant reduction of isolated rods in the sample. Further increasing the synthesis time to 32 min provoked the dissolution and recrystallization processes, with a concomitant elongation of the rods (FIGURE 4.4(d)). These rods were split into nanofilaments during the growth process, forming a particle with more ramifications. The CaVO-32 crystal presented tubes with the length of 6.67 μm and smaller width (230 nm) than the crystals obtained within a shorter synthesis time.

The growth process of the $Ca_{10}V_6O_{25}$ particles can be considered to be a crystal splitting mechanism. The nanocrystals are developed in large crystals, and these are divided to form stems, which are subdivided into nanofilaments as a bundle of straw shape. The division of the crystal is related to the rapid kinetics of crystal growth, supersaturation of the solution, and surface energy [161-164]. FIGURE 4.5 shows a series of morphologies formed according to the growth time of the $Ca_{10}V_6O_{25}$ particles. Thus, we observe that a single crystal is subdivided by means of a single nucleus. Along with the growth of the particle, there is a change in the [CaO_6] clusters, and thus, different morphologies that are dependent on the synthesis time and the presence of microwaves are observed.

It can be observed that the MAH method allowed us to obtain materials with good structural ordering at short time and low temperature (120 °C at 4 min) with well-defined morphology. The interaction of the microwave energy with the particles or ions accelerates the diffusion mechanism, allowing the collision with other ions, atoms, or neighboring molecules, generating heat and thus reducing sintering time and temperature [139]. These shocks are fast and effective, which cause small distortions in bond length and angles in the [CaO_6] and [VO_4] clusters of the crystal lattice. Thus, with the increase of the synthesis time, the microwaves cause a restructurization of the clusters forming order and disorder locally, which can be seen the medium-range by the modification in the orientations of the clusters. These distortions in clusters generate defects as quantum dots, which favor the different PL properties of the material.

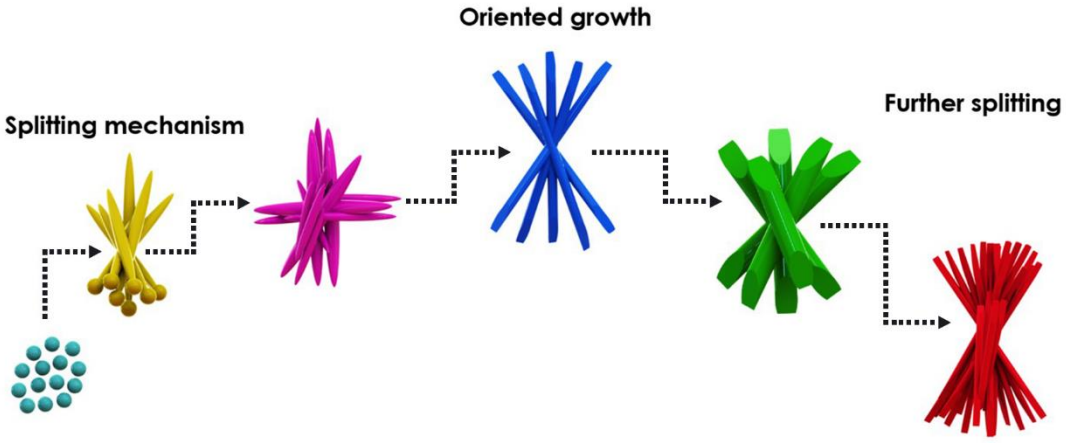

FIGURE 4.5 - Growth mechanism of the $Ca_{10}V_6O_{25}$ crystal as function of synthesis time: 4 min (pink), 8 min (blue), 16 min (green), and 32 min (red).

4.5. Optical properties

4.5.1. UV-vis diffused reflectance

The optical properties of the $Ca_{10}V_6O_{25}$ semiconductors prepared at different times (4, 8, 16, and 32 min) at 120 °C via the MAH method were investigated using UV–vis and PL emissions at room temperature. $Ca_{10}V_6O_{25}$ has a direct-type optical transition [16]. According to the Wood-Tauc function [115], $\alpha hv = C_1(hv - E_{gap})^n$, where $n = ½$, α is the absorption coefficient, hv is the photon energy, C_1 is a proportionality constant, and n is the type of electronic transition. Thus, we have $(\alpha hv)^2$, which can be related to the Kubelka–Munk function (K–M) [114], and we obtain the band gap energy (E_{gap}) values of the samples using the graph $[F(R)hv]^2$ vs hv (FIGURE B3 in the Supplementary Information), where $F(R)$ is the K–M function.

UV–vis spectra show that all the samples of $Ca_{10}V_6O_{25}$ absorbed energy in the ultraviolet. An analysis of the results renders that the samples present an E_{gap} values at 4.04, 4.04, 3.94, and 3.84 eV at CaVO-4, CaVO-8, CaVO-16, and CaVO-32, respectively (see FIGURE B3). According to the Wood–Tauc function, a crystalline and ordered material has a well-defined absorption (vertical black dashed curve), and, therefore, for the $Ca_{10}V_6O_{25}$ crystal, a band gap (E_{gap}) of 4.3 eV is expected. Moreover, it can be observed that the variation in the synthesis time did not change the E_{gap} values of the $Ca_{10}V_6O_{25}$ samples. However, a slope of the optical absorption curves can be observed, indicating the presence of medium-range defects, which decreased the E_{gap} of the samples. The medium-range distortion on the $[CaO_6]_d$ and $[VO_4]_d$ clusters leads to a nonzero difference in the formal load between the clusters, thus causing a polarization in the system. The medium-range polarization generates an orientation interaction, since it causes the rotation motion of the permanent moments in different $[CaO_6]$–$[CaO_6]$, $[VO_4]$–$[VO_4]$, or $[CaO_6]$–$[VO_4]$ clusters.

These interactions produce localized electronic levels within the forbidden band gap, which cause the entrapment of electrons and holes. Thus, the intrinsic PL emissions can be associated with these mechanisms, which are derived from the interactions between distorted clusters. In this way, the coupling of the vibrational and rotational movements modifying the intrinsic properties generating new materials. These properties are related to the defect densities, that is, order–disorder of the crystals.

To clarify the electronic structure of $Ca_{10}V_6O_{25}$, total and atom-resolved density of states (DOS) and band structures profiles were obtained, and the corresponding results are presented in FIGURE 4.6. In the left panel (FIGURE 4.6a), the band structure profile for $Ca_{10}V_6O_{25}$ is presented, in the middle panel (FIGURE 4.6b), total and atom-resolved DOS curves are presented, whereas in the right panel (FIGURE 4.6c), a cluster-resolved DOS curve is depicted focusing on the contribution of different [CaO_6] clusters with singular symmetries. An analysis of the both valence and conduction bands (VB and CB, respectively) show a pattern, which is directly associated with the local clusters centered on Ca and V cations. The VB was predominantly composed of the orbitals of oxygen anions with a small content of Ca orbitals. In contrast, the CB was mostly based on empty valence orbitals from V cations hybridized with oxygen atomic orbitals, revealing the role of [VO_4] clusters.

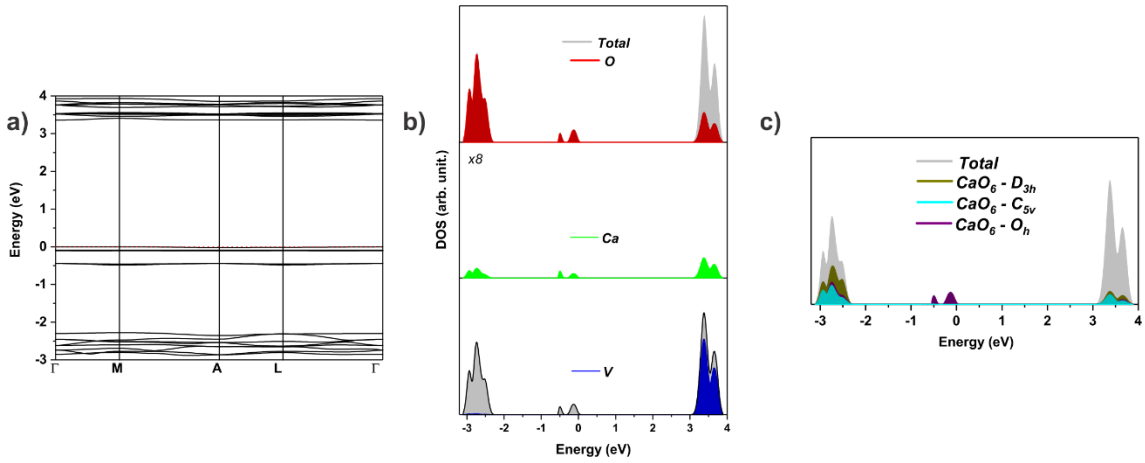

FIGURE 4.6 - (a) Band structure, (b) total and atom-resolved DOS, and (c) Ca-centered cluster resolved DOS for $Ca_{10}V_6O_{25}$ material. In both cases, the Fermi level was set to zero.

Let us now briefly discuss the relationship between the local coordination of both V and Ca cations and the electronic structure of the $Ca_{10}V_6O_{25}$ crystal. The optimized crystalline structure obtained for $Ca_{10}V_6O_{25}$ indicates that Ca cations have a 6-fold coordination [CaO_6] with distinct local environments, as presented in FIGURE 4.2. Despite the same coordination number, the local arrangement indicates the formation of distorted octahedral, prism, and pentagonal-pyramidal symmetries. These distorted polyhedral symmetries provoke a local disorder along the crystalline structure, which perturbs the energy level distribution in the VB. From the energy levels distribution depicted in FIGURE 4.6c, it can be observed that the VB region exhibits two intermediate levels of energy, which can be directly related to the local geometries associated with Ca-centered clusters. Indeed, the first contribution located between –3.15 eV and –2.28 eV is related to the presence of all Ca-centered clusters with a major contribution of approximately prismatic [CaO_6] clusters. In addition, it was noted that, at the vicinity of the Fermi level (between –0.46 eV and 0.0 eV), the electronic states are related to the distorted Ca-centered octahedral clusters. Therefore, the distortion associated with the

crystalline structure of the $Ca_{10}V_6O_{25}$ results in a singular energy-level distribution that controls its electronic properties.

In addition, the obtained band structure profiles indicate that both VB maxima and CB minimum regions present flat energy bands against the symmetry points, resulting in a small difference between the direct and indirect band gap values, which helps achieve superior electrical and optical properties. The calculated band gap is 3.35 eV; in contrast, the experimental value reported here is 4.04 eV. This difference can be associated with almost two factors, as follows: (i) the as-synthesized $Ca_{10}V_6O_{25}$ materials exhibits a high degree of structural disorders with the presence of intermediary energy levels at the forbidden region, and (ii) the theoretical values are computed by using the hybrid B3LYP functional and their drawbacks to obtain accurate values of the band gap are well-known [165, 166].

Hojamberdiev and co-workers [16] successfully used hydrothermal methods to grow $Ca_{10}V_6O_{25}$ crystals, which showed a semiconducting behavior with band gap values of ~3.7 eV, which is consistent with our theoretical and experimental data. In this case, it can be assumed that the electron transfer associated with the band gap value involves the excitation of VBM electrons, which are located at the orbitals linked to the Ca–O bonds of the highly distorted octahedral [CaO_6] clusters, to orbitals or empty states located at the V–O bond of the [VO_4] clusters.

4.5.2. PL emissions

FIGURE 4.7 shows the PL spectra at room temperature, with the wavelength of excitation of 350 nm. All the samples had a broadband profile covering the entire visible region of light. The PL spectra were deconvoluted to understand the behavior of the PL property of the $Ca_{10}V_6O_{25}$ samples. The Voigt

Area G/L function was used, and three components were centered in the yellow (2.12 eV, 585 nm), green (2.43 eV, 510 nm) and blue (2.79 eV, 444 nm) regions.

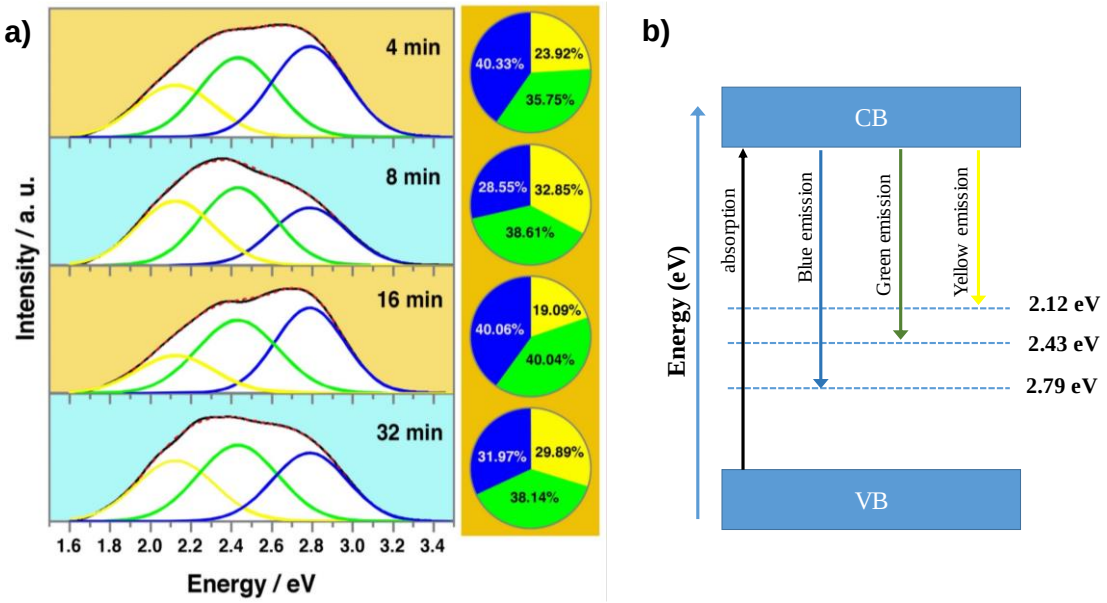

FIGURE 4.7 – (a) Photoluminescence spectra at room temperature (black line), deconvolution (red dashed), and percentage of color area, blue (444 nm, 2.79 eV), green (510 nm, 2.43 eV), and yellow (585 nm, 2.12 eV), of the $Ca_{10}V_6O_{25}$ processed at 120 °C as function of synthesis time. (b) Schematic representation of the PL emissions associated with the presence of the intermediated levels between the conduction band (CB) and the valence band (VB).

It can be observed that the CaVO-4 and CaVO-16 samples have a higher percentage of emission in the blue and green regions, whereas, for the CaVO-8 and CaVO-32 samples, a higher percentage of emission in the yellow region is observed, which are related to the presence of the intrinsic structural defects of the samples. These defects generate intermediated levels between VB and CB. Therefore, the fast growth process and formation of smaller stems causes a high concentration of defects associated to structural distortions in the $[VO_4]$ clusters. An analysis of the deconvolution of PL emissions displayed in FIGURE 4.7a renders that emission energy in the yellow region corresponds to 2.12 eV,

being lower than the energies in the blue region (2.79 eV, and green, 2.43 eV, regions (see FIGURE 4.7b)).

Both dissolution and recrystallization processes during the synthesis favor the formation of elongated stems in these samples, generating oxygen vacancies and surface defects. Three different charge states of oxygen vacancies may occur: the [$VO_3.V_0^x$] state, which presents two paired electrons and is neutral in relation to the lattice; the singly ionized [$VO_3.V_0^{\cdot}$] state, which has one unpaired electron; the [$VO_3.V_0^{\cdot\cdot}$] state, which is doubly positively charged, with respect to the lattice. It is believed that these different types of structural defects that are generated by medium-range distortion that give rise to PL at room temperature. Since, the distortion causes the polarization in the structure and enable the formation of localized states in the band gap, as well as the inhomogeneous charge distribution in the cell, allowing the entrapment of electrons. The distribution of the localized levels allows various energies to be able to excite the trapped electrons. Broadband PL emission for all $Ca_{10}V_6O_{25}$ samples (FIGURE 4.7) shows the participation of numerous energy levels within the band gap, where the shift observed in the maximum emission point is due to variations on the density of structural defects.

A PL mechanism for disordered solids has been very reported in the literature and first-principles calculations are very important to elucidate such a mechanism [158, 167, 168]. In such mechanism structural defects, the creation of oxygen vacancies from the disorder of clusters, as the building block of the material is responsible for the formation of excited singlet (s*) and triplet (t*) electronic states related to PL phenomena. In particular, for our $Ca_{10}V_6O_{25}$ samples synthesized at various times, the experimental results show a similar response; thus, structural defects are important to investigate this material. Oxygen vacancies are the strongest evidence of the structural and electronic disorder in [CaO_6] clusters; high concentration of disorder in clusters results in

excited electronic states. Therefore, we proceed to the localization and characterization of the excited electronic states of the $Ca_{10}V_6O_{25}$ system.

4.5.2.1 Excited states

FIGURE B4, see Appendix B in the Supplementary Information, shows the 3D optimized structure of the excited states, singlet (s*) and triplet (t*), and the local structures of the constituent clusters, which are compared with the fundamental structure of the fundamental singlet electronic state (see FIGURE 4.2). First, we note that the obtained geometries for s* and t* exhibit imaginary frequencies (see TABLE B3 in the Supplementary Information). The singlet excited electronic state, s*, as the ground state (TABLE B2) corresponds to a saddle point (–79.33 cm^{-1}) on a very flat potential energy surface, whereas the excited triplet electronic state, t*, exhibits a very high and negative imaginary frequency (–1966.99 cm^{-1}), showing large structural instability. All attempts to adjust the geometries and eliminate these negative values was unsuccessful.

An analysis of FIGURE B4 shows that three different local arrangements with singular symmetries (D_{3h}, C_{5v}, and O_h) were observed for both s* and t*. The DOS and band structure profiles obtained for the fundamental and excited states are depicted in FIGURE B5 in the Supplementary Information. Regarding the calculated band gap value for s*, a similar value (3.29 eV) to the electronic ground-state was observed, as the VB is mainly composed of O (2p) states and the CB is predominantly formed by the V (3d) atomic state (FIGURE B5a in the Supplementary Information). The main differences were attributed to the band degeneration in the s* state (FIGURE B5a), which can be attributed to the displacement of V atoms in the [VO_4] cluster. In addition, the calculated band structure for the t* state (FIGURE B5b) indicates a band gap value of 1.35 eV, which is a reduced value, in comparison with the singlet ground state. This electron transfer mechanism was described as a charge transfer from the 2p

orbitals of disordered octahedral [CaO_6] clusters to the 3d orbitals of [VO_4] clusters (FIGURE. B5b), indicating that the unpaired electron density generated in the t* state is located in the 3d empty orbitals of V atoms. The electron transfer from VB to CB perturbs the electron density distribution along the [CaO_6] clusters, reordering the charge in the crystalline structure once the uppermost contributions of VB related to the presence of distorted octahedral clusters become high in energy, relative to the molecular orbitals of prismatic and pyramidal clusters.

Therefore, this wideband model enables the observation of the electronic features associated with the transformation from a fundamental s state to excited s* and t* states. In the CB, the t* state induces the creation of intermediary energy levels near the band gap region responsible for the trapping of excited electrons. The calculated results confirm the electron transfer mechanism predicted from the DOS and band structure profiles (FIGURE 4.6). Notably, the unpaired density is mainly located on the [VO_4] clusters closer to the highly distorted [CaO_6] octahedra. The high distortion of [CaO_6] clusters causes an increase in VBM, featuring the electronic excitation process as a charge transfer from [CaO_6] clusters to [VO_4] clusters. Therefore, the PL process is understood in the first moment as an excitation from the fundamental state (s) to an excited energy state (t*), which possesses a relative energy of 3.41 eV, in comparison with the ground state. The subsequent step can be described as an intersystem crossing process from the excited t* state to an s* electronic state, which exhibits a lower relative energy (1.03 eV), compared with the fundamental state. Once this excited s* electronic state is sufficiently populated, the PL emission occurs with a concomitant return to a ground electronic state.

The transformations from fundamental s (FIGURE 4.2) to both excited s* and t* electronic states (FIGURE B4), at prismatic (D_{3h}) and pyramidal (C_{5v}) clusters, are accompanied by a local disorder for both short and long Ca–O bonds, showing a general shortening of the chemical bonds. In contrast, the

octahedral (O_h: centered in Ca5–7) cluster shows a bond expansion from the fundamental s state to the excited s* state, whereas the transformation from s* to t* is accompanied by a bond contraction. Regarding the structural disorders associated with the tetrahedral [VO_4] cluster, it was observed that the transformation from s to s* involves the off-center displacement of V atoms in the *z*-direction, resulting in an in-plane bond elongation and out-of-plane bond contraction. This local disorder also affects the other V atoms in the crystalline structure exhibiting distorted V–O bonds. Furthermore, the transformation from s* to t* suggests a higher local disorder for [VO_4] clusters, where the V–O bond length increases.

A careful inspection of the obtained values indicates that the transformation from the fundamental s state to the excited s* and t* states is predominantly attributed to the symmetrical stretching vibration of the V–O bond associated with the mode described by four degenerated frequencies: 859.60 cm^{-1} in the fundamental state and 854.88 cm^{-1} in the s* state, which becomes nondegenerated for the t* state, which exhibits frequencies of 531.25 and 830.70 cm^{-1}, consistent with the structural disorders summarized in FIGURE B4. This suggests a transition to a lower symmetry without bond breaking, which involves the structural order–disorder effect originating from the off-centering V displacement, modifying not only the V–O bond lengths, but also the interaction among the electronic distributions of the atoms of the cell.

4.6. Measurements of current versus voltage

FIGURE 4.8 shows the current–voltage (*I–V*) characterization of the $Ca_{10}V_6O_{25}$ samples. The curves showed that the electric current in the samples presented a linear dependence with the voltage, showing an ohmic character at room temperature. It can be observed that the CaVO-4 and CaVO-32 samples showed lower electrical conductivity, compared with the CaVO-8 sample. This is

possibly due to the trapping of electrons, which would be free to conduct; one reason for this behavior is the presence of oxygen molecules adsorbed on the surface or to the electron–hole recombination process. The CaVO-8 sample exhibited a greater conductivity than the other samples, and thus, it has a greater availability of free electrons. The CaVO-8 sample has numerous vanadium–oxygen vacancy centers, because of a higher percentage of emission in yellow and red regions (see FIGURE 4.7). Oxygen vacancies form positive charges in the $Ca_{10}V_6O_{25}$ crystal lattice, favoring the diffusion of electrons when an external voltage is applied. Thus, a large current was observed in the CaVO-8 sample. However, for the CaVO-16 sample, a very high resistance was observed and the conductivity was not measured (FIGURE B6 in the Supporting Information). From the PL spectrum, it was observed that this sample has a higher emission in the blue and green regions, which are directly related to the intrinsic structural defects. These defects trap electrons, increasing the resistivity of the material. Moreover, in this sample, the interconversion of octahedral clusters to prismatic and pyramidal clusters of calcium may have occurred. These prismatic and pyramidal clusters show a tendency to form materials with a resistivity character. In addition, the morphology of the CaVO-16 sample may have favored these more-resistive calcium clusters.

From the theoretical point of view, the electrical properties of the $Ca_{10}V_6O_{25}$ crystal can be understood using the symmetry-adapted molecular orbitals depicted in FIGURE 4.6, where the VB is described by two different oxygen contributions, because of to the existence of several $[CaO_6]$ clusters. Therefore, the existence of conductive behavior of the samples can be attributed to the presence of highly distorted octahedral clusters contributing to the upper part of VB, whereas the resistive response is related to the pyramidal and prismatic clusters that contribute to the inner VB region.

However, all the samples exhibited low conduction, which is a characteristic of semiconductor materials. It can be observed that the synthesis

time influenced the ordering of the material and the transport properties of electrons.

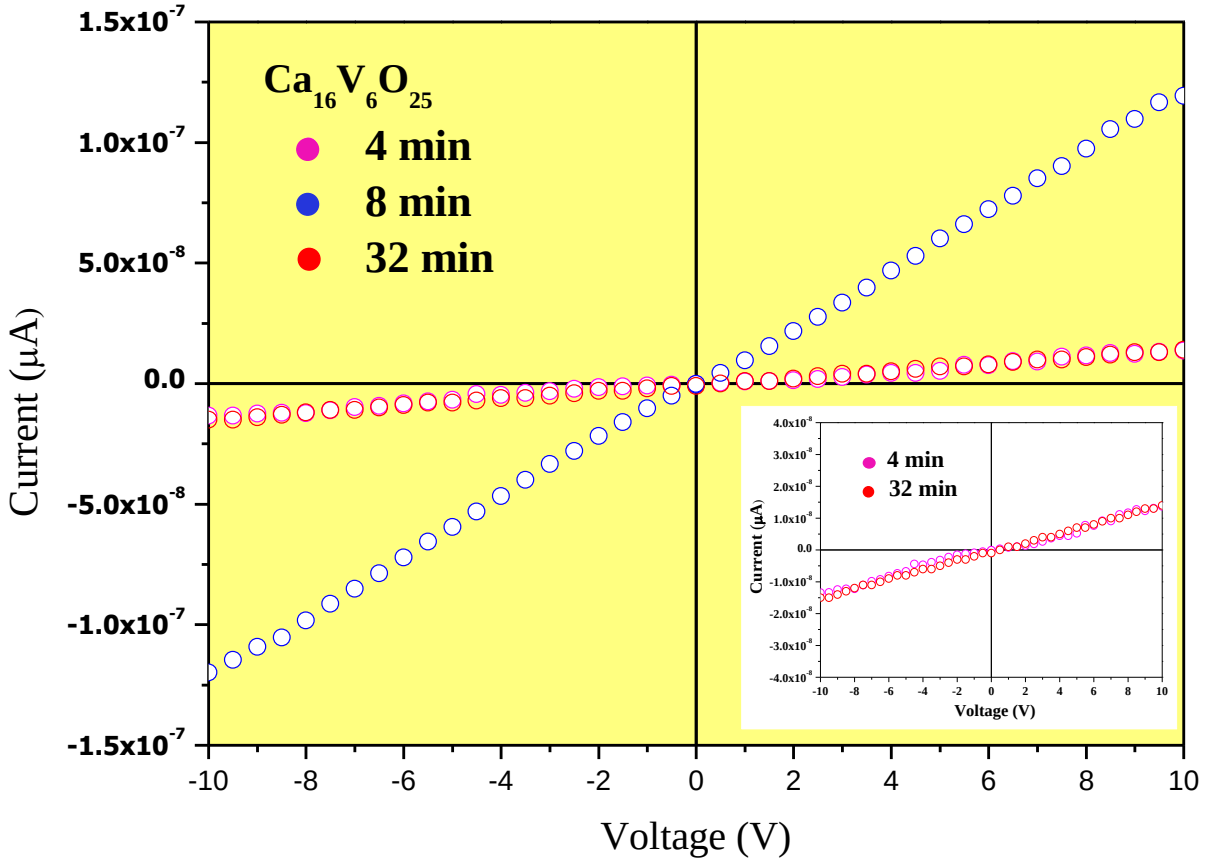

FIGURE 4.8 - Current–voltage for the $Ca_{10}V_6O_{25}$ samples (with time 4, 8, and 32 min in 120 °C by MAH) at room temperature.

4.7. Conclusion

A facile, fast, and environmentally friendly method was reported for the synthesis of $Ca_{10}V_6O_{25}$ crystals. This new structure was prepared via the MAH method, which favors the growth of crystals with different morphologies through time variation. The XRD and Raman patterns showed a complex structure with *P6₃/m* space group symmetry, formed by distorted [VO_4] with various distorted [CaO_6] clusters. Well-faceted and highly crystalline microcrystals were observed, consistent with the XRD and theoretical and experimental Raman spectroscopic analysis. The degree of short organization of the Ca clusters is a determinant of PL emissions. The charge transfer process between [VO_4] and [CaO_6] clusters is responsible for the presence of the singlet and triplet excited electronic states. In addition, the strong influence of defects (intrinsic structural defects and oxygen vacancy) on the electron diffusion in the samples can be observed. The sample that exhibited a greater percentage of oxygen vacancies favored the electron transport. Furthermore, depending on the synthesis conditions used for obtaining these crystals, different morphologies and distortions in their lattice, mainly associated with the distortions of the [VO_4] and [CaO_6] clusters, can be observed, and thus, they can exhibit different electronic properties. These results summarize the relevant contributions to the understanding of the structural, electronic, and optical properties of $Ca_{10}V_6O_{25}$ crystals and the growth mechanism involved during the MAH processing.

5. General Conclusions

5. GENERAL CONCLUSIONS

The calcium vanadate structures with formula $Ca_{10}V_6O_{25}$ were efficiently synthesized using the CP and MAH methods. Different degrees of structural order/disorder in the long- and short-range were observed unsing XRD and Raman spectroscopy measurements. Besides that, the $Ca_{10}V_6O_{25}$ phase was confirmed with the spatial group $P6_3/m$ being formed by distorted [VO_4] and [CaO_6] clusters. XANES spectroscopy confirmed that the $Ca_{10}V_6O_{25}$ structure is composed of vanadium atoms with 5+ oxidation state with tetragonal configuration. The micrographs showed that the variation in the synthesis conditions (temperature and time) were efficient to change the morphology and the microstructural order. The data from UV-vis DRS demonstrate that the $Ca_{10}V_6O_{25}$ compounds present a structural order/disorder in intermediate range, which were formed by local distortions in the [CaO_6] and [VO_4] clusters. Also, combined with theoretical calculations, it was observed that VB is composed predominantly of oxygen atoms with a small contribution from calcium atoms, and CB is composed of vanadium atoms hybridized with oxygen atoms. The photoluminescent behavior of the $Ca_{10}V_6O_{25}$ compounds was attributed to structural factor due to the order/disorder present in the [VO_4] and [CaO_6] clusters, as well as the variation of the morphology and the superficial defects present in the samples. In particular, the theoretical results indicate that the effect of structural order/disorder generates electronic levels located above the VB and below the CB. In this sense, photoluminescence has a strong contribution of defect levels formed within the band gap, as well as on the surface of the samples.

6. REFERENCES

1. THOMAS, G. M.; DAMZEN, M. J. "Passively Q-switched Nd:YVO_4 laser with greater than 11W average power". Optics Express, 19 (5): 4577, 2011.

2. CHELLAPPAN, K. V.; ERDEN, E.; UREY, H. "Laser-based displays: a review". Applied Optics, 49 (25): F79, 2010.

3. ZHUANG, X.; OUYANG, Y.; WANG, X.; PAN, A. "Multicolor semiconductor lasers". Advanced Optical Materials, 7 (17): 1900071, 2019.

4. NAKAJIMA, T.; ISOBE, M.; UZAWA, Y.; TSUCHIYA, T. "Rare earth-free high color rendering white light-emitting diodes using $CsVO_3$ with highest quantum efficiency for vanadate phosphors". Journal of Materials Chemistry C, 3 (41): 10748, 2015.

5. BLASSE, G. "Luminescence of inorganic solids - from isolated centers to concentrated systems". Progress in Solid State Chemistry, 18 (2): 79, 1988.

6. SU, L.; FAN, X.; YIN, T.; WANG, H.; LI, Y.; LIU, F.; LI, J.; ZHANG, H.; XIE, H. "Inorganic 2D luminescent materials: structure, luminescence modulation, and applications". Advanced Optical Materials, 8 (1): 1900978, 2019.

7. FENGWEN KANG; HAISHAN ZHANG; LOTHAR WONDRACZEK; XIAOBAO YANG; YI ZHANG; DANG YUAN LEI; PENG, M. "Band-gap modulation in single Bi^{3+}-doped yttrium−scandium−niobium vanadates for color tuning over the whole visible spectrum". Chemistry of Materials, 28 (8): 2692, 2016.

8. HAMEED, A.; MONTINI, T.; GOMBAC, V.; FORNASIERO, P. "Surface phases and photocatalytic activity correlation of Bi_2O_3/Bi_2O_{4-x} nanocomposite". Journal American Chemical Society, **130**: 9658, 2008.

9. SUN, C.; SONG, S.; XUE, D.; ZHANG, H. "Crystallization of oxides as functional materials". Functional Materials Letters, 05 (02): 1230002, 2012.

10. NAKAJIMA, T.; ISOBE, M.; TSUCHIYA, T.; UEDA, Y.; MANABE, T. "Photoluminescence property of vanadates $M_2V_2O_7$ (M: Ba, Sr and Ca)". Optical Materials, 32 (12): 1618, 2010.

11. NAKAJIMA, T.; ISOBE, M.; TSUCHIYA, T.; UEDA, Y.; MANABE, T. "Correlation between luminescence quantum efficiency and structural properties of vanadate phosphors with chained, dimerized, and isolated VO_4 tetrahedra". Journal of Physical Chemistry C, 114 (11): 5160, 2010.

12. TONG, Y.-P.; LUO, G.-T.; JIN, Z.; LIN, Y.-W. "Synthesis, structure, and theoretical investigations of an alkaline earth vanadate oxide compound ($Ca_4V_4O_{14}$): electronic, optical, and chemical bond properties". Australian Journal of Chemistry, 64 (7): 973, 2011.

13. PEI, L. Z.; PEI, Y. Q.; XIE, Y. K.; YUAN, C. Z.; LI, D. K.; ZHANG, Q.-F. "Growth of calcium vanadate nanorods". Crystengcomm, 14 (13): 4262, 2012.

14. PARHI, P.; UPRETI, S.; RAMANAN, A. "Crystallization of calcium vanadate solids from solution: a metathetic route". Crystal Growth & Design, 10 (12): 5078, 2010.

15. YU, R.; XUE, N.; HUO, S.; LI, J.; WANG, J. "Structure characteristics and photoactivity of simultaneous luminescence and photocatalysis in CaV_2O_6 nanorods synthesized by the sol–gel Pechini method". RSC Advances, 5 (78): 63502, 2015.

16. HOJAMBERDIEV, M.; BOZGEYIK, M. S.; ABDULLAH, A. M.; BEKHEET, M. F.; ZHU, G.; YAN, Y.; XU, Y.; OKADA, K. "Hydrothermal-induced growth of $Ca_{10}V_6O_{25}$ crystals with various morphologies in a strong basic medium at different temperatures". Materials Research Bulletin, 48 (4): 1388, 2013.

17. SINGH, V.; SESHADRI, M.; PATHAK, M. S.; SINGH, N. "Sm^{3+} doped calcium orthovanadate $Ca_3(VO_4)_2$ - A spectral study". Spectrochim Acta A Mol Biomol Spectrosc, **217**: 315, 2019.

18. MATSUSHIMA, Y.; KOIDE, T.; HIRO-OKA, M.; SHIDA, M.; SATO, A.; SUGIYAMA, S.; ITO, M.; MCKITTRICK, J. "Self-activated vanadate compounds toward realization of rare-earth-free full-color phosphors". Journal of the American Ceramic Society, 98 (4): 1236, 2015.

19. ZHAO, B.; YUAN, L.; HU, S.; ZHANG, X.; ZHOU, X.; TANGC, J.; YANG, J. "Controllable synthesis of $Sc_2Mo_3O_{12}$ microcrystals with exposed {001} facets and their remarkable tunable luminescence properties by doping lanthanides". Crystengcomm, 18 (41): 8044, 2016.

20. XUE, D.; LI, K.; LIU, J.; SUN, C.; CHEN, K. "Crystallization and functionality of inorganic materials". Materials Research Bulletin, 47 (10): 2838, 2012.

21. MANN, S. "Synthesis of barium sulfate from surfactant – inorganic nanoparticles". Angewandte Chemie International Edition, **39**: 3392 2000.

22. XIONG, S.; XI, B.; WANG, C.; XU, D.; FENG, X.; ZHU, Z.; QIAN, Y. "Tunable synthesis of various wurtzite ZnS architectural structures and their photocatalytic properties". Advanced Functional Materials, 17 (15): 2728, 2007.

23. GURGEL, A. L.; MARTINELLI, A. E.; CONCEIÇÃO, O. L. D. A.; XAVIER, M. M.; MORALES TORRES, M. A.; DE ARAÚJO MELO, D. M. "Microwave-assisted hydrothermal synthesis and magnetic properties of nanostructured cobalt ferrite". Journal of Alloys and Compounds, **799**: 36, 2019.

24. GAO, Y.; NIE, W.; WANGA, X.; FAN, F.; LIA, C. "Advanced space- and time-resolved techniques for photocatalyst studies". Chem Commun (Camb), 56 (7): 1007, 2020.

25. HUANG, M. H.; NARESH, G.; CHEN, H. S. "Facet-dependent electrical, photocatalytic, and optical properties of semiconductor crystals and their implications for applications". ACS Appl Mater Interfaces, 10 (1): 4, 2018.

26. HUANG, M. H. "Facet-dependent optical properties of semiconductor nanocrystals". Small, 15 (7): e1804726, 2019.

27. ZHANG, X.; BOURGEOIS, L.; YAO, J.; WANG, H.; WEBLEY, P. A. "Tuning the morphology of bismuth ferrite nano- and microcrystals: from sheets to fibers". Small, 3 (9): 1523, 2007.

28. POLSHETTIWAR, V.; BARUWATI, B.; VARMA, R. S. "Self-assembly of metal oxides into three-dimensional nanostructures: synthesis and application in catalysis". ACS NANO, 3 (3): 728, 2009.

29. ANTONIETTI, M.; OZIN, G. A. "Promises and problems of mesoscale materials chemistry or why meso?". Chemistry, 10 (1): 28, 2004.

30. SUN, S.; YUAN, D.; XU, Y.; WANG, A.; DENG, Z. "Ligand-mediated synthesis of shape-controlled cesium lead halide perovskite nanocrystals via reprecipitation process at room temperature". ACS NANO, 10 (3): 3648, 2016.

31. ZHU, F.; MEN, L.; GUO, Y.; ZHU, Q.; BHATTACHARJEE, U.; GOODWIN, P. M.; PETRICH, J. W.; SMITH, E. A.; VELA, J. "Shape evolution and single particle luminescence of organometal halide perovskite nanocrystals". ACS NANO, 9 (3): 2948, 2015.

32. SYRENOVA, S.; WADELL, C.; NUGROHO, F. A.; GSCHNEIDTNER, T. A.; DIAZ FERNANDEZ, Y. A.; NALIN, G.; SWITLIK, D.; WESTERLUND, F.; ANTOSIEWICZ, T. J.; ZHDANOV, V. P.; MOTH-POULSEN, K.; LANGHAMMER, C. "Hydride formation thermodynamics and hysteresis in

individual Pd nanocrystals with different size and shape". Nat Mater, 14 (12): 1236, 2015.

33. ROCA, R. A.; SCZANCOSKI, J. C.; NOGUEIRA, I. C.; FABBRO, M. T.; ALVES, H. C.; GRACIA, L.; SANTOS, L. P. S.; DE SOUSA, C. P.; ANDRÉS, J.; LUZ, G. E.; LONGO, E.; CAVALCANTE, L. S. "Facet-dependent photocatalytic and antibacterial properties of α-Ag_2WO_4 crystals: combining experimental data and theoretical insights". Catalysis Science & Technology, 5 (8): 4091, 2015.

34. DE OLIVEIRA, R. C.; DE FOGGI, C. C.; TEIXEIRA, M. M.; DA SILVA, M. D.; ASSIS, M.; FRANCISCO, E. M.; PIMENTEL, B. N.; PEREIRA, P. F.; VERGANI, C. E.; MACHADO, A. L.; ANDRES, J.; GRACIA, L.; LONGO, E. "Mechanism of antibacterial activity via morphology change of α-$AgVO_3$: Theoretical and experimental insights". ACS Appl Mater Interfaces, 9 (13): 11472, 2017.

35. FERMANI, S.; NJEGIĆ DŽAKULA, B.; REGGI, M.; FALINI, G.; KRALJ, D. "Effects of magnesium and temperature control on aragonite crystal aggregation and morphology". Crystengcomm, 19 (18): 2451, 2017.

36. XIAO, X.; LIU, X.; ZHAO, H.; CHEN, D.; LIU, F.; XIANG, J.; HU, Z.; LI, Y. "Facile shape control of Co_3O_4 and the effect of the crystal plane on electrochemical performance". Adv Mater, 24 (42): 5762, 2012.

37. ZHAN, Y.; SHEN, L.; XU, C.; ZHAO, W.; CAO, Y.; JIANG, L. "MOF-derived porous Fe_2O_3 with controllable shapes and improved catalytic activities in H_2S selective oxidation". Crystengcomm, 20 (25): 3449, 2018.

38. ZHONG, Y.; WANG, Z.; ZHANG, R.; BAI, F.; WU, H.; HADDAD, R.; FAN, H. "Interfacial self-assembly driven formation of hierarchically structured nanocrystals with photocatalytic activity". ACS NANO, 8 (1): 827, 2014.

39. CHEN, K.; XUE, D. "Nanoparticles via crystallization: a chemical reaction control study of copper oxides". Nanoscience and Nanotechnology Letters, 4 (1): 1, 2012.

40. CAO, S.; TAO, F. F.; TANG, Y.; LI, Y.; YU, J. "Size- and shape-dependent catalytic performances of oxidation and reduction reactions on nanocatalysts". Chem Soc Rev, 45 (17): 4747, 2016.

41. ZAERA, F. "Shape-controlled nanostructures in heterogeneous catalysis". ChemSusChem, 6 (10): 1797, 2013.

42. XIA, Y.; XIONG, Y.; LIM, B.; SKRABALAK, S. E. "Shape-controlled synthesis of metal nanocrystals: simple chemistry meets complex physics?". Angew Chem Int Ed Engl, 48 (1): 60, 2009.

43. NADAGOUDA, M. N.; SPETH, T. F.; VARMA, R. S. "Microwave-assisted green synthesis of silver nanostructures". Acc Chem Res, 44 (7): 469, 2011.

44. CHO, S.; JUNG, S.-H.; LEE, K.-H. "Morphology-controlled growth of ZnO nanostructures using microwave irradiation: from basic to complex structures". Journal of Physical Chemistry C, 112 (33): 12769, 2008.

45. SILVA, L. F. D.; CATTO, A. C.; JR, W. A.; MESQUITA, A.; MAIA, L. J. Q.; LOPES, O. F.; LI, M. S.; MOREIRA, M. L.; LONGO, E.; ANDRÉS, J.; R., V.; MASTELARO. "Unveiling the efficiency of microwave-assisted hydrothermal treatment for the preparation of $SrTiO_3$ mesocrystals". Physical Chemistry Chemical Physics, 21 (39): 22031, 2019.

46. KOMARNENI, S.; ROY, R.; LI, Q. H. "Microwave-hydrothermal synthesis of ceramic powders". Materials Research Bulletin, 27 (12): 1393, 1992.

47. ZHU, Y. J.; CHEN, F. "Microwave-assisted preparation of inorganic nanostructures in liquid phase". Chem Rev, 114 (12): 6462, 2014.

48. MOREIRA, M. L.; LONGO, V. M.; AVANSI, W.; FERRER, M. M.; ANDRÉS, J.; MASTELARO, V. R.; VARELA, J. A.; LONGO, É. "Quantum mechanics insight into the microwave nucleation of $SrTiO_3$ nanospheres". The Journal of Physical Chemistry C, 116 (46): 24792, 2012.

49. DE LA HOZ, A.; DIAZ-ORTIZ, A.; MORENO, A. "Microwaves in organic synthesis. Thermal and non-thermal microwave effects". Chem Soc Rev, 34 (2): 164, 2005.

50. ZHOU, N.; SHA, S.; ZHANG, Y.; LI, S.; XU, S.; LUAN, J. "Coprecipitation synthesis of a green Co-doped wurtzite structure high near-infrared reflective pigments using ammonia as precipitant". Journal of Alloys and Compounds, **820**: 153183, 2020.

51. RANGEL, W. M.; BOCA SANTA, R. A. A.; RIELLA, H. G. "A facile method for synthesis of nanostructured copper (II) oxide by coprecipitation". Journal of Materials Research and Technology, 9 (1): 994, 2020.

52. LONGO, V. M.; CAVALCANTE, L. S.; PARIS, E. C.; SCZANCOSKI, J. C.; PIZANI, P. S.; LI, M. S.; ANDRÉS, J.; LONGO, E.; VARELA, J. A. "Hierarchical assembly of $CaMoO_4$ nano-octahedrons and their

photoluminescence properties". The Journal of Physical Chemistry C, 115 (13): 5207, 2011.

53. YANG, P. "SURFACE CHEMISTRY Crystal cuts on the nanoscale". Nature, 482 (7383): 41, 2012.

54. OLIVEIRA, R. C.; TEIXEIRA, M. M.; COSTA, J. P. C.; PENHA, M.; FRANCISCO, E. M.; DA SILVA, J. S.; LI, M. S.; LONGO, E.; GRACIA, L.; ANDRÉS, J. "α- and β-$AgVO_3$ polymorphs as photoluminescent materials: An example of temperature-driven synthesis". Ceramics International, 44 (6): 5939, 2018.

55. PEREIRA, P. F. S.; GOUVEIA, A. F.; ASSIS, M.; DE OLIVEIRA, R. C.; PINATTI, I. M.; PENHA, M.; GONCALVES, R. F.; GRACIA, L.; ANDRES, J.; LONGO, E. "$ZnWO_4$ nanocrystals: synthesis, morphology, photoluminescence and photocatalytic properties". Phys Chem Chem Phys, 20 (3): 1923, 2018.

56. MACHADO, T. R.; SCZANCOSKI, J. C.; BELTRÁN-MIR, H.; LI, M. S.; ANDRÉS, J.; CORDONCILLO, E.; LEITE, E.; LONGO, E. "Structural properties and self-activated photoluminescence emissions in hydroxyapatite with distinct particle shapes". Ceramics International, 44 (1): 236, 2018.

57. DE FOGGI, C. C.; DE OLIVEIRA, R. C.; FABBRO, M. T.; VERGANI, C. E.; ANDRES, J.; LONGO, E.; MACHADO, A. L. "Tuning the morphological, optical, and antimicrobial properties of α-Ag_2WO_4 microcrystals using different solvents". Crystal Growth & Design, 17 (12): 6239, 2017.

58. NAKAMURA, S.; MUKAI, T.; SENOH, M. "Candela-class high-brightness InGaN/AlGaN double-heterostructure blue-light-emitting diodes". Applied Physics Letters, 64 (13): 1687, 1994.

59. MA, Y.; WANG, S.; WANG, L. "Nanomaterials for luminescence detection of nitroaromatic explosives". TrAC Trends in Analytical Chemistry, **65**: 13, 2015.

60. DHOBALE, A. R.; MOHAPATRA, M.; NATARAJAN, V.; GODBOLE, S. V. "Synthesis and photoluminescence investigations of the white light emitting phosphor, vanadate garnet, $Ca_2NaMg_2V_3O_{12}$ co-doped with Dy and Sm". Journal of Luminescence, 132 (2): 293, 2012.

61. HUANG, Y.; YU, Y. M.; TSUBOI, T.; SEO, H. J. "Novel yellow-emitting phosphors of $Ca_5M_4(VO_4)_6$ (M=Mg, Zn) with isolated VO_4 tetrahedra". Optics Express, 20 (4): 4360 2012.

62. ZHOU, J.; HUANG, F.; XU, J.; CHEN, H.; WANG, Y. "Luminescence study of a self-activated and rare earth activated $Sr_3La(VO_4)_3$ phosphor potentially applicable in W-LEDs". J. Mater. Chem. C, 3 (13): 3023, 2015.

63. HASEGAWA, T.; ABE, Y.; KOIZUMI, A.; UEDA, T.; TODA, K.; SATO, M. "Bluish-white luminescence in rare-earth-free vanadate garnet phosphors: structural characterization of $LiCa_3MV_3O_{12}$ (M = Zn and Mg)". Inorg Chem, 57 (2): 857, 2018.

64. RONDE, H.; BLASSE, G. "The nature of the electronic transitions of the vanadate group". Journal of Inorganic and Nuclear Chemistry, **40**: 215 1978.

65. NAKAJIMA, T.; ISOBE, M.; TSUCHIYA, T.; UEDA, Y.; KUMAGAI, T. "A revisit of photoluminescence property for vanadate oxides AVO_3 (A:K, Rb and Cs) and $M_3V_2O_8$ (M:Mg and Zn)". Journal of Luminescence, 129 (12): 1598, 2009.

66. RYBA-ROMANOWSKI, W.; GOŁĄB, S.; SOLARZ, P.; DOMINIAK-DZIK, G.; ŁUKASIEWICZ, T. "Anti-Stokes emission in undoped YVO_4". Applied Physics Letters, 80 (7): 1183, 2002.

67. HAZENKAMP, M. F.; STRIJBOSCH, A. W. P. M.; BLASSE, G. "Anomalous luminescence of two d^0 transition-metal complexes: $KVOF_4$ and K_2NbOF_5 - H_2O". Journal of Solid State Chemistry, **97**: 115 1992.

68. CAMPOS, A. B.; SIMÕES, A. Z.; LONGO, E.; VARELA, J. A.; LONGO, V. M.; DE FIGUEIREDO, A. T.; DE VICENTE, F. S.; HERNANDES, A. C. "Mechanisms behind blue, green, and red photoluminescence emissions in $CaWO_4$ and $CaMoO_4$ powders". Applied Physics Letters, 91 (5): 051923, 2007.

69. MONDEGO, M.; OLIVEIRA, R. C. D.; PENHA, M.; LIB, M. S.; LONGO, E. "Blue and red light photoluminescence emission at room temperature from $CaTiO_3$ decorated with α-Ag_2WO_4". Ceramics International, **43**: 5759, 2017.

70. LONGO, V. M.; CAVALCANTE, L. S.; FIGUEIREDO, A. T. D.; SANTOS, L. P. S. "Highly intense violet-blue light emission at room temperature in structurally disordered $SrZrO_3$ powders". Applied Physics Letters, 90 (9): 091906, 2007.

71. SMITH, M. D.; CONNOR, B. A.; KARUNADASA, H. I. "Tuning the luminescence of layered halide perovskites". Chem Rev, 119 (5): 3104, 2019.

72. ANICETE-SANTOS, M.; ORHAN, E.; DE MAURERA, M. A. M. A.; SIMÕES, L. G. P.; SOUZA, A. G.; PIZANI, P. S.; LEITE, E. R.; VARELA, J. A.; ANDRÉS, J.; BELTRÁN, A.; LONGO, E. "Contribution of structural order-

disorder to the green photoluminescence of $PbWO_4$". Physical Review B, 75 (16): 2007.

73. ORHAN, E.; VARELA, J. A.; ZENATTI, A.; GURGEL, M. F. C.; PONTES, F. M.; LEITE, E. R.; LONGO, E.; PIZANI, P. S.; BELTRÀN, A.; ANDRÈS, J. "Room-temperature photoluminescence of $BaTiO_3$: Joint experimental and theoretical study". Physical Review B, 71 (8): 2005.

74. CAVALCANTE, L. S.; SIMÕES, A. Z.; ESPINOSA, J. W. M.; SANTOS, L. P. S.; LONGO, E.; VARELA, J. A.; PIZANI, P. S. "Study of structural evolution and photoluminescent properties at room temperature of $Ca(Zr,Ti)O_3$ powders". Journal of Alloys and Compounds, 464 (1-2): 340, 2008.

75. LIQIANG, J.; YICHUN, Q.; BAIQI, W.; SHUDAN, L.; BAOJIANG, J.; LIBIN, Y.; WEI, F.; HONGGANG, F.; JIAZHONG, S. "Review of photoluminescence performance of nano-sized semiconductor materials and its relationships with photocatalytic activity". Solar Energy Materials and Solar Cells, 90 (12): 1773, 2006.

76. SUBBA REDDY, C. V.; YEO, I.-H.; MHO, S.-I. "Synthesis of sodium vanadate nanosized materials for electrochemical applications". Journal of Physics and Chemistry of Solids, 69 (5-6): 1261, 2008.

77. XU, D.; CAO, S.; ZHANG, J.; CHENG, B.; YU, J. "Effects of the preparation method on the structure and the visible-light photocatalytic activity of Ag_2CrO_4". Beilstein J Nanotechnol, **5**: 658, 2014.

78. CERVANTES-JUÁREZ, E.; MEZA-ROCHA, A. N.; LICONA-IBARRA, R.; CALDIÑO, U.; ALVAREZ-RAMOS, E.; QUIÑONES-GALVÁN, J. G.; LOZADA-MORALES, R. "Spectroscopy evaluation of crystalline and amorphous $Cd_2V_2O_7$ as blue phosphors". Journal of Luminescence, **195**: 234, 2018.

79. PU, Y.; HUANG, Y.; TSUBOI, T.; CHENG, H.; SEO, H. J. "Intrinsic $[VO_4]^{3-}$ emission of cesium vanadate $Cs_5V_3O_{10}$". RSC Advances, 5 (90): 73467, 2015.

80. NIE, X.; WULAYIN, W.; SONG, T.; WU, M.; QIAO, X. "Photoluminescence enhancement of self-activated vanadate $NaMg_4(VO_4)_3$ by cation substitutions". Materials Letters, **185**: 588, 2016.

81. LI, L.; WANG, W.; PAN, Y.; ZHU, Y.; LIU, X.; NOH, H. M.; MOON, B. K.; CHOI, B. C.; JEONG, J. H. "Preferential occupancy of Eu^{3+} and energy transfer in Eu^{3+} doped $Sr_2V_2O_7$, $Sr_9Gd(VO_4)_7$ and $Sr_2V_2O_7/Sr_9Gd(VO_4)_7$ phosphors". RSC Advances, 8 (3): 1191, 2018.

82. NAKAJIMA, T.; ISOBE, M.; TSUCHIYA, T.; UEDA, Y.; MANABE, T. "Correlation between luminescence quantum efficiency and structural properties of vanadate phosphors with chained, dimerized, and isolated VO_4 tetrahedra". The Journal of Physical Chemistry C, **114**: 5160, 2010.

83. PEI, L.; PEI, Y.; XIE, Y.; FAN, C.; LI, D.; ZHANG, Q. "Formation process of calcium vanadate nanorods and their electrochemical sensing properties". Journal of Materials Research, 27 (18): 2391, 2012.

84. LI, L.; ZHENG, S.; WANG, S.; DU, H.; ZHANG, Y. "Thermal hydrolysis synthesis and characterization of monoclinic metahewettite $CaV_6O_{16}\cdot 3H_2O$". Journal of Wuhan University of Technology-Mater. Sci. Ed., 29 (3): 433, 2014.

85. AYDIN, C. "Synthesis of SnO_2:rGO nanocomposites by the microwave-assisted hydrothermal method and change of the morphology, structural, optical and electrical properties". Journal of Alloys and Compounds, **771**: 964, 2019.

86. TEIXEIRA, M. M.; DE OLIVEIRA, R. C.; OLIVEIRA, M. C.; PONTES RIBEIRO, R. A.; DE LAZARO, S. R.; LI, M. S.; CHIQUITO, A. J.; GRACIA, L.; ANDRES, J.; LONGO, E. "Computational chemistry meets experiments for explaining the geometry, electronic structure, and optical properties of $Ca_{10}V_6O_{25}$". Inorg Chem, 57 (24): 15489, 2018.

87. ALAIN, M.; JACQUES, M.; DIANE, M.-B.; KARINE, P. "MAX: Multiplatform Applications for XAFS". Journal of Physics: Conference Series, **190**: 012034, 2009.

88. DOVESI, R.; SAUNDERS, V. R.; ROETTI, C.; ORLANDO, R.; ZICOVICH-WILSON, C. M.; PASCALE, F.; CIVALLERI, B.; DOLL, K.; HARRISON, N. M.; BUSH, I. J.; D'ARCO, P.; LLUNEL, M.; CAUSÀ, M.; NOËL, Y.; MASCHIO, L.; ERBA, A.; RÉRAT, M.; CASASSA, S. *CRYSTAL17 User's Manual (University of Torino, Torino, 2017)*, 2017.

89. BECKE, A. D. "Density-functional thermochemistry. III. The role of exact exchange". The Journal of Chemical Physics, 98 (7): 5648, 1993.

90. LEE, C.; YANG, W.; PARR, R. G. "Development of the Colle-Salvetti correlation-energy formula into a functional of the electron density". Physical Review B, 37 (2): 785, 1988.

91. MARQUES, A. P.; PICON, F. C.; MELO, D. M.; PIZANI, P. S.; LEITE, E. R.; VARELA, J. A.; LONGO, E. "Effect of the order and disorder of $BaMoO_4$ powders in photoluminescent properties". J Fluoresc, 18 (1): 51, 2008.

92. CAVALCANTE, L. S.; LONGO, V. M.; SCZANCOSKI, J. C.; ALMEIDA, M. A. P.; BATISTA, A. A.; VARELA, J. A.; ORLANDI, M. O.; LONGO, E.; LI, M. S. "Electronic structure, growth mechanism and photoluminescence of $CaWO_4$ crystals". CrystEngComm, 14 (3): 853, 2012.

93. RIETVELD, H. M. "Line profiles of neutron powder-diffraction peaks for structure refinement". Acta Crystallographica, **22**: 151, 1967.

94. LARSON, A. C.; VON DREELE, R. B. "General structure analysis system (GSAS)". Los Alamos, National Laboratory, 124, 2001.

95. WILHELMI, K. A.; JONSSON, O. "X-ray studies on some alkali and alkaline-earth chromates (V)". Acta Chemica Scandinavica, **19**: 177, 1965.

96. MOMMA, K.; IZUMI, F. "VESTA: a three-dimensional visualization system for electronic and structural analysis". Journal of Applied Crystallography, 41 (3): 653, 2008.

97. MOMMA, K.; IZUMI, F. "VESTA 3for three-dimensional visualization of crystal, volumetric and morphology data". Journal of Applied Crystallography, 44 (6): 1272, 2011.

98. PETIT, S.; GODE, T.; THOMAS, C.; DZWIGAJ, S.; MILLOT, Y.; BROURI, D.; KRAFFT, J. M.; ROUSSE, G.; LABERTY-ROBERT, C.; COSTENTIN, G. "Incorporation of vanadium into the framework of hydroxyapatites: importance of the vanadium content and pH conditions during the precipitation step". Phys Chem Chem Phys, 19 (14): 9630, 2017.

99. UNNIMAYA, A. N.; SURESH, E. K.; RATHEESH, R. "Crystal structure and microwave dielectric properties of new alkaline earth vanadate $A_4V_2O_9$ (A = Ba, Sr, Ca, Mg and Zn) ceramics for LTCC applications". Materials Research Bulletin, **88**: 174, 2017.

100. GRZECHNIK, A. "High-temperature transformations in calcium orthovanadate studied with raman scattering". Chemistry of Materials, 10 (4): 1034, 1998.

101. AVANSI, W.; RIBEIRO, C.; LEITE, E. R.; MASTELARO, V. R. "An efficient synthesis route of $Na_2V_6O_{16}{\cdot}nH_2O$ nanowires in hydrothermal conditions". Materials Chemistry and Physics, 127 (1-2): 56, 2011.

102. CAVALCANTE, L. S.; BATISTA, N. C.; BADAPANDA, T.; COSTA, M. G. S.; LI, M. S.; AVANSI, W.; MASTELARO, V. R.; LONGO, E.; ESPINOSA,

J. W. M.; GURGEL, M. F. C. "Local electronic structure, optical bandgap and photoluminescence (PL) properties of $Ba(Zr_{0.75}Ti_{0.25})O_3$ powders". Materials Science in Semiconductor Processing, 16 (3): 1035, 2013.

103. CAVALCANTE, L. S.; ALMEIDA, M. A.; AVANSI, W., JR.; TRANQUILIN, R. L.; LONGO, E.; BATISTA, N. C.; MASTELARO, V. R.; LI, M. S. "Cluster coordination and photoluminescence properties of α-Ag_2WO_4 microcrystals". Inorg Chem, 51 (20): 10675, 2012.

104. DA SILVA, L. F.; AVANSI, W.; MOREIRA, M. L.; MESQUITA, A.; MAIA, L. J. Q.; ANDRÉS, J.; LONGO, E.; MASTELARO, V. R. "Relationship between crystal shape, photoluminescence, and local structure in $SrTiO_3$ synthesized by microwave-assisted hydrothermal method". Journal of Nanomaterials, **2012**: 1, 2012.

105. GRACIA, L.; LONGO, V. M.; CAVALCANTE, L. S.; BELTRÁN, A.; AVANSI, W.; LI, M. S.; MASTELARO, V. R.; VARELA, J. A.; LONGO, E.; ANDRÉS, J. "Presence of excited electronic state in $CaWO_4$ crystals provoked by a tetrahedral distortion: An experimental and theoretical investigation". Journal of Applied Physics, 110 (4): 043501, 2011.

106. MAZZO, T. M.; MENDONÇA DA ROCHA OLIVEIRA, L.; MACARIO, L. R.; AVANSI, W.; SILVEIRA ANDRÉ, R. D.; VIANA ROSA, I. L.; VARELA, J. A.; LONGO, E. "Photoluminescence properties of $CaTiO_3$:Eu^{3+} nanophosphor obtained by the polymeric precursor method". Materials Chemistry and Physics, 145 (1-2): 141, 2014.

107. AVANSI, W.; ARENAL, R.; DE MENDONÇA, V. R.; RIBEIRO, C.; LONGO, E. "Vanadium-doped TiO_2 anatase nanostructures: the role of V in solid solution formation and its effect on the optical properties". Crystengcomm, 16 (23): 5021, 2014.

108. AVANSI, W.; MAIA, L. J. Q.; RIBEIRO, C.; LEITE, E. R.; MASTELARO, V. R. "Local structure study of vanadium pentoxide 1D-nanostructures". Journal of Nanoparticle Research, 13 (10): 4937, 2011.

109. OLIVEIRA, L. H.; PARIS, E. C.; AVANSI, W.; RAMIREZ, M. A.; MASTELARO, V. R.; LONGO, E.; VARELA, J. A.; CHEN, X. M. "Correlation between photoluminescence and structural defects in $Ca_{1+x}Cu_{3-x}Ti_4O_{12}$ systems". Journal of the American Ceramic Society, 96 (1): 209, 2013.

110. CHAURAND, P.; ROSE, J.; BRIOIS, V.; SALOME, M.; PROUX, O.; NASSIF, V.; OLIVI, L.; SUSINI, J.; HAZEMANN, J.-L.; BOTTERO, J.-Y. "New methodological approach for the vanadium K-Edge X-ray absorption near-edge

structure interpretation: application to the speciation of vanadium in oxide phases from steel slag". Journal of Physical Chemistry B, **111**: 5101, 2007.

111. MANSOUR, A. N.; SMITH, P. H.; BALASUBRAMANIAN, M.; MCBREEN, J. "In situ x-ray absorption study of cycled ambigel $V_2O_5{\cdot}nH_2O$($n \approx$ 0.5) composite cathodes". Journal of The Electrochemical Society, 152 (7): A1312, 2005.

112. STIZZA, S.; MANCINI, G.; BENFATTO, M.; NATOLI, C. R.; GARCIA, J.; BIANCONI, A. "Structure of oriented V_2O_5 gel studied by polarized x-ray-absorption spectroscopy at the vanadium K edge". Physical Review B, 40 (18): 12229, 1989.

113. NABAVI, M.; TAULELLE, F.; SANCHEZ, C.; VERDAGUER, M. "XANES and ^{51}V NMR study of vanadium-oxygen compounds". Journal of Physics and Chemistry of Solids, 51 (12): 1375, 1990.

114. PHILIPS-INVERNIZZI, B. "Bibliographical review for reflectance of diffusing media". Optical Engineering, 40 (6): 1082, 2001.

115. WOOD, D. L.; TAUC, J. "Weak absorption tails in amorphous semiconductors". Physical Review B, 5 (8): 3144, 1972.

116. URBACH, F. "The long-wavelength edge of photographic sensitivity and of the electronic absorption of solids". Physical Review, 92 (5): 1324, 1953.

117. CAVALCANTE, L. S.; ALMEIDA, M. A.; AVANSI, W., JR.; TRANQUILIN, R. L.; LONGO, E.; BATISTA, N. C.; MASTELARO, V. R.; LI, M. S. "Cluster coordination and photoluminescence properties of α-Ag_2WO_4 microcrystals". Inorg Chem, 51 (20): 10675, 2012.

118. DUTTA, D. P.; GHILDIYAL, R.; TYAGI, A. K. "Luminescent properties of doped zinc aluminate and zinc gallate white light emitting nanophosphors prepared via sonochemical method". Journal of Physical Chemistry C, 113 (39): 16954, 2009.

119. SINDHU, H. S.; RAJENDRA, B. V.; HEBBAR, N. D.; KULKARNI, S. D.; BABU, P. D. "Defect induced white-light emission from Mn–doped ZnO films and its magnetic properties". Journal of Luminescence, **199**: 423, 2018.

120. DREIFUS, D.; GODOY, M. P. F.; RABELO, A. C.; RODRIGUES, A. D.; GOBATO, Y. G.; CAMARGO, P. C.; PEREIRA, E. C.; DE OLIVEIRA, A. J. A. "Antiferromagnetism induced by oxygen vacancies in V_2O_5 polycrystals synthesized by the Pechini method". Journal of Physics D: Applied Physics, 48 (44): 445002, 2015.

121. PAVITRA, E.; RAJU, G. S.; PARK, J. Y.; WANG, L.; MOON, B. K.; YU, J. S. "Novel rare-earth-free yellow $Ca_5Zn_{3.92}In_{0.08}(V_{0.99}Ta_{0.01}O_4)_6$ phosphors for dazzling white light-emitting diodes". Sci Rep, **5**: 10296, 2015.

122. PARK, K.-C.; MHO, S.-I. "Photoluminescence properties of $Ba_3V_2O_8$, $Ba_{3(1-x)}Eu_{2x}V_2O_8$ and $Ba_2Y_{2/3}V_2O_8$:Eu^{3+}". Journal of Luminescence, **122-123**: 95, 2007.

123. KIM, S. W.; HASEGAWA, T.; MUTO, M.; TODA, A.; KANEKO, T.; SUGIMOTO, K.; UEMATSU, K.; ISHIGAKI, T.; TODA, K.; SATO, M.; KOIDE, J.; TODA, M.; KUDO, Y. "Improvement of luminescence properties of rubidium vanadate, $RbVO_3$, phosphors by erbium doping in the crystal lattice". New Journal of Chemistry, 41 (12): 4788, 2017.

124. LU, Z.; WANG, H.; YU, D.; HUANG, T.; WEN, L.; HUANG, M.; ZHOU, L.; WANG, Q. "Synthesis and luminescence properties of a double perovskite Ca_2LaNbO_6:Mn^{4+} deep-red phosphor". Optics & Laser Technology, **108**: 116, 2018.

125. CHEN, W.; CHENG, Y.; SHEN, L.; SHEN, C.; LIANG, X.; XIANG, W. "Red-emitting $Sr_2MgGe_2O_7$:Mn^{4+} phosphors: Structure, luminescence properties, and application in warm white light emitting diodes". Journal of Alloys and Compounds, **762**: 688, 2018.

126. JOUANNEAU, S.; VERBAERE, A.; GUYOMARD, D. "On a new calcium vanadate: synthesis, structure and Li insertion behavior". Journal of Solid State Chemistry, 172 (1): 116, 2003.

127. LUKE, G. M.; FUDAMOTO, Y.; GINGRAS, M. J. P.; KOJIMA, K. M.; LARKIN, M.; MERRIN, J.; NACHUMI, B.; UEMURA, Y. J. "Spin freezing and ordering in CaV_4O_9, CaV_3O_7 and CaV_2O_5". Journal of Magnetism and Magnetic Materials, **177-181**: 754, 1998.

128. CURELARU, I. M.; STRID, K. G.; SUONINEN, E.; MINNI, E.; RÖNNHULT, T. "Electron structure of excited configurations in $Ca_2V_2O_7$ studied by electron-induced core-ionization loss spectroscopy, appearance-potential spectroscopy, and x-ray-photoelectron spectroscopy". Physical Review B, 23 (8): 3700, 1981.

129. PARHI, P.; MANIVANNAN, V.; KOHLI, S.; MCCURDY, P. "Synthesis and characterization of $M_3V_2O_8$ (M = Ca, Sr and Ba) by a solid-state metathesis approach". Bulletin of Materials Science, **31**: 885, 2008.

130. JACOB, K. T.; GUPTA, P. "Gibbs energy of formation of $Ca_7V_4O_{17}$". The Journal of Chemical Thermodynamics, **63**: 7, 2013.

131. ZHANG, S.; MU, W. "Fabrication of $Ca_2V_2O_7$ microspheres and its application in lithium-ion batteries". Materials Letters, **183**: 311, 2016.

132. OGO, S.; ONDA, A.; YANAGISAWA, K. "Hydrothermal synthesis of vanadate-substituted hydroxyapatites, and catalytic properties for conversion of 2-propanol". Applied Catalysis A: General, 348 (1): 129, 2008.

133. QIU, K.; LI, J.; LI, J.; LU, X.; GONG, Y.; LI, J. "Luminescence property of $Ca_3(VO_4)_2$:Eu^{3+} dependence on molar ratio of Ca/V and solution combustion synthesis temperature". Journal of Materials Science, 45 (20): 5456, 2010.

134. ZHAN, G.; NG, W. C.; KOH, S. N.; WANG, C.-H. "Template-free synthesis of alkaline earth vanadates nanomaterials from leaching solutions of oil refinery waste". ACS Sustainable Chemistry & Engineering, 6 (2): 2292, 2018.

135. LI, L.; WANG, S.; DU, H.; ZHENG, S.; ZHANG, Y. "Equilibrium data of the KOH–K_3VO_4–$Ca(OH)_2$–H_2O system at (313.2 and 353.2) K". Journal of Chemical & Engineering Data, 57 (9): 2367, 2012.

136. ADAMS, D. M.; GARDNER, I. R. "Single-crystal vibrational spectra of apatite, vanadinite, and mimetite". Journal of the Chemical Society-Dalton Transactions, **14**: 1505, 1974.

137. FROST, R. L.; CRANE, M.; WILLIAMS, P. A.; THEO KLOPROGGE, J. "Isomorphic substitution in vanadinite [$Pb_5(VO_4)_3Cl$]- a Raman spectroscopic study". Journal of Raman Spectroscopy, 34 (3): 214, 2003.

138. BARTHOLOMÄI, G.; KLEE, W. E. "The vibrational spectra of pyromorphite, vanadinite and mimetite". Spectrochimica Acta, **34A**: 831 1978.

139. BAGHBANZADEH, M.; CARBONE, L.; COZZOLI, P. D.; KAPPE, C. O. "Microwave-assisted synthesis of colloidal inorganic nanocrystals". Angew Chem Int Ed Engl, 50 (48): 11312, 2011.

140. KOMARNENI, S.; ROY, R.; LI, Q. H. "Microwave-hydrothermal synthesis of ceramic powders". Materials Research Bulletin, **27**: 1393, 1992.

141. BILECKA, I.; NIEDERBERGER, M. "Microwave chemistry for inorganic nanomaterials synthesis". Nanoscale, 2 (8): 1358, 2010.

142. OLIVER KAPPE, C. "Microwave dielectric heating in synthetic organic chemistry". Chemical Society Reviews, 37 (6): 1127, 2008.

143. MOREIRA, M. L.; ANDRÉS, J.; VARELA, J. A.; LONGO, E. "Synthesis of fine micro-sized $BaZrO_3$ powders based on a decaoctahedron shape by the microwave-assisted hydrothermal method". Crystal Growth & Design, **9**: 833, 2009.

144. VOLANTI, D. P.; SATO, A. G.; ORLANDI, M. O.; BUENO, J. M. C.; LONGO, E.; ANDRÉS, J. "Insight into copper-based catalysts: microwave-assisted morphosynthesis, in situ reduction studies, and dehydrogenation of ethanol". Chemcatchem, **3**: 839, 2011.

145. DA SILVA, L. F.; AVANSI, W.; ANDRES, J.; RIBEIRO, C.; MOREIRA, M. L.; LONGO, E.; MASTELARO, V. R. "Long-range and short-range structures of cube-like shape $SrTiO_3$ powders: microwave-assisted hydrothermal synthesis and photocatalytic activity". Phys Chem Chem Phys, 15 (29): 12386, 2013.

146. DA SILVA, L. F.; CATTO, A. C.; AVANSI, W.; CAVALCANTE, L. S.; MASTELARO, V. R.; ANDRÉS, J.; AGUIR, K.; LONGO, E. "Acetone gas sensor based on α-Ag_2WO_4 nanorods obtained via a microwave-assisted hydrothermal route". Journal of Alloys and Compounds, **683**: 186, 2016.

147. DOVESI, R.; ORLANDO, R.; ERBA, A.; ZICOVICH-WILSON, C. M.; CIVALLERI, B.; CASASSA, S.; MASCHIO, L.; FERRABONE, M.; DE LA PIERRE, M. "CRYSTAL14: A program for the Ab initio investigation of crystalline solids". International Journal of Quantum Chemistry, **114**: 1287, 2014.

148. BELTRÁN, A.; GRACIA, L.; ANDRÉS, J.; LONGO, E. "First-principles study on polymorphs of $AgVO_3$: assessing to structural stabilities and pressure-induced transitions". The Journal of Physical Chemistry C, 121 (49): 27624, 2017.

149. RIBEIRO, R. A. P.; DE LAZARO, S. R.; PIANARO, S. A. "Density Functional Theory applied to magnetic materials: Mn_3O_4 at different hybrid functionals". Journal of Magnetism and Magnetic Materials, **391**: 166, 2015.

150. MOREIRA, M. L.; BUZOLIN, P. G.; LONGO, V. M.; NICOLETI, N. H.; SAMBRANO, J. R.; LI, M. S.; VARELA, J. A.; LONGO, E. "Joint experimental and theoretical analysis of order-disorder effects in cubic $BaZrO_3$ assembled nanoparticles under decaoctahedral shape". J Phys Chem A, 115 (17): 4482, 2011.

151. OLIVEIRA, F. K. F.; OLIVEIRA, M. C.; GRACIA, L.; TRANQUILIN, R. L.; PASKOCIMAS, C. A.; MOTTA, F. V.; LONGO, E.; ANDRÉS, J.; BOMIO,

M. R. D. "Experimental and theoretical study to explain the morphology of $CaMoO_4$ crystals". Journal of Physics and Chemistry of Solids, **114**: 141, 2018.

152. VALENZANO, L.; TORRES, F. J.; DOLL, K.; PASCALE, F.; ZICOVICH-WILSON, C. M.; DOVESI, R. "Ab initio study of the vibrational spectrum and related properties of crystalline compounds; the case of $CaCO_3$ calcite". Zeitschrift für Physikalische Chemie, 220 (7_2006): 893, 2006.

153. MACKRODT, W. C.; HARRISON, N. M.; SAUNDERS, V. R.; ALLAN, N. L.; TOWLER, M. D.; APRÀ, E.; DOVESI, R. "Ab initio Hartree-Fock calculations of CaO, VO, MnO and NiO". Philosophical Magazine A, 68 (4): 653, 1993.

154. CORNO, M.; BUSCO, C.; CIVALLERI, B.; UGLIENGO, P. "Periodic ab initio study of structural and vibrational features of hexagonal hydroxyapatite $Ca_{10}(PO_4)_6(OH)_2$". Phys Chem Chem Phys, 8 (21): 2464, 2006.

155. MONKHORST, H. J.; PACK, J. D. "Special points for Brillouin-zone integrations". Physical Review B, 13 (12): 5188, 1976.

156. DA SILVA, L. F.; M'PEKO, J.-C.; ANDRÉS, J.; BELTRÁN, A.; GRACIA, L.; BERNARDI, M. I. B.; MESQUITA, A.; ANTONELLI, E.; MOREIRA, M. L.; MASTELARO, V. R. "Insight into the effects of fe addition on the local structure and electronic properties of $SrTiO_3$". The Journal of Physical Chemistry C, 118 (9): 4930, 2014.

157. LONGO, V. M.; DAS GRACA SAMPAIO COSTA, M.; ZIRPOLE SIMOES, A.; ROSA, I. L.; SANTOS, C. O.; ANDRES, J.; LONGO, E.; VARELA, J. A. "On the photoluminescence behavior of samarium-doped strontium titanate nanostructures under UV light. A structural and electronic understanding". Phys Chem Chem Phys, 12 (27): 7566, 2010.

158. GRACIA, L.; ANDRÉS, J.; LONGO, V. M.; VARELA, J. A.; LONGO, E. "A theoretical study on the photoluminescence of $SrTiO_3$". Chemical Physics Letters, 493 (1-3): 141, 2010.

159. OLIVEIRA, M. C.; GRACIA, L.; DE ASSIS, M.; ROSA, I. L. V.; DO CARMO GURGEL, M. F.; LONGO, E.; ANDRÉS, J. "Mechanism of photoluminescence in intrinsically disordered $CaZrO_3$ crystals: First principles modeling of the excited electronic states". Journal of Alloys and Compounds, **722**: 981, 2017.

160. MOURA, M. R.; AYALA, A. P.; GUEDES, I.; GRIMSDITCH, M.; LOONG, C. K.; BOATNER, L. A. "Raman scattering study of $Tb(V_{1-x}P_x)O_4$ single crystals". Journal of Applied Physics, 95 (3): 1148, 2004.

161. LIU, K.; YOU, H.; JIA, G.; ZHENG, Y.; HUANG, Y.; SONG, Y.; YANG, M.; ZHANG, L.; ZHANG, H. "Hierarchically nanostructured coordination polymer: facile and rapid fabrication and tunable morphologies". Crystal Growth & Design, 10 (2): 790, 2010.

162. TANG, J.; ALIVISATOS, P. A. "Crystal splitting in the growth of Bi_2S_3". Nano Letters, **6**: 2701, 2006.

163. ZHAO, Y.; SHI, H.; CHEN, M.; TENG, F. "Splitting growth of novel CuO straw sheaves and their improved photocatalytic activity due to exposed active {110} facets and crystallinity". Crystengcomm, 16 (12): 2417, 2014.

164. WU, S.; ZHANG, J.; SHI, L.; TANG, S.; LI, Y.; JIANG, L.; CUI, Q. "Template-free synthesis of α-GaOOH hyperbranched nanoarchitectures via crystal splitting and their optical properties". RSC Advances, 4 (16): 8209, 2014.

165. CESARE, F. "Hybrid functionals applied to perovskites". Journal of Physics: Condensed Matter, 26 (25): 253202, 2014.

166. GARZA, A. J.; SCUSERIA, G. E. "Predicting band gaps with hybrid density functionals". J Phys Chem Lett, 7 (20): 4165, 2016.

167. MOREIRA, M. L.; ANDRÉS, J.; GRACIA, L.; BELTRÁN, A.; MONTORO, L. A.; VARELA, J. A.; LONGO, E. "Quantum mechanical modeling of excited electronic states and their relationship to cathodoluminescence of $BaZrO_3$". Journal of Applied Physics, 114 (4): 043714, 2013.

168. GRACIA, L.; LONGO, V. M.; CAVALCANTE, L. S.; BELTRÁN, A.; AVANSI, W.; LI, M. S.; MASTELARO, V. R.; VARELA, J. A.; LONGO, E.; ANDRÉS, J. "Presence of excited electronic state in $CaWO_4$ crystals provoked by a tetrahedral distortion: An experimental and theoretical investigation". Journal of Applied Physics, 110 (4): 043501, 2011.

Appendix A

Supplementary Information of Chapter III

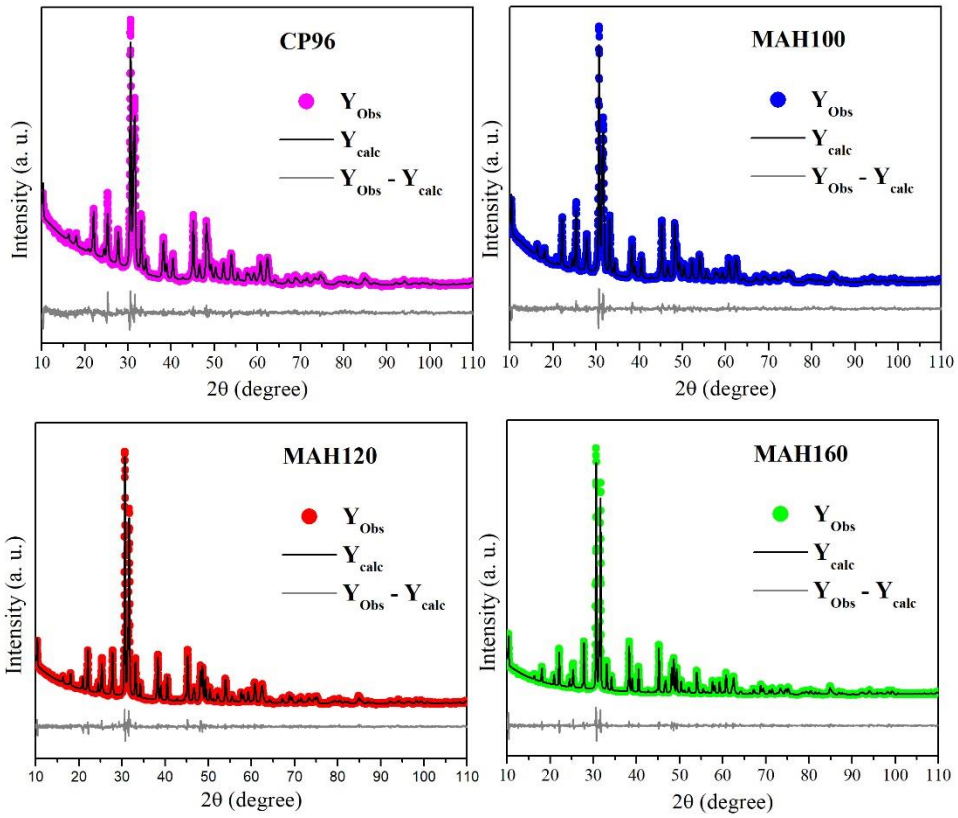

FIGURE A1 - Rietveld refinement plots of the $Ca_{10}V_6O_{25}$ samples synthetized via different methods and temperatures conditions, based on data from the ICSD card No. 24100.

TABLE A1 - Structural parameters obtained from Rietveld refinements for $Ca_{10}V_6O_{25}$ samples obtained via different methods and temperature conditions.

	CP96	MAH100	MAH120	MAH160
w R_p (%)	6.54	6.76	6.94	7.88
R_p (%)	4.96	5.07	5.22	5.78
χ^2	2.116	2.040	2.215	2.830
R_{Bragg}	0.0682	0.0616	0.0559	0.0711
a = b	9.75508	9.75531	9.75511	9.75937
c	6.98975	6.99186	6.99662	7.00818
Cell volume $(Å)^3$	576.042	576.243	576.612	578.069

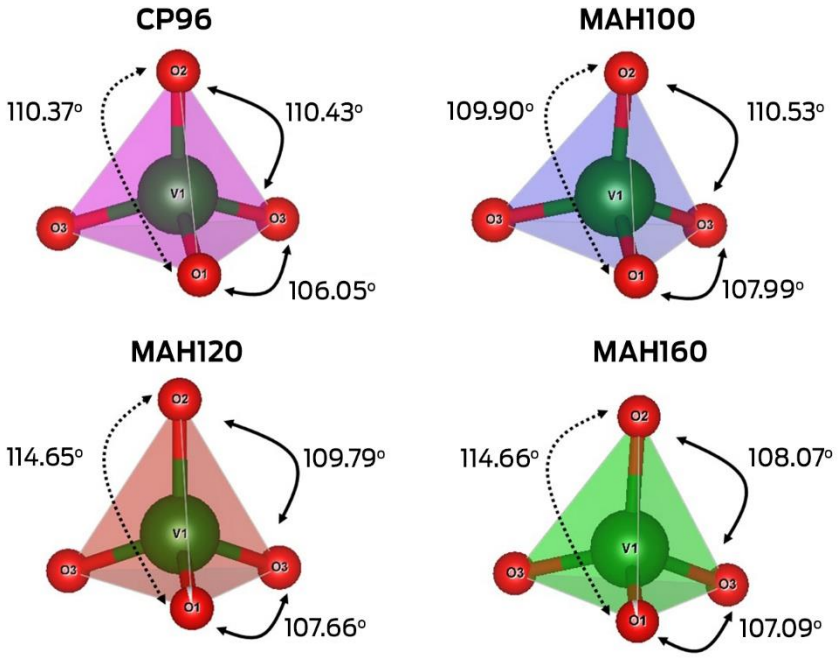

FIGURE A2 - O–V–O bond angles of tetrahedral [VO_4] clusters of the $Ca_{10}V_6O_{25}$ samples obtained by the CP method at 96 °C and the MAH method at temperatures of 100, 120, and 160 °C.

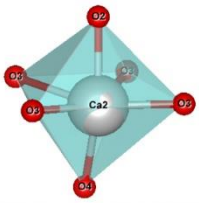

Samples	Octahedron Bond angles (º)				
	O2 - Ca - O3	O2 - Ca - O3	O2 - Ca - O4	O4 - Ca - O3	O4 - Ca - O3
CP96	88.41	78.68	154.61	100.45	80.41
MAH100	88.43	78.21	155.92	100.48	81.83
MAH120	89.47	73.66	150.64	101.09	82.11
MAH160	89.07	75.30	152.31	101.01	82.03

FIGURE A3 - O–Ca–O bond angles of octahedral [CaO_6] clusters of the $Ca_{10}V_6O_{25}$ samples obtained by different methods and temperature conditions.

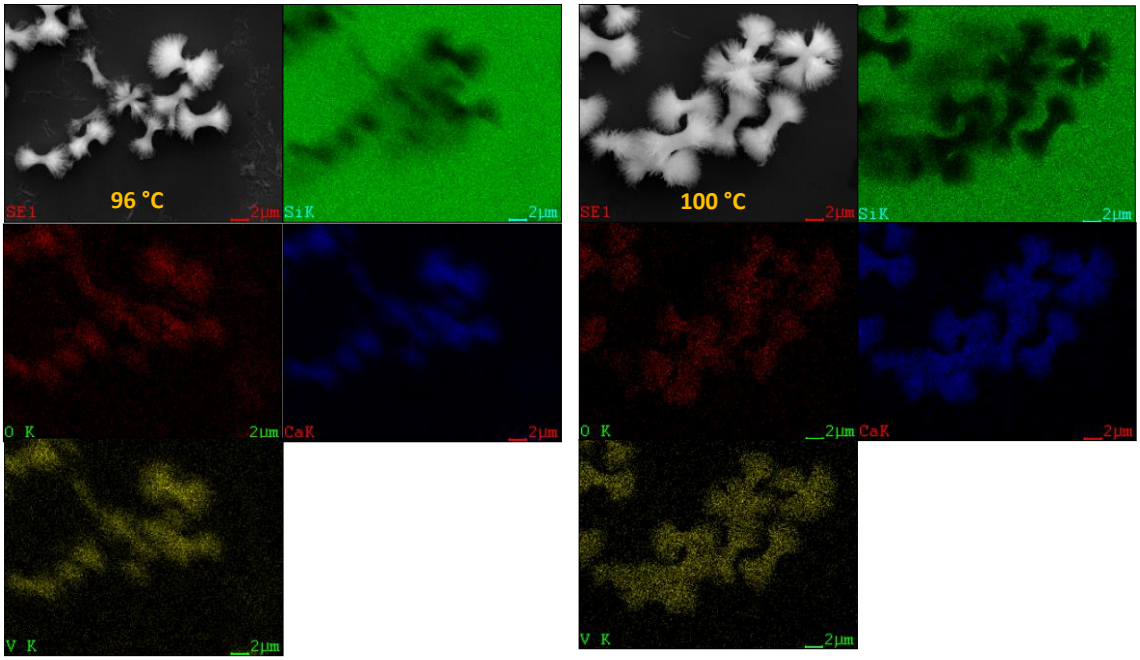

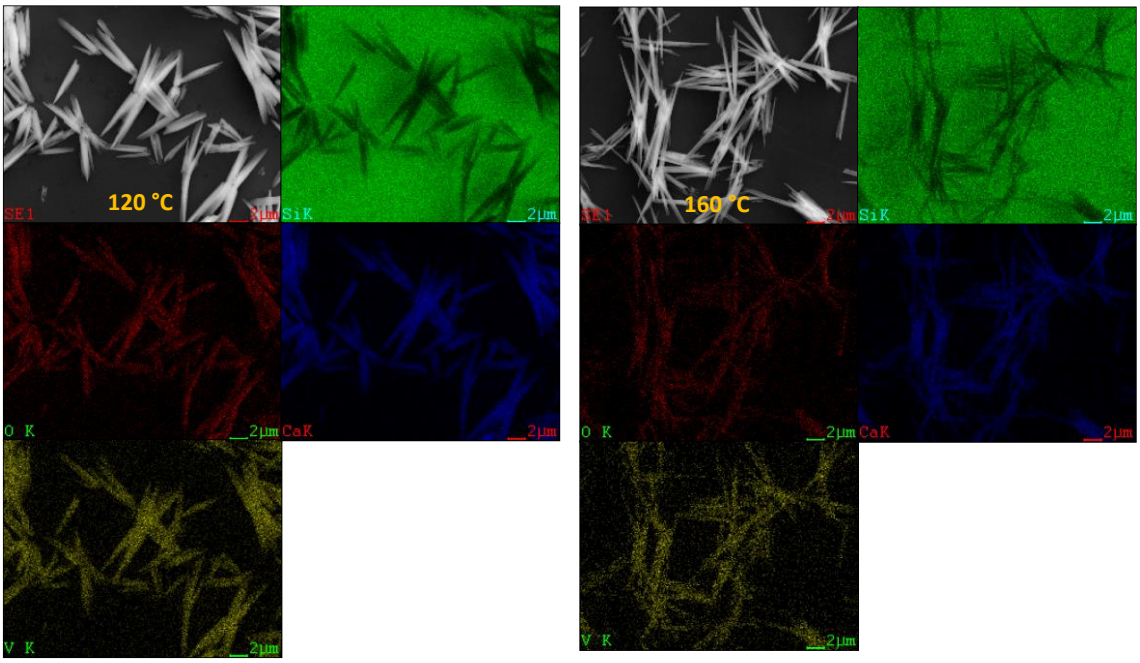

FIGURE A4 - Chemical composition map obtained by EDX of the $Ca_{10}V_6O_{25}$ samples obtained by the CP method at 96 °C and the MAH method at temperatures of 100, 120, and 160 °C.

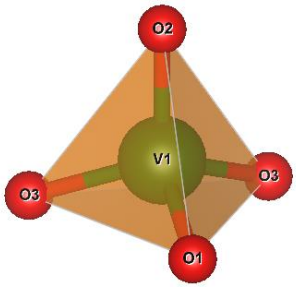

	Bond length (Å)		
Sample	V1 – O1	V1 – O2	V1 – O3
CP96	1.82	1.70	1.77
MAH100	1.76	1.69	1.74
MAH120	1.82	1.81	1.77
MAH160	1.77	1.82	1.77

FIGURE A5 - V–O bond length of [VO_4] clusters of the $Ca_{10}V_6O_{25}$ samples obtained by different methods and temperature conditions.

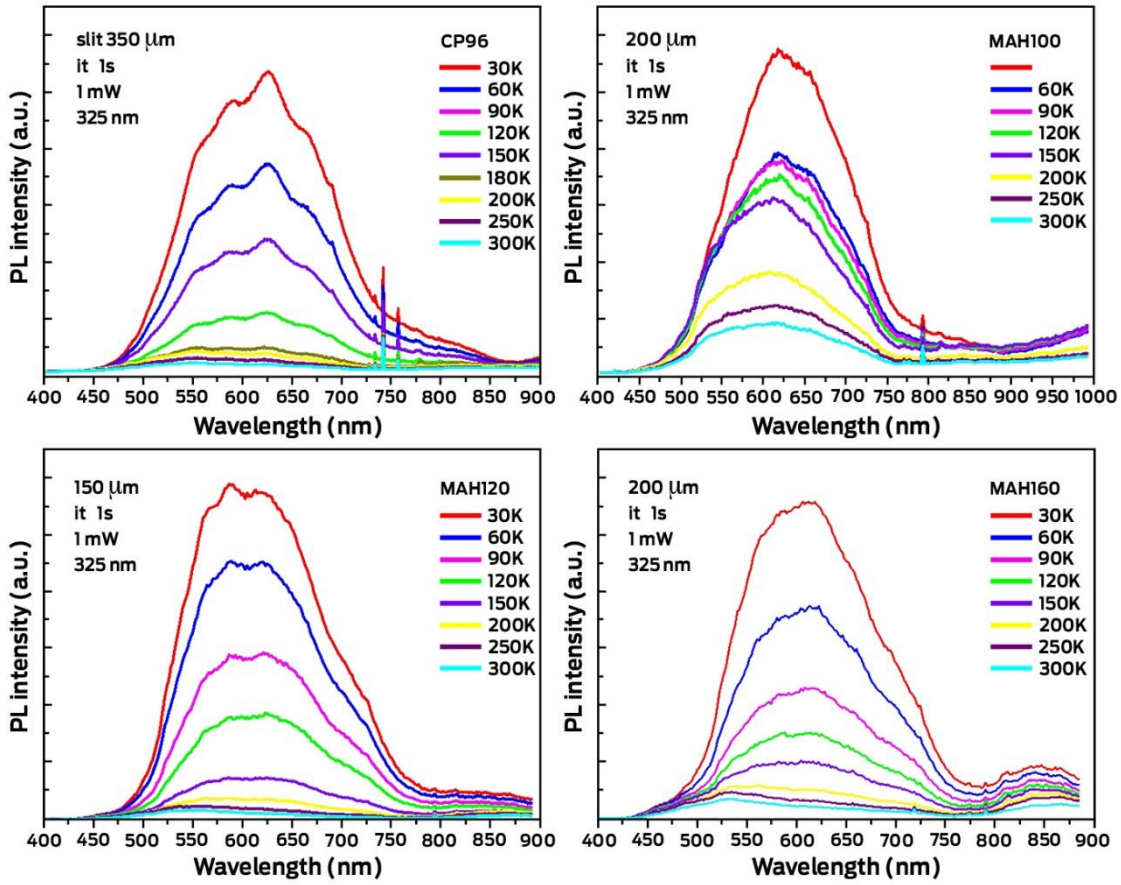

FIGURE A6 - Temperature dependence luminescence of the $Ca_{10}V_6O_{25}$ samples obtained by the CP method at 96 °C and the MAH method at temperatures of 100, 120, and 160 °C.

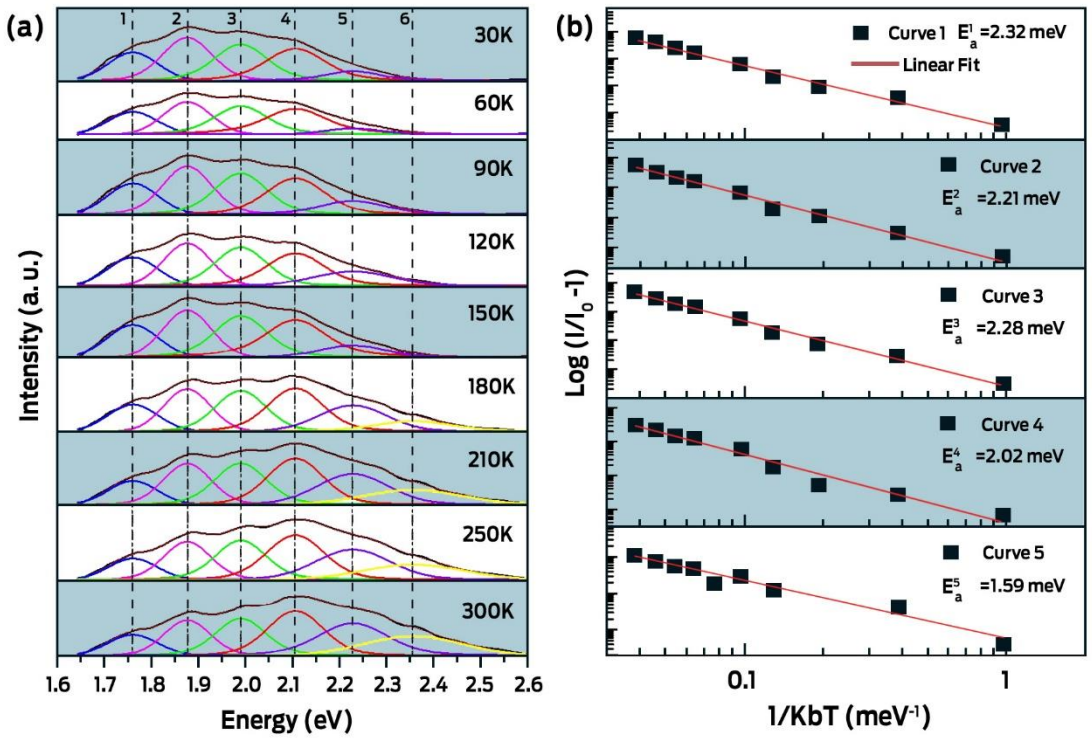

FIGURE A7 - (a) Deconvolution of the PL band spectrum using the Voigt Area G/L function. (b) Arrhenius plots of log ((I_0/I) - 1) versus 1/k_BT. The $Ca_{10}V_6O_{25}$ sample obtained by CP method at 96 °C.

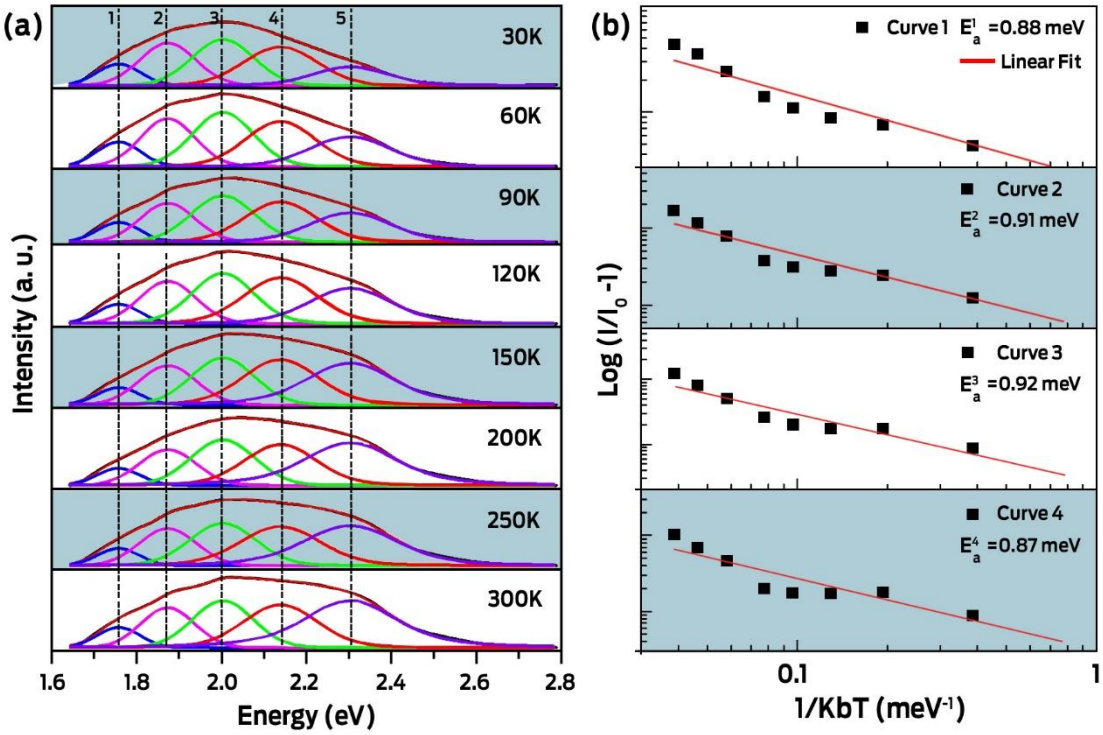

FIGURE A8 - (a) Deconvolution of the PL band spectrum using the Voigt Area G/L function. (b) Arrhenius plots of log ((I_0/I) - 1) versus 1/k_BT. The $Ca_{10}V_6O_{25}$ sample obtained by MAH method at 100 °C.

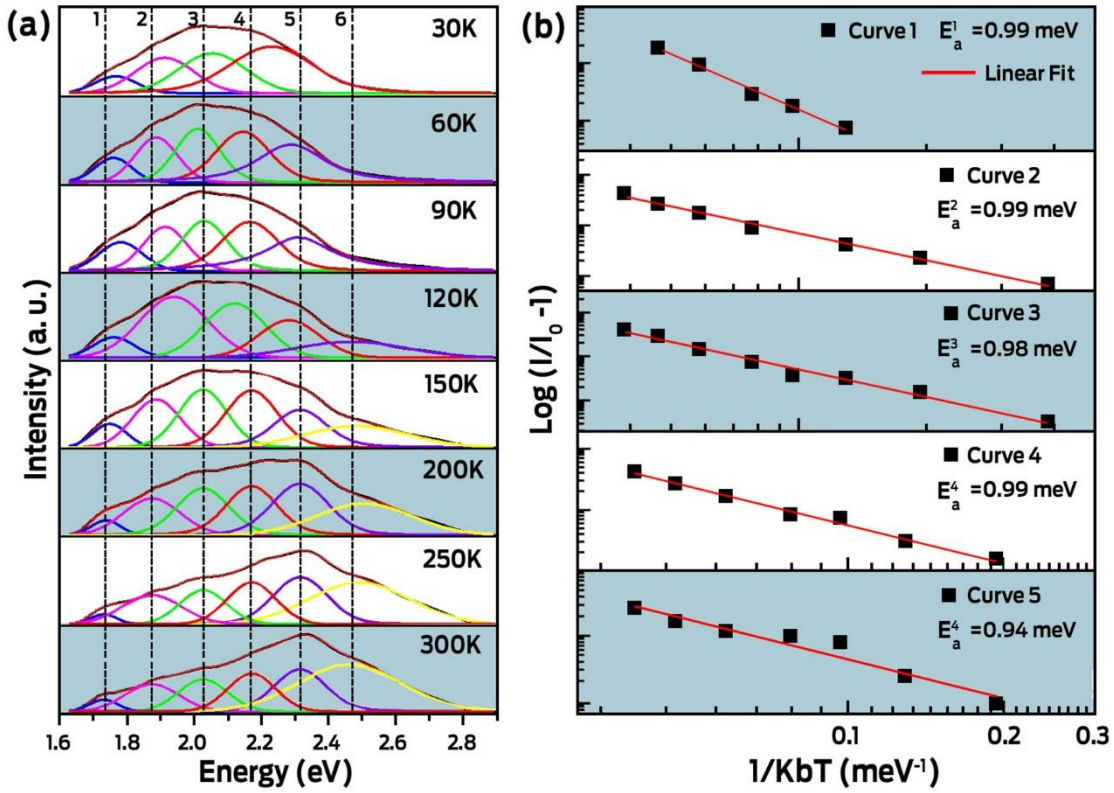

FIGURE A9 - (a) Deconvolution of the PL band spectrum using the Voigt Area G/L function. (b) Arrhenius plots of log ((I_0/I) - 1) versus 1/k_BT. The $Ca_{10}V_6O_{25}$ sample obtained by MAH method at 160 °C.

Appendix B

Supplementary Information of Chapter IV

TABLE B1 - Results obtained from Rietveld refinements and DFT calculations for $Ca_{10}V_6O_{25}$ material.

$Ca_{10}V_6O_{25}$ Time (min)		Lattice Parameter (Å)		β = α (°)	γ (°)	d g/cm³	Cell volume (Å)³	R_{Bragg} (%)	χ^2 (%)
		a = b	*c*						
Exp.	04	9.7328	7.0014	90	120	3.263	574.375	0.0572	1.882
	08	9.7432	7.0072	90	120	3.235	576.084	0.0848	2.189
	16	9.7171	7.0057	90	120	3.254	572.868	0.0688	2.033
	32	9.7407	6.9961	90	120	3.260	574.869	0.0847	2.497
Theoretical		9.6719	6.9793	90	120	3.246		-	-

TABLE B2 - Theoretical and experimental values of the Raman frequencies calculated and experimental of $Ca_{10}V_6O_{25}$ crystal. The symbols B, S and R correspond to Bending, Stretching and Rotational type of motions.

Raman mode	Type of motion	Theoretical (cm^{-1})	Experimental (cm^{-1})
E'	R	-55.02	-
E'	R	89.38	90
E'	R	97.98	
E"	B	107.20	
A'	S	114.20	
E"	B	124.14	126
E'	B	126.43	
A'	B	127.57	
A'	S	138.76	
E"	B	145.00	
E'	B	167.96	
A'	B	179.04	
E'	B	180.48	
A'	B	188.33	
E"	B	191.33	
E'	B	204.69	202
A'	S	207.62	
E"	S	210.81	
E'	S	214.09	
A'	B	224.46	
E"	B	228.99	
E'	B	237.07	235
E"	B	246.12	
E'	S	246.22	
A'	S	246.70	
E'	S	261.60	
A'	B	262.58	276
A'	S	288.37	
E'	B	293.77	
A'	S	308.60	
E"	S	309.65	
A'	S	334.79	
E"	S	348.26	352
E"	S	379.40	391
E'	S	393.58	
A'	S	394.95	
E"	B	400.22	407
E'	B	411.41	
E"	S	416.38	
A'	B	427.11	
E'	B	447.10	
A'	S	456.41	
E'	B	459.33	
E"	B	463.86	

E’	B	469.10	
A’	B	475.56	
A’	B	508.22	
E’	B	511.03	
A’	S	526.88	
E’	S	548.08	
E’	S	859.60	822
A’	S	867.34	862
E’	S	891.02	
A’	S	906.14	
E’	S	913.37	
E”	S	926.92	
E’	S	937.36	
A’	S	950.97	
E”	S	952.18	
A’	S	956.78	
E’	S	958.08	
A’	S	984.13	
E’	S	985.67	
A’	S	1020.96	1062

TABLE B3 - Values of the Raman frequencies calculated for $Ca_{10}V_6O_{25}$ crystal in the singlet (s*) and triplet (t*) excited state.

Raman mode	s* (cm^{-1})	Raman mode	t* (cm^{-1})
E"	-79.33	**E'**	-1963.99
E'	82.99	**E"**	-95.90
E'	91.62	**E'**	75.48
E"	93.05	**E"**	78.43
A'	112.35	**E'**	94.05
E"	116.15	**E"**	115.69
E'	126.69	**A'**	116.26
A'	128.30	**E'**	128.51
A'	134.05	**A'**	129.20
E"	140.28	**A'**	137.23
E'	164.65	**E"**	139.05
A'	167.90	**E'**	166.50
E'	176.98	**A'**	176.36
A'	184.08	**E'**	182.72
E"	186.90	**E"**	187.36
A'	199.10	**A'**	189.33
E'	199.36	**E"**	197.14
E"	200.92	**A'**	199.24
E'	210.37	**E'**	209.70
E"	220.20	**E'**	219.73
A'	220.40	**A'**	221.44
E'	229.55	**E"**	223.38
E"	239.14	**E"**	235.66
A'	241.40	**A'**	244.35
E'	243.84	**E'**	245.40
E'	256.50	**A'**	251.90
A'	257.33	**E'**	253.01
A'	280.23	**A'**	264.56
E'	290.15	**E'**	278.19
E"	297.75	**A'**	286.38
A'	304.69	**E'**	299.76
A'	332.82	**A'**	300.82
E"	342.31	**E"**	307.71
E"	375.38	**E"**	330.18
E'	385.81	**E"**	346.14
A'	387.20	**E'**	355.85
E"	392.99	**E"**	374.49
E'	402.13	**A'**	382.94
E"	408.65	**E'**	398.48
A'	415.94	**E"**	399.41
E'	443.15	**A'**	413.90
A'	447.04	**E'**	417.82
E'	448.90	**E'**	444.99

E"	459.14	**E"**	449.35
E'	460.62	**E'**	449.66
A'	469.30	**A'**	452.93
E'	498.33	**E'**	465.43
A'	498.33	**A'**	477.47
A'	514.99	**A'**	496.13
E'	542.20	**A'**	517.33
E'	854.88	**E'**	531.25
A'	863.49	**E'**	830.70
E'	887.85	**A'**	839.17
A'	902.76	**E'**	868.22
E'	909.91	**A'**	885.84
E"	922.11	**E'**	898.02
E'	934.48	**E"**	900.52
E"	947.42	**A'**	919.05
A'	947.44	**E'**	934.50
A'	952.83	**A'**	937.68
E'	954.36	**E"**	938.44
A'	980.66	**A'**	962.26
E'	981.60	**E'**	968.78
A'	1018.73	**A'**	1001.26

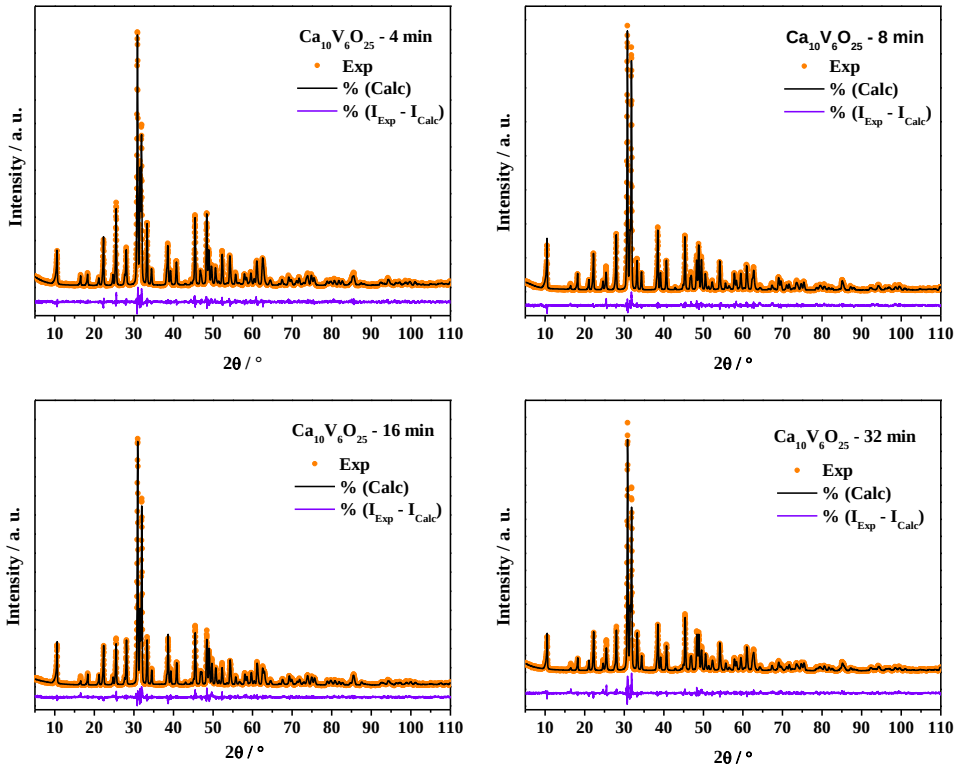

FIGURE B1 - Rietveld refinements based on data from the ICSD No. 24100 for the $Ca_{10}V_6O_{25}$ processed at 120 °C as function of synthesis time.

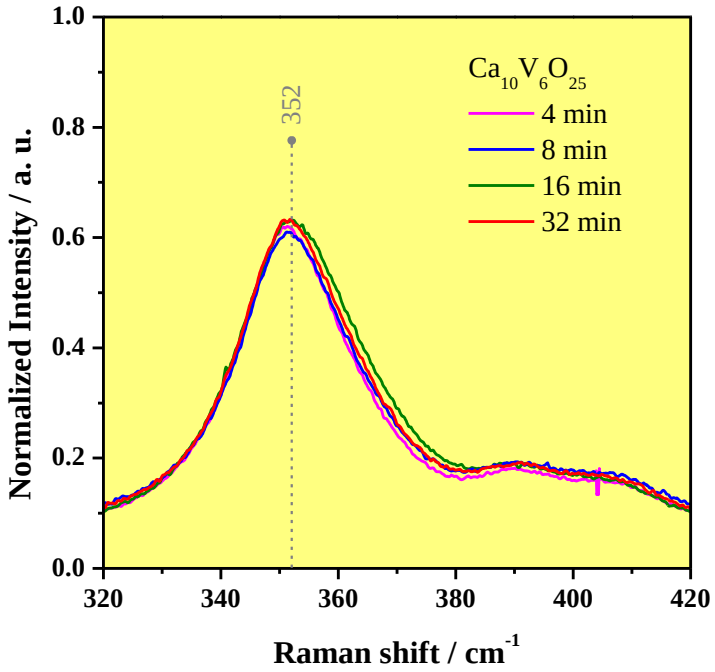

FIGURE B2 - Full width at half maximum at 352 cm^{-1} peak of $Ca_{10}V_6O_{25}$ crystals as function of synthesis time.

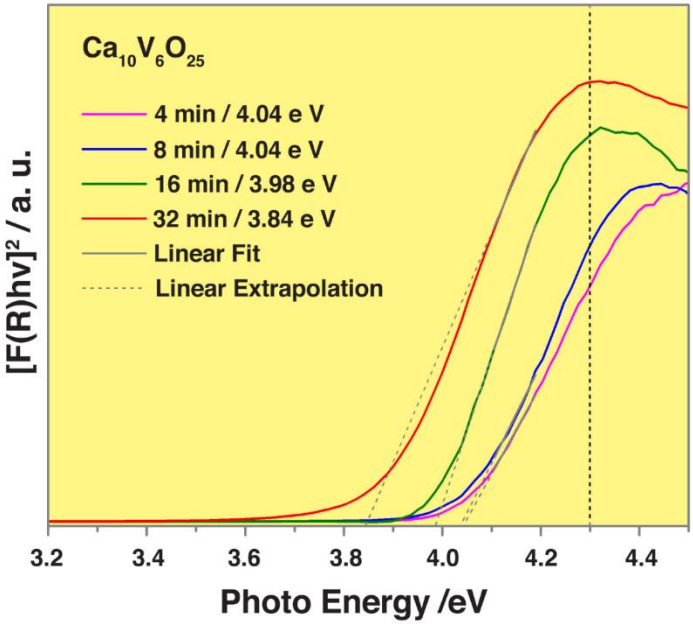

FIGURE B3 - UV-vis diffuse reflectance spectra with direct-type optical transition of the $Ca_{10}V_6O_{25}$ samples processed at 120 °C as function of synthesis time.

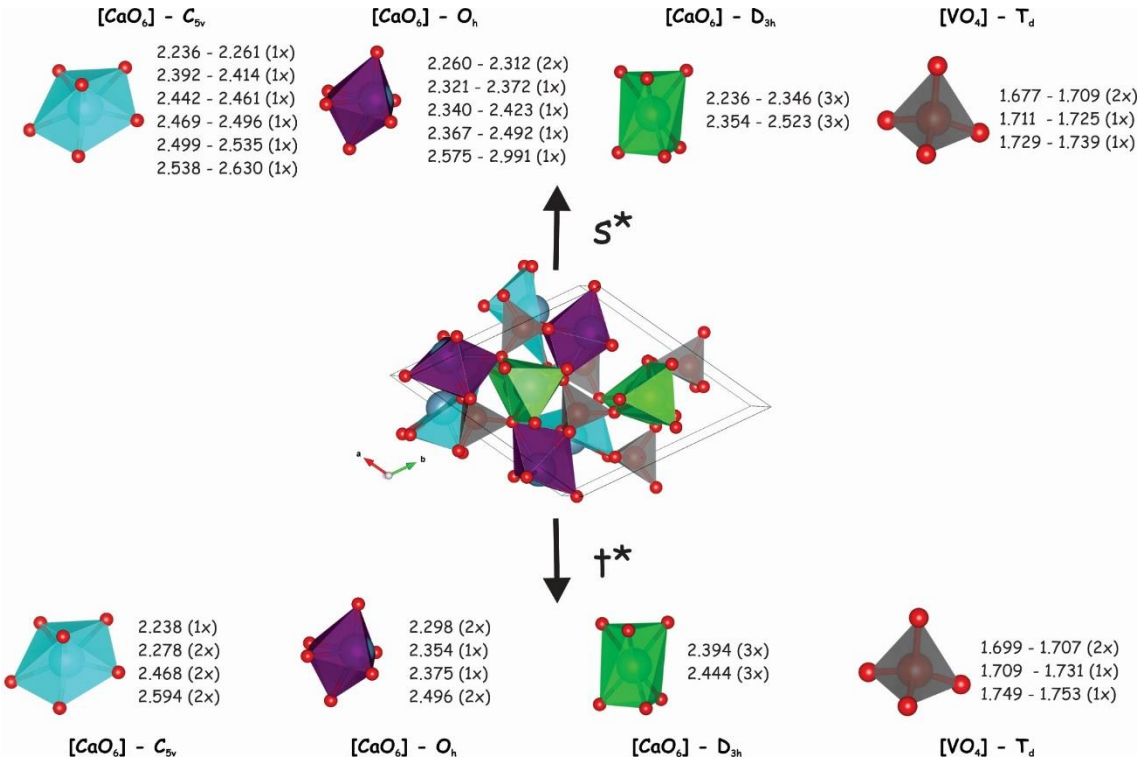

FIGURE B4 - Schematic representation of the constituent clusters for $Ca_{10}V_6O_{25}$ material and its calculated bond distances (in Å) for excited s* and t* states. The values 1x, 2x and 3x correspond to the bond multiplicity.

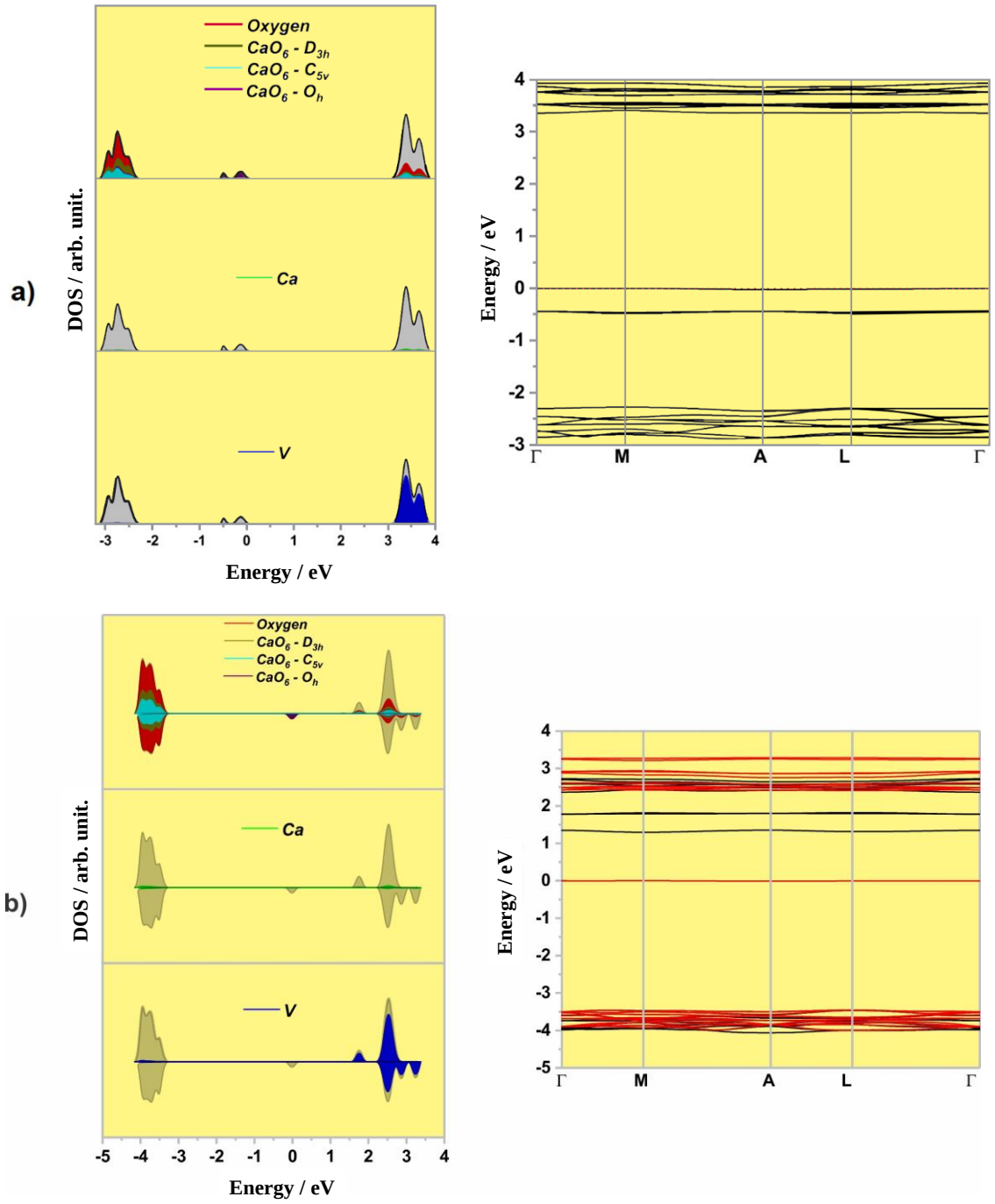

FIGURE B5 - Total and atom-resolved DOS and bands structure profiles for $Ca_{10}V_6O_{25}$ material at s* (a) and t* (b) electronic states. In both cases the Fermi level was set to zero.

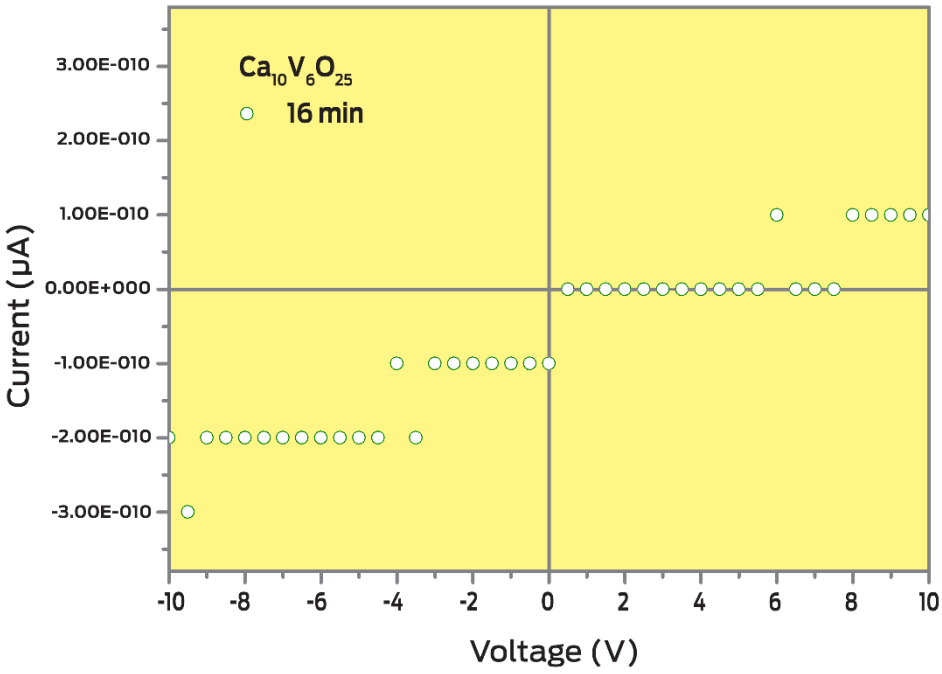

FIGURE B6 - Current-Voltage for the $Ca_{10}V_6O_{25}$ crystal at 16 min in 120 °C by MAH at room temperature.